Etude des ondes de gravité dans l'atmosphère au moyen de ballons et de simulations

Valerian Jewtoukoff

▶ **To cite this version:**

Valerian Jewtoukoff. Etude des ondes de gravité dans l'atmosphère au moyen de ballons et de simulations. Océan, Atmosphère. Université Paris 6, 2014. Français. <tel-01176779>

HAL Id: tel-01176779
https://tel.archives-ouvertes.fr/tel-01176779

Submitted on 15 Jul 2015

Étude des ondes de gravité dans l'atmosphère au moyen de ballons et de simulations

présenté par

Valérian Jewtoukoff

THÈSE DE DOCTORAT DE L'UNIVERSITÉ PARIS VI
Spécialité:
MÉTÉOROLOGIE, OCÉANOGRAPHIE ET ENVIRONNEMENT

Soutenance le 19 novembre 2014, devant le jury composé de:

Vladimir Zeitlin	LMD	Président
Jean-Pierre Chaboureau	LA	Rapporteur
Stuart Webster	MetOffice	Rapporteur
François Lott	LMD	Examinateur
Philippe Keckhut	LATMOS	Examinateur
Philippe Cocquerez	CNES	Examinateur
Riwal Plougonven	LMD	Directeur
Albert Hertzog	LMD	Co-Directeur

Largage d'un ballon pressurisé depuis la station McMurdo (Antarctique) durant la campagne Concordiasi en 2010.

Ho an'i Neny

ACKNOWLEDGEMENTS

TABLE OF CONTENTS

LIST OF FIGURES

Figure

LIST OF TABLES

LIST OF ABBREVIATIONS

AIRS Atmospheric InfraRed Sounder

AMSU-A Advanced Microwave Sounding Unit-A

AMPS Antarctic Mesoscale Prediction System

CCM Chemistry-Climate Model

CGW convective gravity wave

CMIP5 Coupled Model Intercomparison Project 5

CNES Centre National des Etudes Spatiales

DART Data Assimilation Research Testbed

ECMWF European Center for Medium-range Weather Forecast

EnKF ensemble Kalman filter

ESM Earth System Model

GCM Global Climate Model

GPS Global Positioning System

GW gravity wave

GWD gravity wave drag

HF high-frequency

HIRDLS HIgh Resolution Dynamics Limb Sounder

IASI Infrared Atmospheric Sounding Interferometer

IGW inertia-gravity wave

IMF integrated momentum flux

IPSL Institut Pierre Simon Laplace

LMD Laboratoire de Météorologie Dynamique

MLS Microwave Limb Sounder

NCAR National Center for Atmospheric Research

NCEP National Center for Environmental Prediction

NGW nonorographic gravity wave

NGWD nonorographic gravity wave drag

OGW orographic gravity wave

OGWD orographic gravity wave drag

OSB open stratospheric balloon

PDF probability density function

PV potential vorticity

QBO Quasi-Biennal Oscillation

RS radiosounding

SABER Sounding of the Atmosphere using Broadband Emission Radiometry

SPB superpressure balloon

SSW Sudden Stratospheric Warming

TSEN Thermodynamic SENsor

TTL Tropical tropopause layer

UKMO U.K Meteorological Office

WRF Weather Research and Forecasting

ABSTRACT

Étude des ondes de gravité dans l'atmosphère au moyen de ballons et de simulations

par

Valérian Jewtoukoff

L'objectif de cette thèse est d'obtenir une meilleure connaissance des ondes de gravité atmosphériques, de leurs sources et caractéristiques, et de leur propagation au moyen d'observations ballons et de simulations. Les ballons pressurisés (SPBs) utilisés dans cette thèse sont une des meilleures plateformes d'observations des ondes de gravité, et permettent d'obtenir l'ensemble de leurs caractéristiques. Les modèles à haute résolution donnent une description complète de l'écoulement, non seulement des ondes, mais aussi de leurs sources. Nous avons combiné mesures par SPBs et modélisation pour décrire les ondes de gravité et évaluer le réalisme des champs d'ondes de gravité dans des sorties de modèles. En s'appuyant sur les observations de PreConcordiasi (2010), les ondes de gravité convectives sont décrites aux Tropiques sur l'ensemble de la campagne, ainsi que sur un cas de cyclone tropical en développement. Dans un deuxième temps, les observations de la campagne Concordiasi (2010) nous permettent de quantifier le réalisme du champ d'onde de gravité résolu aux hautes latitudes (hémisphère sud) décrit dans les analyses de l'ECMWF. Un bon accord géographique et saisonnier est observé pour les flux de quantité de mouvement et l'intermittence. Cependant, il est montré que la magnitude des flux est sous-estimé dans les analyses de l'ECMWF. Enfin, une contribution aux campagnes opérationnelles ballons est apportée, en se focalisant sur les ballons stratosphériques ouverts qui sont le plus grand défi pour le CNES. Pour des cas d'étude lors de la campagne Strapolété (2009), nous montrons que l'incertitude sur la position de retombée des ballons peut être réduite dans une configuration simple en assimilant des observations par radiosondages.

ABSTRACT

Study of the gravity waves in the atmosphere with balloons and simulations

by

Valérian Jewtoukoff

The goal of this thesis is to obtain a better knowledge of the atmospheric gravity waves in the atmosphere, of their sources and characteristics, and their propagation using balloon observations and modeling. The superpressure balloons (SPBs) used in this thesis are one of the best platforms to observe gravity waves, and allow us to retrieve the ensemble of their characteristics. High-resolution models provide a complete description of the flow, not only of the waves, but also of their sources. We have combined SPB measurements and modeling in order to describe the gravity waves and evaluate the gravity wave field in model outputs. Using the observations from PreConcordiasi (2010), the convective gravity waves are described in the Tropics during the whole campaign, and also for a case of developing Tropical Cyclone. Second, observations from the Concordiasi campaign (2010) allow us to quantify the realism of the resolved gravity wave field in the ECMWF analyses at high latitudes (Southern Hemisphere). A good geographical and seasonal agreement is found for the momentum fluxes and the intermittency. However, it is shown that the magnitude is underestimated in the ECMWF. Finally, we bring a contribution to the operational balloon campaigns, with a focus on the open stratospheric balloons, which constitute the greatest challenge for the CNES. For cases during the Strapolété campaign, we show that the uncertainty on the final touchdown position of the balloons can be reduced using a simple setup that assimilates radiosoundings.

CHAPTER I

Introduction

L'observation et la prévision de l'état de l'atmosphère et du climat terrestre pour les décennies à venir dépendent essentiellement des modèles numériques (Earth System Models; ESM) qui couplent plusieurs éléments du système climatique. Pendant longtemps, il fut admis que les interactions entre la basse et la moyenne atmosphère se faisaient uniquement dans le sens troposphère-stratosphère. Au cours des dernières décennies, on a découvert que les forçages en moyenne atmosphère par des phénomènes de dissipation d'ondes vont contribuer à accélérer ou décélérer la circulation en stratosphère. Ainsi, inclure la stratosphère (qui s'étend depuis environ 15 km au-dessus de la surface jusqu'à 50 km) dans la composante atmosphérique de ces modèles est devenu crucial pour une représentation réaliste de la circulation atmosphérique. Le besoin d'améliorer la description de la circulation de la moyenne atmosphère constitue une motivation qui a conduit au développement de stratosphères dans les modèles de climat (*Gerber et al.*, 2012). La moyenne atmosphère dans les modèles s'étend généralement au-delà de la seule stratosphère et inclut une partie ou la totalité de la mésosphère (le sommet des modèles se situe entre 70 et 100 km). En outre, les modèles incluent desormais les interactions chimiques pour prédire notamment l'évolution de l'ozone (i.e. Chemistry-Climate Models; CCM). Avec l'amélioration et l'utilisation massive des CCM, les modèles qui participent au 5$^{\text{ème}}$ volet du Projet

de Comparaison des Modèles Couplés (Coupled Model Intercomparison Project 5; CMIP 5) ont une moyenne atmosphère. Au sein de CMIP5, les CCM ont été validés et comparés et des biais persistents se dégagent (*Eyring et al.*, 2010; *Butchart et al.*, 2010). Un de ces biais est lié à la difficulté des modèles à représenter la destruction du vortex polaire au printemps, en particulier pour l'hémisphère sud. Ce biais commun à la plupart des CCM simule une stratosphère d'hiver dans l'hémisphère sud trop froide avec un vortex polaire qui se détruit trop tard (jusqu'à plusieurs semaines). Cette difficulté provient des problèmes associés à la représentation des réchauffements stratosphériques soudains (Stratospheric Sudden Warmings; SSWs). En particulier, les SSW varient en fréquence et en synchronisation dans les différents modèles de climat. Le second biais provient de la difficulté de simuler l'Oscillation Quasi-Biennale (QBO; Quasi-Biennal Oscillation) en raison des problèmes liés à la représentation des ondes de gravité et des ondes équatoriales.

1.1 La circulation de l'atmosphère moyenne

La circulation zonale en moyenne atmosphère obtenue à partir de mesures satellites et illustrée en figure 1.1 est caractérisée par un jet d'est dans l'hémisphère d'été et un jet d'ouest dans l'hémisphère d'hiver, avec des maxima de vent à environ 60 km d'altitude. On observe une asymétrie sur la vitesse des vents zonaux, qui est due au fait que des ondes quasi-stationnaires se propagent verticallement et se dissipent dans la stratosphère sous l'effet des vents d'ouest, produisant un ralentissement de l'écoulement. Dans les parties qui suivent, nous décrivons les principales composantes de la dynamique de l'atmosphère moyenne.

1.1.1 L'Oscillation Quasi-Biennale (QBO)

L'Oscillation Quasi-Biennale (QBO; Quasi-Biennal Oscillation) est un élément essentiel du climat dans les tropiques (*Baldwin et al.*, 2001) et constitue la source de

variabilité principale en stratosphère tropicale. Le mécanisme fondamental qui force la QBO a été décrit à la fin des années 60 par *Lindzen and Holton* (1968) et *Holton and Lindzen* (1972), et constitue un modèle d'interaction onde-écoulement moyen en absence de rotation. La QBO est caractérisée par une alternance d'est en ouest des vents zonaux avec des périodes de 24-30 mois (voir figure 1.2) et symétrique par rapport à l'equateur. Les régimes de vent apparaissent au dessus de 30 km d'altitude avant de se propager vers le bas et s'atténuer en dessous de 20 km. L'amplitude maximale des vents est de l'ordre de 20 m s^{-1}.

1.1.2   Les Réchauffements Stratosphériques Soudains (SSW)

Les réchauffements stratosphériques soudains (SSW; Stratospheric Sudden Warming) correspondent à des périodes où le vortex polaire est détruit dans l'hémisphère d'hiver, et s'accompagnent d'un ralentissement significatif du jet en stratosphère (*Andrews et al.*, 1987) (voir figure 1.3). Les SSW se produisent sous l'effet de l'interaction entre l'écoulement moyen et les ondes planétaires comme illustré sur le schéma de la figure 1.4. Ces évènements sont associés à des augmentations brutales de température en stratosphère et constituent la source principale de la variabilité pour l'ozone polaire. Ils influencent aussi la circulation et les températures en troposphère (*Thompson and Wallace*, 1998; *Baldwin et al.*, 2001).

1.1.3   La circulation de Brewer-Dobson

La circulation de Brewer-Dobson (parfois aussi appelée circulation résiduelle (*Vallis*, 2006)) est une composante majeure du système climatique qui transporte notamment la vapeur d'eau qui pénètre la stratosphère au niveau de la Tropical Tropause Layer (TTL; *Fueglistaler et al.* (2009)) vers les pôles (voir B-D circulation sur le schéma de la figure 1.4). Cette circulation est engendrée en réponse à la dissipation d'ondes en basse stratosphère, les ondes de Rossby apportant la principale contribu-
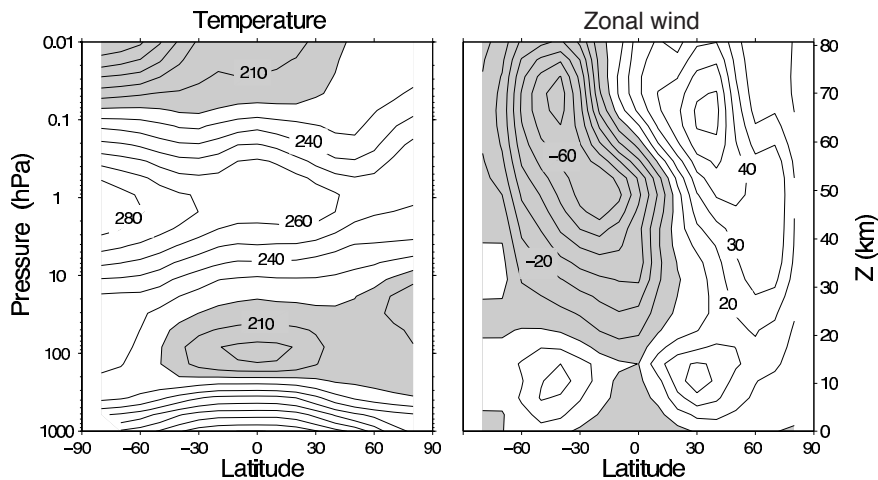
Figure 1.1: Moyennes zonales de la température en K (à gauche) et du vent zonal en
m s^{-1} (à droite) de la surface à 80 km d'altitude pour le mois de janvier.
Figure tirée de *Vallis* (2006).
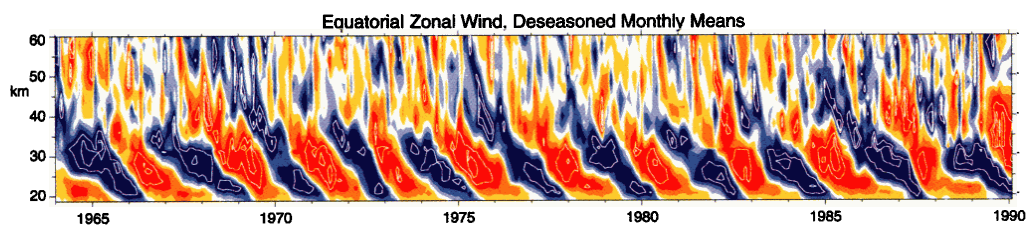
Figure 1.2: Signature de la QBO dans le vent moyen dans les tropiques pour la période
1964-1990 en fonction de l'altitude et du temps à partir d'observations
provenant de radiosondages et de roquettes. Le cycle saisonnier moyen a
été retranché. Figure tirée de *Baldwin et al.* (2001).

tion (voir figure 1.4)(*Vallis*, 2006).

1.1.4   La circulation en mésosphère

En mésosphère, la circulation résiduelle est dominée par un transport orienté du pôle d'été vers le pôle d'hiver (Fig. 1.4). La circulation est engendrée par le forçage zonal produit par le déferlement des ondes de gravité, et ferme le jet en mésosphère.

1.2   L'importance des ondes de gravité en moyenne atmosphère

Comme nous l'avons vu précédemment, les principales composantes de la circulation en moyenne atmosphère résultent d'interactions onde-écoulement moyen. Les ondes équatoriales ont un rôle déterminant en stratosphère pour la QBO, les ondes planétaires pour les SSW aux hautes latitudes, les ondes baroclines pour la circulation de Brewer-Dobson, et les ondes de gravité dans la fermeture du jet mésosphérique. Nous soulignons ici l'importance particulière des ondes de gravité.

Pour la QBO, les simulations de *Kawatani et al.* (2010) et *Evan et al.* (2012) soulignent l'importance des ondes de gravité à méso-échelle durant les phases d'est et des ondes de Kelvin durant les phases d'ouest. Leur importance relative est encore sujet à débat et une quantification des contributions relatives est par conséquent nécessaire. *Dunkerton* (1997) a montré à partir de simulations que les ondes de gravité contribuent à l'accélération de la circulation moyenne, mais que les flux de quantité de mouvement associés à ces seules ondes n'étaient pas suffisants pour forcer la QBO. Les ondes de gravité vont aussi influencer la circulation aux hautes latitudes après un SSW. De plus, *Angot et al.* (2012) ont identifié un signal d'onde de gravité en mésosphère avant un épisode de SSW, ce qui suggère qu'elles pourraient jouer un rôle potentiel dans l'initiation du phénomène. Les ondes de gravité jouent également
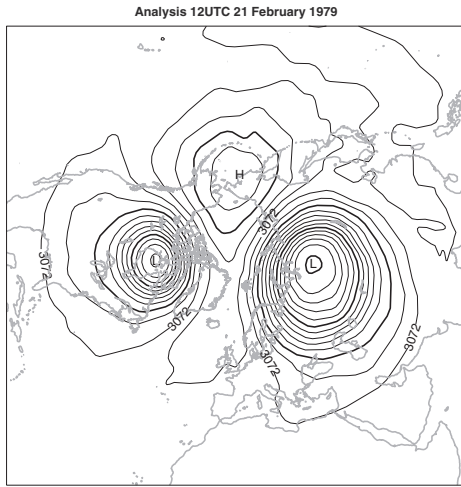
Figure 1.3: Altitude du géopotentiel 10 hPa le 21 février 1979 à 12UTC illustrant la destruction du vortex polaire associé à un SSW. Figure tiré de *Holton* (2004).
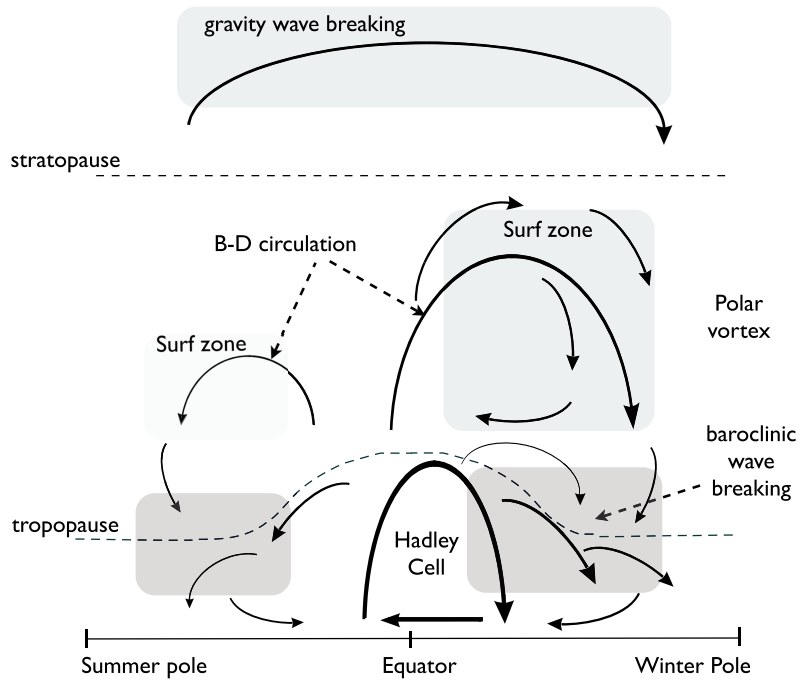
Figure 1.4: Circulation résiduelle moyenne dans l'atmosphère. Figure tiré de *Vallis* (2006).

un rôle dans la destruction de l'ozone dans les nuages stratosphériques polaires aux hautes latitudes ou encore le mélange des particules d'air lorsqu'elles se dissipent.

Il faut faire une distinction importante pour les ondes de gravité en fonction de leurs sources : les ondes orographiques excitées par la topographie pour lesquelles les sources sont fixes, connues, et plutôt bien comprises, et les ondes non-ographiques excitées par la convection, les fronts et les jets, et qui demeurent moins bien comprises. Les contributions relatives des deux types d'ondes ne sont pas encore complètement clarifiées, y compris dans les GCM. Par exemple, *McLandress et al.* (2012) attribuent le déficit de forçage à 60°S sur le vortex polaire de l'hémisphère à une mauvaise représentation des ondes orographiques générées par des petites îles isolées (*Alexander et al.*, 2009). Cependant, ils n'excluent pas non plus que le déficit puisse également provenir du manque important de sources d'ondes non-orographiques. En outre, l'étude récente de *McLandress et al.* (2013) montre que les rôles relatifs des ondes orographiques et non-orographiques en mésosphère ont des variabilités différentes. Par conséquent, il est nécessaire d'obtenir des climatologies pour les ondes non-orographiques, et de quantifier leurs contributions pour les flux de quantité de mouvement, ainsi que leurs caractéristiques spectrales afin de mieux contraindre les paramétrisations.

1.3 Les paramétrisations des ondes de gravité

Etant données les échelles courtes d'une partie importante des ondes de gravité (10-100 km) par rapport aux plus petites échelles correctement résolues par les GCM (500-1000 km), il est nécessaire de représenter leurs impacts sur la circulation atmosphérique par des paramétrisations. On peut décomposer les principaux ingrédients en deux catégories :

1. les éléments principaux :

   (a) la description des sources ;

(b) la propagation sur la verticale ;

(c) la description de la dissipation et du forçage correspondant.

2. les paramètres principaux :

(a) les caractéristiques des ondes au niveau des sources (vitesse de phase, longueur d'onde) ;

(b) l'amplitude des flux de quantité de mouvement.

Ce forçage des ondes de gravité sur l'écoulement est généralement appelé "trainée" (gravity wave drag; GWD) dans la littérature, bien qu'il puisse s'agir aussi d'une accélération (et pas seulement une décélération). On distingue les paramétrisations pour les ondes orographiques pour lesquelles les sources sont connues (orographic gravity wave drag; OGWD) de celles des ondes non-ogrographiques (nonorographic gravity wave drag; NGWD) dont les sources sont uniformément réparties et pour lesquelles on comprend moins le phénomène d'excitation. De plus, les phénomènes comme la dissipation sont encore des sujets de recherche et leur représentation dans les paramétrisations est soumise aux choix que font les modélisateurs. Ces problèmes motivent donc l'analyse des observations pour mieux contraindre ces paramétrisations. Des détails et des comparaisons entre différentes paramétrisations sont présentés dans *Kim et al.* (2003).

1.4   Les moyens d'observation des ondes de gravité

Les premiers calculs directs de flux de quantité de mouvement à partir d'observations pour des ondes de gravité ont été effectués par *Vincent and Reid* (1983) en mésosphère au moyen d'une technique qui utilise deux ou plus faisceaux radars haute fréquence (HF). Cette technique a par la suite été appliquée à d'autres radars au Japon, au Pérou, au Royaume-Uni et en Inde à partir du début des années 90, notamment par

Sato (1993) et *Fritts et al.* (1997). Plus récemment, l'estimation des flux de quantité de mouvement est basée sur de nouvelles techniques qui reposent toutes sur l'analyse de fluctuations dans les observations de vent ou température (induites par les ondes de gravité) par rapport à un état de base, et utilisent les relations de polarisations des ondes. Les observations permettent d'obtenir les climatologies des flux de quantité de mouvement, les caractéristiques spectrales des ondes, ainsi que d'étudier les sources. Ces moyens d'observation et les méthodes pour obtenir les flux de quantité de mouvement et les caractéristiques des ondes sont décrits et comparés dans *Fritts and Alexander* (2003), *Alexander et al.* (2010) et *Geller et al.* (2013).

1.4.1   Les ondes de gravité

Les ondes de gravité sont des perturbations de petite amplitude par rapport à un état de base uniforme horizontalement en vent $\bar{u}$, $\bar{v}$, en température $\bar{T}$ et densité $\bar{\rho}$. Elles sont observées dans l'atmosphère comme l'illustrent les photographies de la figure 1.5, mais aussi dans l'océan. La relation de dispersion qui lie les nombres d'onde (k, l, m) à la pulsation intrinsèque $\hat{\omega}$ (i.e. la fréquence mesurée dans le référentiel en mouvement qui se déplace avec l'écoulement) de l'onde a été dérivée à partir des équations de conservation pour les fluides par *Fritts and Alexander* (2003) et s'écrit de la manière suivante :

$$\hat{\omega}^2 = (\omega - k\hat{u} - l\hat{v})^2 = \frac{N^2(k^2 + l^2) + f^2[m^2 + (2H)^{-2}]}{k^2 + l^2 + m^2 + (2H)^{-2}}, \tag{1.1}$$

où ω est la fréquence absolue mesurée par rapport au sol, N est la fréquence de Brunt-Väisälä, f est le paramètre de Coriolis et H est une échelle verticale pour la densité. Les différents moyens d'observation ont des résolutions différentes, et les méthodes d'analyse pour estimer les flux de quantité de mouvements reposent sur des techniques différentes pour identifier les perturbations induites par les ondes de gravité. Par conséquent, cela va limiter la gamme de longueurs d'ondes qui vont

a)
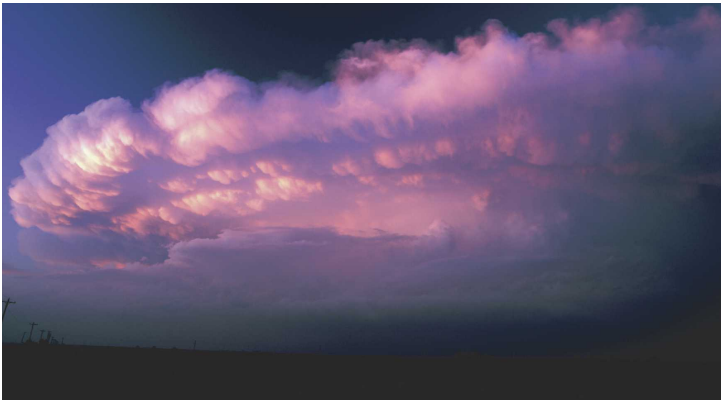
b)

Figure 1.5: Exemple d'ondes non-orographiques. a) Paquet de GWs préfrontal pho-
tographié par avion à 4 km d'altitude au-dessus de la mer à l'ouest de
l'Angleterre le 24 novembre 2009 à environ 1420UTC (tiré de *Knippertz
et al.* (2010)). b) Enclume de cumulonimbus organisée en ligne, en train
d'émettre des ondes de gravité (voir les oscillations de la couche nuageuse
au niveau de l'enclume) le 5 mai 2002 à l'est de Silverton, TX (copyright
©C. Doswell, tous droits réservés, reproduit avec permission).

pouvoir être résolues. De plus, en vertu de la relation (1.1), des restrictions sur la gamme de longueurs d'ondes produit de manière équivalente une restriction sur la gamme des fréquences comme l'a illustré *Alexander* (1998). Nous décrivons les différents types d'observation et les techniques pour calculer les flux de quantité de mouvement et les caractéristiques des ondes dans les sections qui suivent.

1.4.2 Les satellites

Les instruments embarqués sur les satellites permettent d'obtenir des profils verticaux de température quasi-globale sur de longues périodes de temps. L'état de base de l'atmosphère est retranché au champ total et le résidu est supposé représenter des fluctuations de température T' induites par des ondes de gravité. On distingue deux méthodes d'observation par satellite : les observations au nadir (par exemple AIRS et Advanced Microwave Sounding Unit-A AMSU-A) qui permettent d'identifier les ondes qui ont une grande longueur d'onde verticale (typiquement >12-15 km), et les observations au limbe (HIRDLS; HIgh Resolution Dynamics Limb Sounder ; ou encore SABER par exemple) qui permettent de résoudre les ondes de grandes longueurs d'onde horizontales. En dépit de l'avantage de la couverture globale, les limitations en terme de résolution (typiquement 100-500 km horizontalement) et les incertitudes pour estimer la direction de propagation des ondes conduit à des biais importants (au moins d'un facteur 2) sur les flux de quantité de mouvement (*Ern et al.*, 2004; *Preusse et al.*, 2009).

1.4.3 Les radiosondes

Les radiosondages permettent d'obtenir des mesures de vent horizontal et de température lors de leur ascension jusqu'à 25-30 km d'altitude. Des hypothèses sont nécessaires pour le calcul des flux de quantité de mouvement. Par exemple, on suppose que l'énergie des ondes se propage vers le haut, et en utilisant les relations de polar-

isation et la corrélation entre vitesse et température, on obtient une estimation des flux (*Vincent et al.*, 1997). Ces mesures permettent de couvrir de longues périodes de temps mais sont effectuées avec une fréquence limitée (1 ou 2 fois par jour en général), et ne sont valables que dans un rayon de quelques centaines de kilomètres au plus autour du site de lancement. Si le réseau est suffisamment dense, il est cependant possible de moyenner entre plusieurs stations pour obtenir des climatologies comme l'ont fait *Allen and Vincent* (1995) et *Gong et al.* (2008).

1.4.4 Les lidars et les radars

Les lidars Rayleigh permettent aussi d'obtenir des climatologies sur une suffisamment longue période avec une résolution verticale approximativement égale à 1 km à l'endroit du site à partir d'observations de température (*Wilson et al.*, 1991a,b; *Marsh et al.*, 1991; *Mitchell et al.*, 1991; *Whiteway and Carswell*, 1995).

Les radars mesurent les vents en utilisant l'effet Doppler dans la troposphère, la stratosphère et jusqu'en mésosphère (*Vincent and Reid*, 1983; *Tsuda et al.*, 1989; *Chagnon and Gray*, 2008). A l'instar des observations faites par radiosonde ou lidar, les mesures sont localisées spatiallement mais offrent une couverture temporelle relativement bonne qui permet d'analyser les variations saisonnières sur plusieurs années (*Vaughan and Worthington*, 2007).

1.4.5 Les avions

Les mesures des fluctuations de vent et de température par avion en basse stratosphère ont permis d'obtenir des informations sur les longueurs d'ondes horizontales des ondes de gravité (*Nastrom et al.*, 1987; *Bacmeister et al.*, 1996). Bien que ce soient des mesures in-situ, ces mesures sont trop courtes dans le temps pour pouvoir donner une information sur les variations saisonnières. En revanche, un ensemble de vols permet d'en faire l'étude. De plus, elles ont permis une meilleure compréhension

de la variabilité des ondes qui est un paramètre important pour contraindre les études théoriques et numériques. En particulier, certaines études ont relié les caractéristiques des ondes à leur sources troposphériques : topographie (*Gary*, 1989; *Bacmeister et al.*, 1990a,b), convection et fronts (*Fritts and Nastrom*, 1992; *Pfister et al.*, 1993b,a; *Alexander and Pfister*, 1995; *Alexander et al.*, 2000).

1.4.6   Les ballons pressurisés

Les ballons pressurisés sont constitués d'une enveloppe rigide qui maintient un volume quasi-constant et permet ainsi de voler sur des surfaces isopycnes (i.e. des surfaces de densité constante) pendant de longues périodes de plusieurs mois, couvrant ainsi des régions géographiques étendues. Les observations sont effectuées avec une fréquence d'échantillonage relativement élevée par rapport aux autres moyens d'observations (15 min lors de la campagne Vorcore, 30 s à partir des campagnes Pre-Concordiasi et Concordiasi) lors de leur vol permet d'observer une plus grande partie, voire l'intégralité, du spectre des ondes de gravité. Une caractéristique unique des ballons pressurisés est qu'ils sont advectés par l'écoulement moyen, et par conséquent se comportent comme des traceurs quasi-lagrangiens, ce qui permet de mesurer directement les fréquences intrinsèques des phénomènes observés. Des estimations des flux de quantité de mouvement pour les ondes de gravité ont été obtenues en basse stratosphère par *Hertzog and Vial* (2001) localement pour un petit nombre de ballons, puis à l'échelle de la calotte polaire par *Vincent et al.* (2007) et *Hertzog et al.* (2008). En raison des avantages qu'apportent les ballons pressurisés, *Geller et al.* (2013) concluent dans leur revue sur les moyens d'observations des ondes de gravité que '*The fluxes derived from the Vorcore balloons are considered the most accurate global-scale measurements available, for waves with intrinsic frequencies $\hat{\omega}$ lower than $2\pi(1\ h)^{-1}$*'. De plus *Alexander et al.* (2010) ajoutent qu'une bonne stratégie pour l'étude des ondes de gravité est de combiner plusieurs moyens (simulations et obser-

vations), ce qui justifie ainsi l'approche que nous adoptons par la suite dans notre
étude.

1.5   Les campagnes ballons pressurisés (SPB)

1.5.1   PreConcordiasi

Durant la phase de préparation pour la campagne Concordiasi (*Rabier et al.*,
2010), le CNES a lancé 3 ballons pressurisés depuis les îles Seychelles (55.5°E,4.6°N)
en février 2010. Ces vols étaient destinés à tester les ballons et les instruments em-
barqués en vue de Concordiasi. Le capteur Thermodynamic SENsor (TSEN) qui était
utilisé pour effectuer des mesures de pression et de température était installé en bas
de la chaîne de vol pour éviter toutes perturbations dues au ballon. Les vitesses hori-
zontales ont été calculées en utilisant les positions successives des ballons lors de leur
vol mesurées par GPS. Toutes les mesures sont effectuées avec une grande résolution
temporelle (30 s). Ces ballons ont volé en basse stratosphère tropicale entre 60 et
70 hPa (19-20 km d'altitude) pendant des périodes typiques de 3 mois, durant une
phase de retournement de la QBO.

1.5.2   Concordiasi

La campagne Concordiasi (*Rabier et al.*, 2010) au printemps austral 2010 avait
pour but l'étude de la circulation et de l'ozone en basse stratosphère aux hautes
latitudes et létalonnage et la validation des observations satellites IASI (Infrared At-
mospheric Sounding Interferometer). Pour la composante ballon de cette campagne,
18 SPBs ont été lancés depuis la station de McMurdo (78°S,166°E) en Antarctique
entre aôut et septembre 2010 par le CNES. Les ballons sont identiques à ceux de la
campagne PreConcordiasi et ont embarqué la même technologie. Les ballons ont volé
pendant environ 4 mois chacun. Le but de la campagne était l'étude de circulation

et de l'ozone en basse stratosphère aux hautes latitudes.

1.5.3 Les enjeux pour les campagnes opérationnelles ballons

Les activités ballons génèrent des contraintes de sécurité lors des phases de descente et d'atterissage des chaînes de vols qui peuvent peser jusqu'à une tonne. Les ballons ne doivent pas atterrir dans des zones densément peuplées ou avec des infrastructures pour ne pas causer de dégats humains ou matériels. Pour le CNES, les problématiques de sécurité sont les plus grandes pour les ballons stratosphériques ouverts (Open Stratospheric Balloons; OSB) dont les charges utiles sont les plus importantes et pour lesquels les prévisions opérationnelles sur le point de descente varient avec une incertitude de plusieurs dizaines de kilomètres. Nos études sur les ondes de gravité dépendent en grande partie de mesures faites par SPB comme nous l'avons vue dans les parties précédentes. Par conséquent, les questions de sécurité nous concernent également pour les vols longue durée, et il est donc crucial d'améliorer les prévisions des trajectoires pour les ballons en général, au moyen de simulation numériques à méso-échelle, et d'observations supplémentaires. La prévision des trajectoires de SPB nous intéressent également pour l'avenir au sein de l'équipe et dans le cadre de la collaboration avec le CNES, mais l'étude s'est naturellement orientée sur les OSB qui posent un problème plus urgent pour le CNES.

1.6 Les objectifs de la thèse

L'objectif de la thèse est 1) d'étudier les ondes de gravité non-orographiques dans l'atmosphère pour contraindre les paramétrisations, et 2) donner des pistes d'amélioration pour les campagnes opérationelles. Nous avons utilisé les données provenant de ballons, et les simulations méso-échelle avec le modèle WRF déjà utilisées au LMD, ainsi que les produits globaux provenant de l'ECMWF. La thèse porte sur les ballons et les ondes de gravité. Nous présentons les 2 premières parties de l'étude

qui portent directement sur cette question, puis une 3ème partie qui donne des pistes pour l'amélioration des campagnes ballons :

1. Les ondes de gravité convectives, excitées aux tropiques par la convection profonde (complexes convectifs de méso-échelle, cellules isolées, cyclones tropicaux) sont étudiées dans le chapitre II à partir des données PreConcordiasi et de simulations à méso-échelle. Nous comparons les flux de quantité de mouvement, les caractéristiques spectrales des ondes, et leur intermittence dans les simulations et les observations sur un cas d'étude de cyclone tropical. Dans une seconde partie, nous élargissons l'étude à l'ensemble des données PreConcordiasi en quantifiant les vitesses de phase, l'intermittence, et la contribution des cyclones tropicaux au forçage global en moyenne atmosphère, et nous comparons les contributions relatives des évènements intenses non-orographiques et orographiques.

2. Nous étudions les ondes de gravité non-orographiques, excitées aux hautes latitudes (dans l'Hémisphère sud) par les systèmes frontaux et les jets dans le chapitre III en utilisant les données Concordiasi que nous comparons aux analyses de l'ECMWF. Avec l'augmentation de la résolution et de la fiabilité des analyses ECMWF, il devient maintenant crucial d'estimer le degré de réalisme de leur champ d'ondes de gravité. Nous étudions la variabilité saisonnière et géographique des flux de quantité de mouvement et de l'intermittence sur l'ensemble de la durée de la campagne Concordiasi.

3. Dans le chapitre IV, nous décrivons une stratégie pour apporter des améliorations pour les prévisions des trajectoires ballons dans les opérations, en utilisant une approche qui utilise des simulations d'ensemble à méso-échelle et un filtre de Kalman d'ensemble qui permet d'assimiler des données type radiosondages. Nous présentons des tests sur 3 cas d'étude sur des OSB de la campagne

Strapolété 2009 à Kiruna, en Suède.

CHAPTER II

Les ondes de gravité convectives dans les tropiques

Les ondes de gravité excitées par la convection profonde tropicale en basse stratosphère sont étudiées dans ce chapitre, au moyen de données in-situ provenant de ballons pressurisés de la campagne PreConcordiasi, et de simulations numériques à méso-échelle avec le modèle WRF.

Les ondes de gravité sont un élément essentiel de la circulation de la moyenne atmosphère. Les ondes se propagent verticalement depuis leurs sources troposphériques jusqu'en stratosphère et en mésosphère où elles vont déferler quand elles atteignent des niveaux critiques ou sous l'effet de la diminution de la densité, et elles cèdent alors leur flux de quantité de mouvement à l'écoulement moyen. Les ondes de gravité participent à la dynamique de l'atmosphère moyenne et en particulier en stratosphère avec le forçage de la circulation de Brewer-Dobson aux moyennes latitudes (*Holton et al.*, 1995), et celui de l'Oscillation Quasi-Biennale dans les régions tropicales (QBO; *Dunkerton* (1997); *Kawatani et al.* (2010); *Evan et al.* (2012)), ainsi qu'en mésosphère pour leur rôle dans le forçage zonal. Les ondes de gravité sont des phénomènes d'échelles relativement petites en raison des gammes de fréquence et des vitesses de phases qu'imposent les sources et le milieu de propagation (de l'ordre de 10-1000 km horizontalement)(*Bacmeister et al.*, 1990b), et ne sont donc pas résolues explicitement dans les modèles de circulation globale (GCM) qui ont une résolution typique

de 100 km. Il est par conséquent nécessaire de représenter les ondes de gravité par des paramétrisations pour tenir compte de leur effets sur la circulation globale dans les GCM (*Kim et al.*, 2003). Les paramétrisations et leurs limitations constituent encore un obstacle dans la représentation de la circulation en stratosphère dans les modèles avec haut sommet (*Pawson et al.*, 2000; *Austin et al.*, 2003; *Butchart et al.*, 2010). En effet, certains modèles ne possèdent pas encore de QBO ou nécessitent de "nudger" des observations pour forcer la circulation en moyenne atmosphère à se mettre en place (*Douville*, 2009; *Hansen et al.*, 2013). Ces limitations constituent une motivation pour une meilleure connaissance et une meilleure compréhension des ondes de gravité dans l'atmosphère. La compréhension des ondes de gravité convectives a beaucoup évolué dans un premier temps au moyen d'études théoriques (*Lin and Smith*, 1986; *Nicholls et al.*, 1991; *Pandya et al.*, 1993), avec l'analyse d'observations (*Pfister et al.*, 1993b), puis avec l'arrivée de modèles de méso-échelle qui permettent de faire des simulations à haute résolution et de représenter explicitement les sources convectives, les ondes de petite échelle, ainsi que la dissipation des ondes en moyenne atmosphère (*Fovell et al.*, 1992; *Alexander et al.*, 1995; *Lane et al.*, 2001). Peu d'études à notre connaissance ont utilisé des observations in-situ à haute résolution et des simulations à méso-échelle pour les ondes convectives (*Alexander et al.*, 2010), et c'est donc l'objet de notre étude.

2.1 Sources et caractéristiques des ondes de gravité convectives

La convection profonde est reconnue comme une des sources principales d'onde de gravité non-orographique dans les tropiques (*Alexander et al.*, 1995; *Pandya and Durran*, 1996; *Chu and Lin*, 2000; *Lane et al.*, 2001). Leur signature est facilement identifiable à partir d'observations satellites à proximité de convection profonde, et on peut

désormais estimer leurs flux de quantité de mouvement (*Ern et al.*, 2011). Bien que la convection soit connue comme une source d'onde de gravité, et qu'elle ait fait l'objet d'études théoriques, ce n'est que récemment qu'on a pu déterminer leurs différents mécanismes d'excitation à partir d'observations et de simulations numériques. Les trois principaux mécanismes proposés sont les suivants :

- Le forçage par chauffage convectif : ce mécanisme d'excitation a été proposé par *Alexander et al.* (1995) et sa pertinence a été démontrée à partir d'observations satellites par *McLandress et al.* (2000). La chaleur latente dégagée par condensation produit un forçage de même échelle que le courant ascendant sur le champs de pression et les ondes excitées par ce mécanisme se propagent au-dessus des cellules convectives. En l'absence de fort cisaillement vertical, la longueur d'onde verticale est de l'ordre de la hauteur du chauffage convectif troposphérique (*Alexander et al.*, 1995; *Piani et al.*, 2000). *Salby and Garcia* (1987) ont montré que le chauffage convectif produit une onde de longueur d'onde verticale du même ordre que la hauteur du chauffage convectif en se propageant à travers la stratosphère. Le forçage thermique produit un champ d'ondes isotrope qui est filtré par l'écoulement moyen.

- L'effet d'obstacle (*Clark et al.*, 1986; *Pfister et al.*, 1993b,a) : par analogie avec les ondes orographiques, on considère que les nuages se comportent comme une montagne en mouvement qui vont faire obstacle à l'écoulement et génerer des ondes de gravité en modifiant la forme des surfaces isentropes. *Clark et al.* (1986) ont montré que ce mécanisme génère des ondes avec des amplitudes plus importantes que pour le forçage par chauffage convectif. Des signatures de l'effet d'obstacle ont été observées dans des radiosondages par *Vincent and Alexander* (2000); *Alexander and Vincent* (2000). Ce mécanisme génère des ondes qui se propagent préférentiellement contre le cisaillement.

- L'effet d'oscillateur mécanique (*Fovell et al.*, 1992) : les puissants courants ascendants (updrafts) dans les orages convectifs peuvent traverser la tropopause (on parle

alors d'"overshoot"), et les surfaces isentropes en stratosphère vont aussi se mettre à osciller. *Fovell et al.* (1992) ont montré que cette source locale de quantité de mouvement excite des ondes à la fréquence d'oscillation des "updrafts". Les anisotropies du champ d'onde pour ce mécanisme proviennent du filtrage par l'écoulement moyen, comme pour l'effet d'obstacle. *Lane et al.* (2001) ont montré que l'effet d'oscillateur domine l'effet de forçage thermique dans la phase mature des complexes convectifs.

La problématique de l'excitation n'est cependant pas encore complètement résolue et elle fait encore l'objet actuellement de recherches (*Song et al.*, 2003; *Alexander et al.*, 2006). L'importance relative des trois effets reste incertaine. De plus, la manière complexe dont le forçage thermique interagit avec le cisaillement et les couches stables en altitude est mal comprise (*Fritts and Alexander*, 2003). Bien que les débats au sujet des mécanismes d'excitations des ondes de gravité soient encore très actifs, nous ne traitons pas de ces questions dans notre étude.

Les ondes de gravité convectives ont été étudiées au moyen d'instruments embarqués (*Pfister et al.*, 1993b; *Wang et al.*, 2006), de mesures radar (*Sato*, 1993; *Chagnon and Gray*, 2008) et satellites (*Dewan et al.*, 1998). Parmi les sources convectives, les cyclones tropicaux ont été beaucoup étudiés parce que ces évènements ressortent singulièrement dans la circulation de la troposphère. Les caractéristiques principales des ondes convectives générées par les cyclones tropicaux ont été dérivées par des observations (*Sato*, 1993; *Dhaka et al.*, 2003) et à partir de simulations numériques (*Kim et al.*, 2005, 2007; *Kuester et al.*, 2008; *Kim and Chun*, 2010) :

- Importance des ondes avec longueurs d'onde de l'ordre de la centaine et de la dizaine de kilomètres horizontallement et verticalement (*Kim et al.*, 2005; *Kuester et al.*, 2008; *Kim and Chun*, 2010).

- Importance des petites fréquences intrinsèques, et des périodes plus courtes que 2h (*Kim and Chun*, 2010).

- L'émission d'ondes de gravité est plus importante durant la phase de développement

du cyclone tropical que pendant sa phase mature, et elle se fait à plus courte longueur d'onde.

- Les ondes se propagent principalement vers l'est relativement au vent avec des valeurs de vitesses de phase comprises entre 20 et 30 m s^{-1}.

- Les flux de quantité de mouvement sont de l'ordre de 10-50 mPa (*Sato*, 1993; *Kuester et al.*, 2008; *Kim and Chun*, 2010).

Les études qui utilisent des simulations numériques ont cependant montré que les estimations des flux de quantité de mouvement et des longueurs d'ondes restent sensibles à la résolution horizontale (*Lane and Knievel*, 2005), et qu'il est souhaitable d'utiliser la meilleure résolution possible (1 km ou moins).

2.2   Données disponibles et outils d'analyse

Les ballons pressurisés se prêtent bien à l'étude des ondes de gravité car ils peuvent obtenir une partie des caractéristiques des ondes de gravité. Ils ont été utilisés pour décrire les ondes de gravité dans les régions tropicales (*Hertzog and Vial*, 2001) ainsi qu'aux hautes latitudes (*Vincent et al.*, 2007; *Hertzog et al.*, 2008; *Plougonven et al.*, 2008, 2013). Dans notre étude, nous obtenons une description détailleé des ondes grâce aux caractéristiques suivantes des ballons :

- Les ballons sont advectés par l'écoulement atmosphérique de grande échelle, et ils ont donc un comportement quasi-lagrangien, ce qui leur permet de mesurer directement les fréquences intrinsèques des phénomènes observés.

- Ils disposent maintenant de mesures de pression et d'altitude précises (précision de 0.1 Pa et 1.5 m respectivement) qui permettent d'obtenir les flux de quantité de mouvement avec une plus grande précision que dans les études précédentes (*Hertzog et al.*, 2008; *Plougonven et al.*, 2008, 2013).

- La fréquence d'echantillonage par les instruments de mesure permet maintenant d'analyser tout le spectre des ondes de gravité, en particulier les ondes de haute

fréquence, qui étaient mal résolues dans les observations ballons jusque récemment.

L'utilisation de simulations numériques à méso-échelle permet en plus de donner une description de l'écoulement en trois dimensions et de pouvoir relier les ondes à leurs sources. La comparaison des données aux simulations apporte en outre une validation au modèle pour la représentation des sources en troposphère et des ondes de gravités convectives en basse stratosphère tropicale.

2.3   Principaux résultats

Nous récapitulons ici les principaux résultats obtenus à partir des simulations numériques à méso-échelle et des observations ballons. Pour le cas d'étude du cyclone tropical Gelane :

- Importance des ondes avec des vitesses de phases (relatives) entre -5 m s^{-1} et 50 m s^{-1} et avec des longueurs d'ondes entre 0 et 20 km, avec la contribution principale aux flux de quantité de mouvement provenant des ondes avec faible vitesse de phase (< 40 m s^{-1}) et avec courte longueur d'onde (< 20 km).

- Importance des ondes à hautes fréquences avec les ondes de périodes inférieures à 20 min qui contribuent pour 80% du flux total.

- Flux moyens de l'ordre de 100 mPa sur des échelles spatiales de 350 km.

A l'échelle de la campagne PreConcordiasi:

- Contribution principale aux flux de quantité de mouvement par les ondes quasi-stationnaires (vitesses de phase < 10 m s^{-1}).

- Frequence d'occurrence plus grande des évènements intenses purement convectifs (60%) par rapport aux évènements orographiques mixtes intenses aux tropiques, mais amplitude des flux comparables de l'ordre de 40 mPa en moyenne. Les cyclones tropicaux s'inscrivent dans la moyenne des évènements convectifs en terme d'amplitude des flux de quantité de mouvement. Ils représentent donc un contribution faible au forçage de la moyenne atmosphère bien qu'ils sont des sources locales d'ondes signi-

ficatifs.

- Intermittence des flux de quantité de mouvement relativement forte avec des valeurs du coefficient de Gini comprises entre 0.5 et 0.6. L'intermittence pour les hautes valeurs du flux provient majoritairement des ondes de gravité convectives.

2.4 "Gravity waves generated by deep tropical convection: Estimates from balloon observations and mesoscale simulations"

Gravity waves generated by deep tropical convection: Estimates from balloon observations and mesoscale simulations

Valérian Jewtoukoff,[1] Riwal Plougonven,[2] and Albert Hertzog[2]

[1] Convective gravity waves in the Tropics are studied by analyzing in situ measurements from long-duration stratospheric balloons launched during the PreConcordiasi campaign (2010) and mesoscale simulations. An improved temporal resolution of the observations as well as the balloon quasi-Lagrangian behavior allow an unprecedented investigation of the whole gravity wave spectrum. First, a case study of gravity waves generated by a developing cyclone, Tropical Storm Gelane (February 2010), is carried out using observations complemented by numerical simulations with the Weather Research and Forecast model, with a resolution down to 1 km. Distributions of momentum fluxes obtained from both data show reasonable agreement and emphasize waves with short wavelengths (< 15 km) and short periods (< 20 min). Still, some differences are also found, which can likely be related to errors of the modeled background flow. Second, observations from the whole PreConcordiasi flights are analyzed with an emphasis on gravity wave momentum fluxes. Their phase speed distribution has a robust shape, with maximum fluxes with near-zero ground-based phase speeds. Yet, significant momentum fluxes are also found for larger values, yielding a mean phase speed of about 27 m s^{-1}. The momentum fluxes are concentrated in short episodes with intense values, and their intermittency is quantified using probability distribution functions and the Gini coefficient (0.5–0.6). The relative importance of convective and topographic sources are investigated, suggesting comparable intensities, but a greater occurrence frequency of convective events. Waves emitted by Tropical Storm Gelane do not stand out relative to other convective events.

1. Introduction

[2] Gravity waves (GW) are key processes in the global middle atmosphere circulation. Their momentum, which is transported upward from tropospheric sources, is deposited in the stratosphere and mesosphere and essentially contributes to the force balance at those altitudes [*Fritts and Alexander*, 2003]. In the midlatitudes, GWs are consequently involved in the maintenance of the Brewer-Dobson circulation [*Holton et al.*, 1995], and they play a major role as well in driving the Quasi-Biennial Oscillation in the tropics [*Dunkerton*, 1997; *Kawatani et al.*, 2010; *Evan et al.*, 2012]. Since they occur on relatively small scales ($\sim$10–1000 km in the horizontal; some kilometers at most in

the vertical), dedicated parameterizations are needed to simulate their effects in atmospheric Global Circulation Models (GCMs) [*Kim et al.*, 2003]. Deficiencies in these parameterizations, and in particular in those used for nonorographic GWs, have been and remain a significant contributor to the biases of the so-called high-top GCMs, i.e., those including a well-resolved stratosphere [*Pawson et al.*, 2000; *Austin et al.*, 2003; *Butchart et al.*, 2010]. These deficiencies constitute a great motivation for improving our knowledge and understanding of atmospheric gravity waves, both through observations and numerical modeling [*Alexander et al.*, 2010].

[3] Deep convection is known to be one of the main sources of nonorographic GWs in the tropics, as evidenced in global maps of momentum fluxes obtained from satellite observations [e.g., *Ern et al.*, 2011]. Convectively generated gravity waves (CGW) have been the focus of observational studies using airborne measurements [e.g., *Pfister et al.*, 1993; *Wang et al.*, 2006], radar measurements [e.g., *Sato*, 1993], and satellite observations [e.g., *Dewan et al.*, 1998]. These studies have highlighted the importance of waves with horizontal scales of tens to hundreds of kilometers and vertical scales of about 10 km, corresponding to short intrinsic periods (i.e., a few tens of minutes).

[1]Laboratoire de Météorologie Dynamique du CNRS, Ecole Normale Supérieure, Paris, France.
[2]Laboratoire de Météorologie Dynamique du CNRS, Ecole Polytechnique, Palaiseau, France.

Corresponding author: V. Jewtoukoff, Laboratoire de Météorologie Dynamique du CNRS, Ecole Normale Supérieure, 24 rue Lhomond, 75005 Paris, France. (vjewtou@lmd.ens.fr)

[4] Among convective sources, Tropical Cyclones stand out as intense, organized events and have been specifically studied for their generation of GWs, both with observations [e.g., *Sato*, 1993; *Dhaka et al.*, 2003] and with numerical simulations [*Kim et al.*, 2005, 2007; *Kuester et al.*, 2008; *Kim and Chun*, 2010]. As finer resolution has become available, numerical simulations have stressed the role of waves with shorter and shorter wavelengths: *Kim et al.* [2005] simulated waves emitted by typhoon Rusa (2002) with a horizontal resolution of Δx = 27 km and found dominant wavelengths of 300–600 km, with periods of 6–11 h. *Kuester et al.* [2008] simulated Hurricane Humberto (2001) with a resolution down to Δx = 3 km and found dominant wavelengths of 15–300 km, with periods 20–100 min. Similarly, *Kim and Chun* [2010] simulated waves emitted by Typhoon Saomai (2006) and found dominant wavelengths of 10–100 km, with periods less than 2 h. These different studies have consistently contrasted the emission during different cyclone stages, showing stronger emission and shorter wave scales during the development stage as compared to later stages [*Kuester et al.*, 2008; *Kim and Chun*, 2010]. Phase speeds have been found to be mostly eastward, with typical values around 20 to 30 m s^{-1}. Local maxima of momentum fluxes have been estimated from observations as $\sim$ 40 mPa [*Sato*, 1993] and similar values from simulations (10–30 mPa in *Kuester et al.* [2008], 30–50 mPa in *Kim and Chun* [2010]). *Kim and Chun* [2010] improved on previous simulations by the extent of the fine-resolution domain. They displayed significant sensitivity of the model results to the resolution. In fact, at resolutions that are presently available for three-dimensional simulations, it is expected that CGWs will remain sensitive to resolution [*Lane and Knievel*, 2005]. In this respect, it is all the more important to have an observational counterpart to the numerical simulations. However, the short horizontal scales and high temporal frequencies of gravity waves generated by convection, as well as their location in the vicinity of cyclones, constitute major difficulties for many observing techniques. Recent long-duration balloon observations performed with a sampling frequency sufficient to resolve the whole GW spectrum provide a unique opportunity for such a comparison.

[5] Balloon-borne observations have already been used to estimate gravity wave momentum fluxes, either in the tropics [*Hertzog and Vial*, 2001] or at high latitudes [*Vincent et al.*, 2007; *Hertzog et al.*, 2008], and have also been successfully compared to high-resolution numerical simulations [*Plougonven et al.*, 2008, 2013]. They also served to describe gravity wave intermittency [*Alexander et al.*, 2010; *Hertzog et al.*, 2012], which is arguably a characteristic feature of convection. One outstanding characteristic of long-duration balloons is that they move with the wind, so that the intrinsic frequency ($\hat{\omega}$) of gravity wave packets are directly inferred from the observations. In these previous studies, however, the sampling rate during the flights, 1 obs/15 min, was too slow to resolve most of the waves generated by convection. Recently, the baud rate of the space link used to transfer data to the ground was increased so that it became possible to perform observations every 30 s during the flights, increasing the sampling rate by a factor 30. Consequently, the whole gravity wave spectrum ($|f| \leq \hat{\omega} \leq N$, with f and N the inertial and Brunt-Väisälä frequencies, respectively) is resolved in these observations. Three recent

long-duration superpressure balloons (SPB) launched from Seychelles Islands in 2010 in the framework of the PreConcordiasi campaign will be used here and provide the basis for the comparisons with numerical simulations of CGWs.

[6] The present study is divided into two distinct parts: In the first part, we focus on a case study where balloon observations have been collected over a developing cyclone in the Indian Ocean. Numerical simulations are specifically designed to reproduce this case, so as to let us compare the characteristics of simulated CGWs with those derived from the balloon observations. In the second part, we analyze GW signatures during the whole three balloon flights and aim at assessing the representativity and contribution of GW generated by Tropical Storms and Tropical Cyclones in the whole tropical belt.

[7] The paper is organized as follows: The balloon campaign, observations, and analysis method are first presented in section 2. The case study of the developing cyclone is described in section 3, as well as the associated numerical simulations. The characteristics of the observed and simulated gravity waves corresponding to this event are quantified and compared in section 4, while section 5 presents the observed overall wave characteristics for the whole three balloon flights. A summary and conclusion are presented in the last section.

2. Balloon Observations

2.1. The PreConcordiasi Campaign

[8] During the preparation of the Concordiasi campaign [*Rabier et al.*, 2010], the French Space Agency (Centre National d'Etudes Spatiales (CNES)) released three SPBs from Mahe Airport (55.530°E, 4.679°S), Seychelles Islands in February 2010. SPBs are closed balloons filled with helium, which drift on constant-density surface in the atmosphere [*Hertzog et al.*, 2007]. The PreConcordiasi flights were aimed at testing the balloons and payloads designed for Concordiasi. In particular, they hosted the Thermodynamic SENsor (TSEN) meteorological package that performs in situ observations of pressure and temperature along the flights. The wind is deduced from the successive balloon positions provided by a GPS receiver onboard the CNES main gondola, as during previous campaigns.

[9] The balloons flew in the lower tropical stratosphere between typically 19 and 20 km altitude ($\sim$ 55–65 hPa) (see flight-mean statistics in Table 1). The flight trajectories are displayed on Figure 1. During the campaign, the quasi-biennial oscillation (QBO) in the stratospheric equatorial winds reverses at the flight level of the balloons, inducing eastward zonal wind at the beginning of the flight period and westward wind at the end. For some periods, in particular, the QBO signal was weak enough so that the balloons were very sensitive to the residual seasonal cycle and to any wind disturbance (e.g., Rossby-gravity or inertial waves) present in the equatorial lower stratosphere at that time. As a consequence, the balloon trajectories were relatively complicated. Balloon #1 for instance stayed some days over the Indian Ocean close to the Seychelles Islands before being advected over Africa. It was then embedded in the QBO eastward circulation and, respectively, crossed the Indian and Pacific Ocean before experiencing the QBO reversal and flying back

Table 1. PreConcordiasi Balloon Flights

				Flight-Mean Statistics		
Flight	Launch (dd/mm/yyyy)	End (dd/mm/yyyy)	Duration (day)	Altitude (km)	Pressure (hPa)	Density (kg/m^3)
1	8/2/2010	11/5/2010	92	19.8	59.4	0.103
2	19/2/2010	8/5/2010	79	19.3	64.2	0.114
3	21/2/2010	12/5/2010	81	19.6	61.2	0.114

over the Pacific Ocean. The flight ended 3 months after the launch in the South China Sea, northwest of Borneo. Like balloon #1, balloon #2 stayed in the deep tropics. It first made a complete eastward revolution around the Earth and then flew back over the Indian Ocean where the flight ended. Balloon #3 on the other hand drifted southwestwardly toward the subtropics, so that it eventually became advected by the developing midlatitude westerlies of the southern winter.

2.2. Estimation of Gravity Wave Characteristics From the Balloon Observations

[10] In this study, we will essentially use the equations and methodology developed in *Boccara et al.* [2008] to estimate gravity wave momentum fluxes and phase speeds from long-duration balloon observations. Briefly, a (complex) wavelet analysis is used to decompose the observed time series of pressure, wind, and vertical displacement in the time-intrinsic frequency space, and the resulting wavelet coefficients are combined to retrieve the wave packet characteristics. However, as recalled in section 1, this former study essentially dealt with hydrostatic waves ($\hat{\omega} \ll N$), in contrast with what is sought here. A few adjustments were therefore needed to analyze the PreConcordiasi flights, regarding high-frequency oscillations, the estimation of phase speeds, and periods of depressurization, as detailed below.

[11] We must first ensure that the balloon's neutral oscillations about its equilibrium level do not interfere with the gravity wave signals. The pulsation of the balloon oscillations can be theoretically derived by assuming that a fully pressurized balloon keeps its volume constant during these motions (and thus its density too). At first order, the balloon vertical displacement (δz) simply responds to the buoyant forces:

$$\frac{d^2 \delta z}{dt^2} = -g \frac{\rho_b - \rho}{\rho} \tag{1}$$

where g is the Earth's gravity, ρ_b is the balloon density, and ρ is the atmospheric density. Using the perfect gas law to relate the vertical variation of the atmospheric density to those of temperature (T) and pressure (P), and with the help of the hydrostatic equilibrium, one obtains

$$\frac{d^2 \delta z}{dt^2} + \omega_b^2 \delta z = 0 \tag{2}$$

where

$$\omega_b = \sqrt{\frac{g}{T} \left(\frac{\partial T}{\partial z} + \frac{g}{R} \right)} \tag{3}$$

is the angular frequency of the balloon oscillations. In this equation, R is the perfect gas constant per mass unit of air.

The balloon neutral oscillations therefore occur with a higher frequency than the Brunt-Väisälä frequency

$$N = \sqrt{\frac{g}{T} \left(\frac{\partial T}{\partial z} + \frac{g}{C_p} \right)}.$$

Taking a mean value for the vertical gradient of temperature in the lower equatorial stratosphere of 5 K km^{-1} yields $2\pi/\omega_b \sim 2.5$ min. Observations show that the real balloon oscillations are slightly longer, which mainly results from the balloon convecting some air with it during its displacement [*Nastrom*, 1980]. Yet these periods are still shorter than those of the shortest gravity waves in the intrinsic frame of reference (4 min), and the associated signals can thus be essentially separated from the gravity wave ones in the wavelet analysis that we perform to infer the wave characteristics.

[12] In this study, intrinsic phase speeds of gravity wave packets ($\hat{c}$) are directly inferred from equation (6) in *Boccara et al.* [2008] as:

$$\hat{c} = \frac{1}{\bar{\rho} \delta_-} \frac{Re(u'_\| p'^{\star}_w)}{u'^2_\|} \tag{4}$$

with $\bar{\rho}$ denoting the mean density along the flight, $\delta_- = 1 - f^2/\hat{\omega}^2$, p'_w and $u'_\|$, respectively, denoting the complex wavelet coefficients for the Eulerian pressure disturbance and for the wind disturbance in the wave direction of propagation, and $p'^{\star}_w$ denoting the complex conjugate of p'_w. The Eulerian pressure disturbance is inferred from the observed Lagrangian pressure disturbance (p'_l):

$$p'_w = p'_l + \bar{\rho} g \zeta'_b \tag{5}$$

where the balloon vertical displacement (ζ'_b) is obtained from the embarked GPS. This phase speed estimation from the Eulerian pressure perturbation is rendered possible thanks to a 1 order of magnitude improvement in the precision of GPS altitudes (1.5 m for the 2010 flights versus 15 m previously).
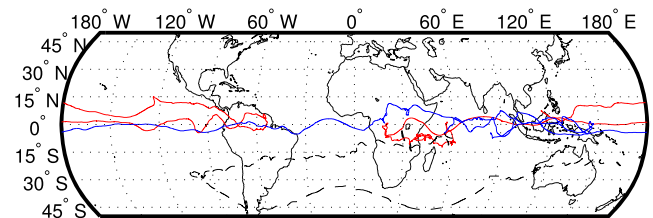
Figure 1. Trajectory of balloon 1 (red), 2 (blue), and 3 (dashed black) in the lower stratosphere during the PreConcordiasi campaign (February–May 2010).
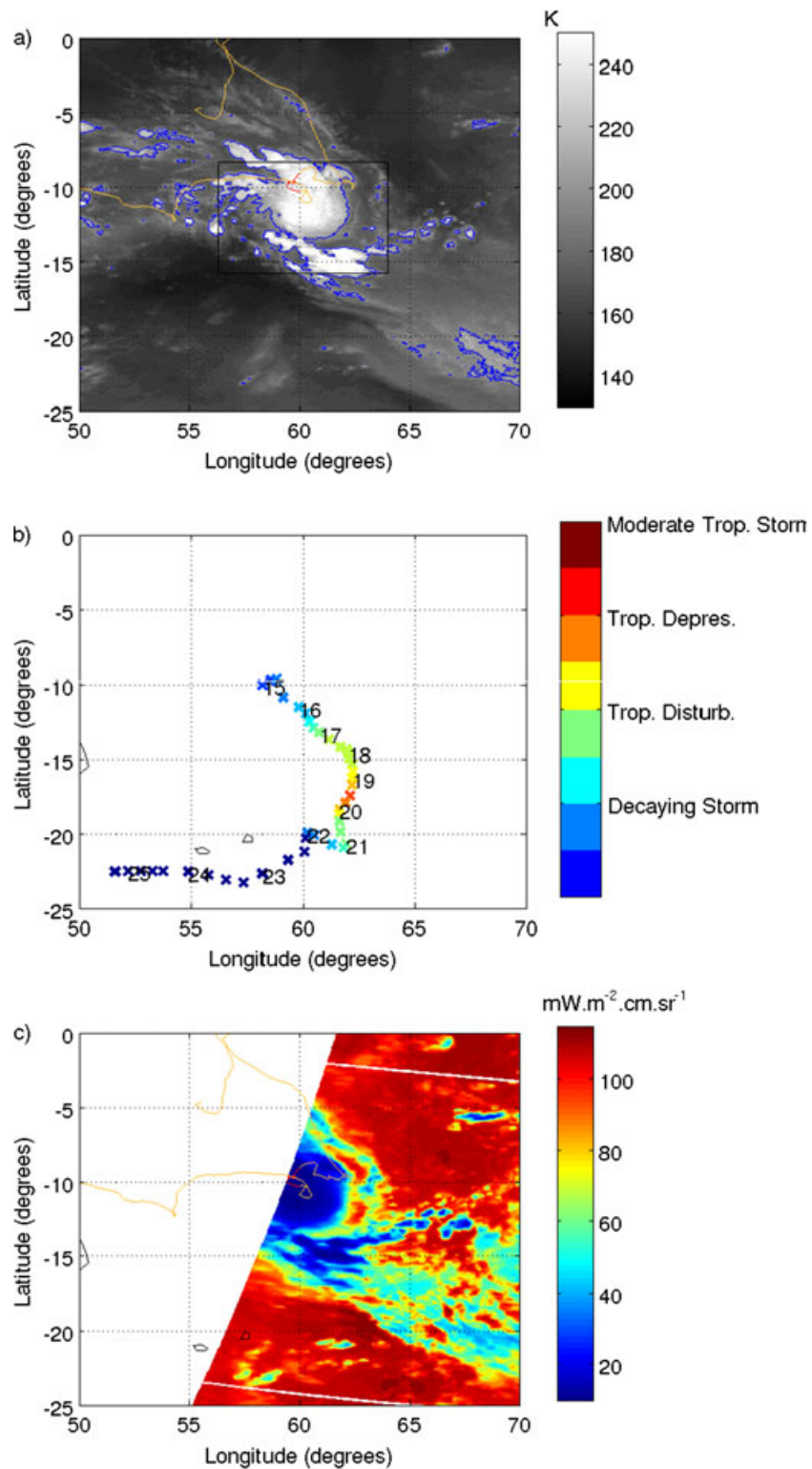
Figure 2. (a) Brightness temperatures in the Meteosat-6 water vapor channel on 15 February 2010 at 2200 UTC. The indicative contour at 200 K is represented in blue. The balloon trajectory on the 15 February 2010 is shown with the red curve, while the extended trajectory is denoted by the yellow curve. The black square corresponds to one of the domain used in the numerical simulation, later referred to as D03. (b) Tropical Cyclone Gelane track with the corresponding Southwest Indian Ocean Tropical Cyclone scale category and dates. (c) Atmospheric Infrared Sounder (AIRS) radiances at 2100 UTC for channel 763 (tropospheric channel), balloon trajectory during the 15 February 2010 (red line), and extended trajectory (yellow).

Table 2. Domain Setup

Domain	D01	D02	D03	D04
Grid dimension (x, y)	70×70	151×151	271×271	346×346
Horizontal resolution (km)	27	9	3	1
Vertical levels (z)	121	121	121	121
Integration time (UTC)	0000–2400	0000–2400	1800–2400	1800–2400
Output frequency (min)	30	30	30	1

Tests performed on synthetic time series including measurement noise have shown that the phase speeds are estimated with a 1-σ uncertainty of 9 m s^{-1}. The wave packet horizontal wavelengths are then obtained as $\lambda_h = 2\pi \hat{c}/\hat{\omega}$, and the vertical wavelengths are finally estimated from the gravity wave dispersion relation.

[13] Last, it is necessary to evaluate the impacts of balloon depressurization on the estimation of gravity wave characteristics. Specifically, the case study presented below occurred on 15–16 February 2010, when balloon #1 flew over the Intense Tropical Cyclone Gelane over the western Indian Ocean (see section 3). Besides disturbances in wind and pressure time series, this period is also characterized by a sudden drop of the balloon superpressure, which eventually vanishes for 15 h, between 1200 UTC on the fifteenth and 0300 UTC on the sixteenth. This depressurization event constitutes another difference with the previous work of *Boccara et al.* [2008]. During these periods, actually, the balloon density is no longer constant, since the balloon volume may vary. These periods typically occur when the balloons fly over areas of organized deep convection as the upward infrared flux impinging on the balloon envelope becomes very weak, cooling the lifting gas and consequently lowering its pressure. Now, the estimation of the gravity wave momentum fluxes in *Boccara et al.* [2008] relies on the balloon drifting on constant-density surfaces and may therefore be biased during depressurization events. The effect of depressurization events on the momentum flux estimates is assessed in Appendix A, where it is shown that momentum fluxes are likely overestimated during such periods, but with no more than a factor 2.

3. Overall Description of the Case Study

[14] We focus our case study on late 15 February 2012, during the early development stage of Tropical Cyclone Gelane. Balloon 1 flew over the main convective core of the Tropical Storm during that period (Figure 2a). The storm track and the corresponding Southwest Indian Ocean Tropical Cyclone scale category are represented on Figure 2b.

3.1. Meteorological Situation

[15] On 15 February 2010, Météo France announced the formation of Tropical Disturbance 12 approximately 1200 km northeast of La Réunion island. During the following hours, the storm continued to develop and drift south-southeasterly as deep convection concentrated vorticity near the core, was then classified as Moderate Tropical Storm, and renamed Gelane. Satellite observations of atmospheric water (Figure 2c) reveal that on 15 February 2010, episodic cellular convection occurred on the upshear side (eastern half) of the storm, in the core and outer bands. The storm intensified, reaching Severe Tropical Storm intensity on 17 February and becoming an Intense Tropical Cyclone on 18 February. When the system reached its peak intensity on 19 February, the minimum sea level pressure was 930 hPa at the core of the Cyclone. Then, finally, turning to the west and moving toward Madagascar, the remnants of Gelane quickly dissipated ∼ 200 km under the effects of the increasing vertical wind shear.

3.2. Model Setup

[16] We investigate the stratospheric gravity waves generated by this Tropical Storm through a numerical simulation with the Weather Research and Forecast (WRF) Model [*Skamarock et al.*, 2008]. WRF is a nonhydrostatic compressible mesoscale model well suited for studying convectively generated gravity waves. The horizontal grid uses Arakawa-C staggering, and the vertical coordinate is terrain following. Time integration uses a third-order scheme with small time steps for acoustic and gravity waves [*Wicker and Skamarock*, 2002].

[17] Two-way nesting is used to perform high-resolution model integrations (see Table 2). Hereafter, the domains with horizontal grid spacings of 27, 9, 3, and 1 km are referred to as D01, D02, D03, and D04, respectively. The domains are centered on 60°E, 10°S, which corresponds to

Table 3. Model Physics

Model Physics	References
Morrison double-moment microphysics	*Morrison et al.* [2009]
Kain-Fritsch convective scheme (for D01 and D02 only)	*Kain* [2004]
Yonsei University planetary boundary layer scheme	*Hong and Pan* [1996]
MM5-derived surface layer scheme	*Skamarock et al.* [2005]
Noah land surface model	*Chen and Dudhia* [2001]
Rapid radiative transfer model for longwave radiation	*Mlawer et al.* [1997]
Dudhia shortwave radiation scheme	*Dudhia* [1989]
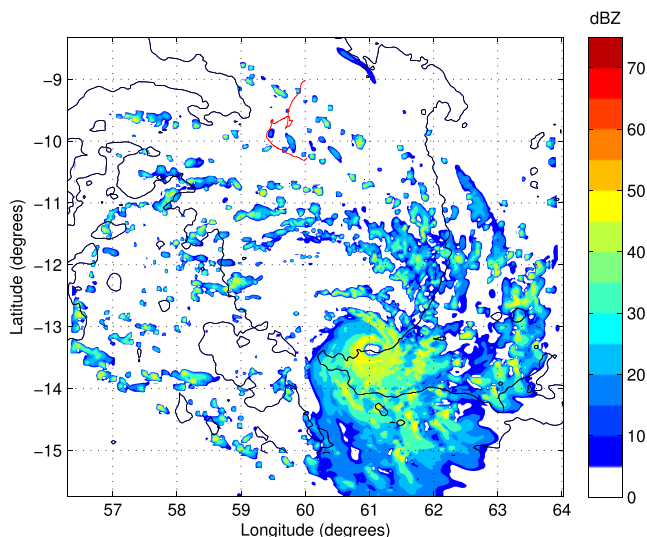
Figure 3. Simulated radar reflectivity in D03 at 2200 UTC and balloon trajectory on 15 February 2010 (red line). The overlaid black contour is the blue contour on Figure 2a and represents an estimation of the main convection system associated with Gelane as observed by Meteosat-6.

the mean location of the simulated storm core. This positioning was performed manually and was based on previous test simulations. From the coarser to the finer, the domains, respectively, have dimensions of 70 × 70, 151 × 151, 271 × 271, and 346 × 346 grid points. Each nested domain contains 120 vertical levels from the surface to the model top, chosen as 6 hPa and corresponding to an approximate altitude of 35 km. We prescribe a sponge layer effective in the upper 7.5 km below the domain top, using Rayleigh damping on the vertical velocity to avoid wave reflections on the model top. A few tests were necessary to determine the optimal thickness of this layer.

[18] The physical schemes are summarized in Table 3. For example, convection is explicitly simulated in D03 and D04 while it is parameterized in the two first domains using the Kain-Fritsch scheme [*Kain*, 2004]. This scheme showed good results when simulating Tropical Storms [*Gentry and Lackman*, 2006]. Moreover, we used the Morrison double-moment microphysics scheme because it includes graupel and ice and the associated processes necessary to simulate convection at cloud-scale.

[19] The reference simulation covers the 24 h period from 15 February 2010 at 0000 UTC to 16 February 2010 at 000 UTC. The model first ran on D01 and D02 until 1800 UTC; at which time, all four domains were run together for the last 6 h. In the rest of the study, we will focus on the period from 2030 to 2400 UTC (i.e., after the spin up of the flow in D03 and D04). The atmospheric initial conditions and boundary conditions for D01 were provided by the European Centre for Medium-Range Weather Forecasts (ECMWF) operational analyses. These analyses are available at 0000, 0006, 1200, and 1800 UTC every day. They have a horizontal resolution of 0.25° corresponding to an approximate grid spacing of 20–25 km, and 91 model levels in the vertical, with a higher resolution near the

surface. In addition, we have performed another run with D03 and D04 starting at 1200 UTC, in order to test the sensitivity to the model spin-up in those domains. Unless stated otherwise, we only discuss below results from the reference simulation.

[20] It was furthermore found necessary to carefully initialize the model run with data assimilation of satellite radiances complementing the information from the ECMWF analyses. Preliminary cold start initialization tests with data provided only by ECMWF did not successfully simulate the Tropical Cyclone (probably because of insufficient use of the complete set of fields by WRF, like the cloud liquid water, for example). Hence, satellite radiances from the NOAA Advanced Microwave Sounding Unit B (AMSU-B) [*Aumann et al.*, 2003; *Fetzer et al.*, 2003] before the run period were assimilated through intermittent assimilation cycles on the D01 grid to initialize the model with realistic convection. AMSU-B is a microwave radiometer onboard near-polar orbiting satellites, which measures the atmospheric humidity profile and complements the temperature sounding instruments AMSU-A and High-Resolution Infrared Radiation Sounder/3. The assimilation is performed with the WRF Data Assimilation 3DVAR package (WRFDA-3DVAR) [*Barker et al.*, 2004]. We perform the first 3DVAR assimilation cycle on 14 February at 0600 UTC, and then, cycle it every 6 h until 15 February at 0000 UTC. In contrast with numerous other studies focusing on Hurricane simulations, we therefore did not use a bogus vortex [*Singh et al.*, 2005] to force the circulation at the initial time. However, we note that assimilation of AMSU-B here was the key element to simulate convection comparable to that observed in the Meteosat-6 and AIRS data.

3.3. Simulated Storm and Model Validation

[21] Figure 3 shows the simulated radar reflectivity in D03 at 2200 UTC to identify deep moist convection associated to the developing Tropical Storm. The simulated storm shows the typical features of a real Tropical Storm, with converging winds near the surface (not shown), a cloud-free core, eye-wall clouds overshooting at an altitude of about 15 km, and spiraling rainbands, denoted by the strong reflectivity cores outside the storm core. Moreover, the simulated values of 35 dBZ with maxima of 55 dBZ are typical values of radar reflectivity for Tropical Storms and Tropical Cyclones. For comparison, those values are usually between 55 and 70 dBZ in classical monocellular or multicellular convective storms.

[22] In D01, the Tropical Storm intensifies slowly immediately after the beginning of the run and starts to drift south-southeasterly with a speed of 5 m s^{-1}. In D02, D03, and D04, the Tropical Storm intensifies more rapidly than observed by Météo France and already reaches Severe Tropical Storm intensity by the end of 15 February. The Storm speed of displacement is realistic and appears to be of the same order than that of the real storm. Nonetheless, the simulated core is located 100–150 km south-southeasterly of its observed location. Cyclone trajectories are notoriously difficult to predict [e.g., *Plu*, 2011, and references therein], and this should not hinder the comparison below. The position and characteristics of the storm remain essentially unchanged in the simulation with the longer spin-up for D03 and D04.
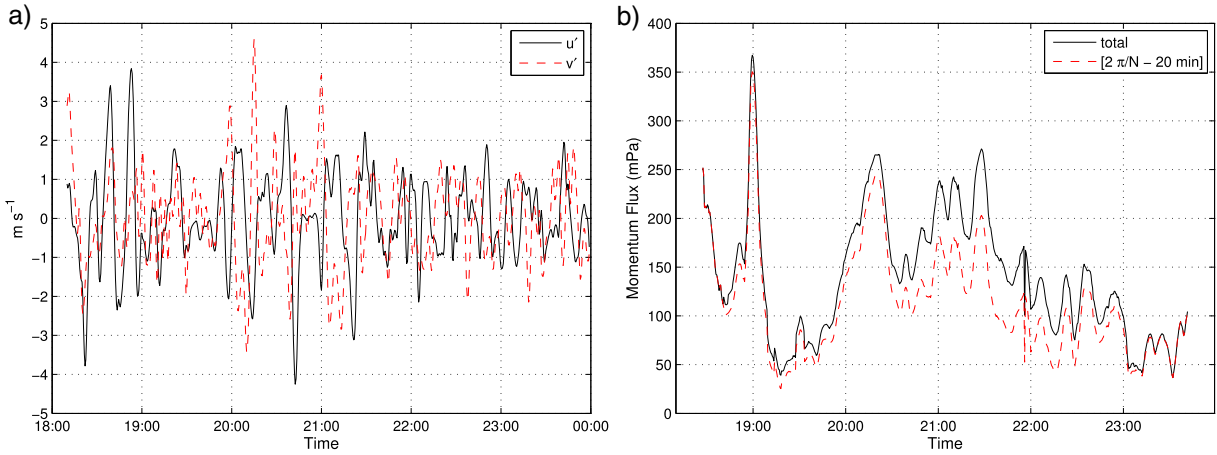
Figure 4. (a) u' (black) and v' (dashed red) perturbation velocities time series as measured by the first balloon on 15 February 2010. (b) Instantaneous momentum flux computed using the first balloon data during the Tropical Storm phase (solid black). We have represented the contribution of CGWs with $\hat{T} = [2\pi/N, 20 \text{ min}]$ by the dashed red line.

4. Gravity Waves Associated With Gelane Tropical Storm

4.1. Estimates From the Balloon Observations

[23] In what follows, in order to compare the simulation with the balloon observations, we provide a first estimate of the CGW characteristics from a straightforward graphical analysis of the balloon time series. A more quantitative analysis, using wavelets, is presented afterward. In contrast to *Plougonven et al.* [2008], which investigated a single orographic wave, making pointwise comparisons possible, here we aim at deriving the typical amplitudes and characteristics of multiple wave packets.

4.1.1. Description of the Waves in the Balloon Observations

[24] Time series of zonal (u') and meridional (v') wind perturbations observed by balloon #1 on 15 February 2010 are displayed on Figure 4a. They have been obtained by filtering the raw time series with a band-pass filter with cutoff periods at 5 min and 24 h. The filtered time series exhibit disturbances with intrinsic periods ($2\pi/\hat{\omega}$) around 10–12 min, i.e., slightly more than twice the Brunt-Väisälä period, therefore indicative of gravity waves. As in *Plougonven et al.* [2008], an analysis of the characteristics of the waves in the balloon observations is now done with the help of the polarization and dispersion relations for gravity waves. We use standard notations and decompose the perturbation fields a' into monochromatic plane waves:

$$a' = \text{Re}\left(\tilde{a}e^{i(kx+ly+mz-\omega t)}\right) \tag{6}$$

where Re stands for the real part, $\tilde{a}$ is the complex amplitude of a', (k, l, m) are the zonal, longitudinal, and vertical wave numbers, and ω is the definite positive absolute frequency. With a Coriolis parameter nearly vanishing in the deep tropics, the polarization relations for 2-D linearly polarized gravity wave read [*Fritts and Alexander*, 2003; *Plougonven et al.*, 2008]:

$$\tilde{u} = \frac{k}{l}\tilde{v} \tag{7}$$

$$\tilde{w} = \frac{m\hat{\omega}}{N^2 - \hat{\omega}^2}\tilde{p} \tag{8}$$

$$\tilde{\zeta} = -i\frac{\hat{\omega}}{N^2}\frac{m}{k}\tilde{u} \tag{9}$$

where $(\tilde{u}, \tilde{v}, \tilde{w}, \tilde{\zeta})$, respectively, stand for the complex amplitudes of the velocity perturbations in the zonal, longitudinal, and vertical directions, and of the height perturbations. Here the terms involving the scale height H in *Fritts and Alexander* [2003] are neglected because the vertical wavelengths, of typically the order of the diabatic heating scale, i.e., ~ 10 km, are assumed to be small with respect to $4\pi H$.

[25] It is possible to estimate the wave propagation direction k/l in the horizontal plane using equation (7) and the series of u' and v' for the considered period. Throughout the considered period, calculated values of the counterclockwise angle from the East are found within a range from ~ 0° at 1800 UTC to ~ –60° from 2000 to 2400 UTC. Furthermore, following equation (7), the horizontal compo-
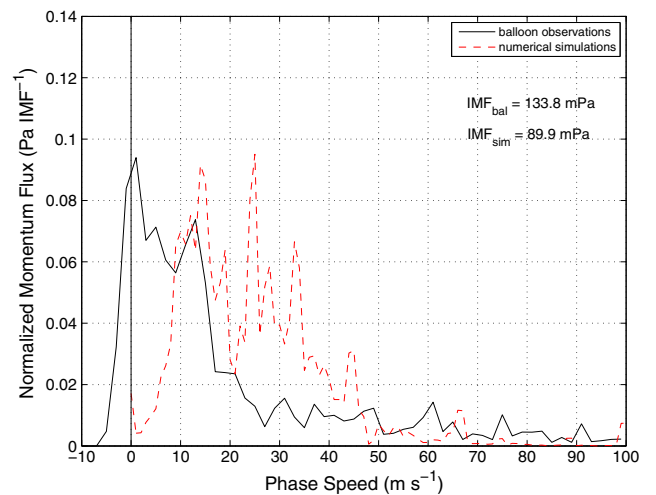
Figure 5. Ground-relative phase speeds associated with convective gravity waves in the balloon observations (black solid) and in the simulation (dashed red).
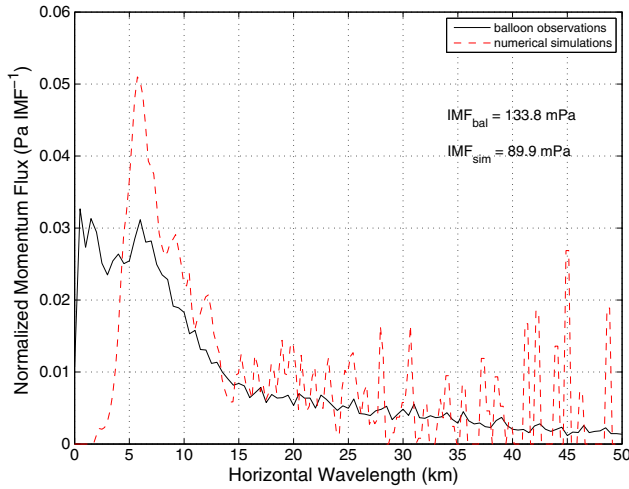
Figure 6. Horizontal wavelength spectra associated with convective gravity waves in the balloon observations (black solid) and in the simulation (dashed red).

nents of the velocity perturbations are in phase opposition, and this is observed in the time series of Figure 4 between 2000 and 2130 UTC, for example. Calculating a typical squared Brunt-Väisälä frequency of 7.5×10^{-4} s^{-2} (period of $\sim$ 4 min) from the ECMWF reanalysis along the balloon trajectory, and using equation (8) and w' and p' time series (not shown), we can estimate a typical vertical wavelength as $\lambda_z \sim 6$ km. Finally, we retrieve a horizontal wave number by using the dispersion relation:

$$\hat{\omega}^2 = \frac{N^2 k_H^2}{k_H^2 + m^2} \qquad (10)$$

with $k_H^2 = k^2 + l^2$. We find a value of 6.4×10^{-4} m^{-1}, yielding an horizontal wavelength of $\sim$ 10 km. Using equation (9) and considering the period when the propagation angle is constant and $\sim -60°$ (i.e., past 2000 UTC), we can finally calculate a typical height perturbation amplitude $\tilde{\zeta} \sim 200$ m.

4.1.2. Wavelet Analysis of the Balloon Data

[26] After the preliminary estimate of wave characteristics described above, we now carry out a systematic examination of the waves using wavelet analysis (section 2.2 and Appendix A) which provides estimates of the momentum fluxes, of phase speeds, frequencies, and wavelengths.

[27] The time series of the absolute momentum fluxes due to gravity waves obtained from the balloons with the wavelet analysis are shown in Figure 4b (solid black line). We note strong variations on timescales less than an hour with peaks exceeding 150 mPa.

[28] The wavelet analysis identifies wave packets and provides estimates of their intrinsic frequency. In order to quantify the contribution of high-frequency gravity waves to the total instantaneous momentum flux, we also show in Figure 4b the contribution of the waves with intrinsic periods shorter than 20 min (dashed red line). This clearly shows that most of the momentum flux (about 80%) is carried by the gravity waves with highest intrinsic frequencies.

[29] The wavelet analysis also provides estimates of the waves phase speeds and wavelengths. This information is used to describe the gravity wave momentum fluxes as a function of phase speed and horizontal wavelength, with bins of respective width $\Delta c = 2$ m s^{-1} and $\Delta\lambda_H = 500$ m. The ground-based phase speeds and horizontal wavelengths spectra of momentum fluxes are displayed in Figures 5 and 6 (solid black lines). The major part of momentum fluxes is accounted for by waves with phase speeds within a range of 0 to 50 m s^{-1}, and horizontal wavelengths within a range of 1 to 50 km. Both momentum flux distributions have two modes. The characteristics of the mode that carries the most momentum flux are summarized in Table 4 for comparison with the numerical simulations. These characteristics are in fair agreement with the first estimates provided in the previous section, both emphasizing short horizontal wavelengths: $\lambda_H \lesssim 10$ km.

4.2. Simulated Gravity Waves

[30] We now turn to the numerical simulations and aim at comparing the gravity waves emitted by Gelane in the simulations with those derived from the balloon observations.

4.2.1. Description of the Waves in the Numerical Simulation

[31] In this section, we first describe the simulated waves in physical space, relative to the large-scale flow structure, then examine their characteristics as a function of phase speeds and wavelengths.

[32] In Figure 7, we have represented horizontal cross sections of the vertical wind velocity and horizontal velocity vector at 2030 and 2210 UTC, 15 February 2010 in D04 at 7 and 19 km, the latter corresponding to the mean altitude of the balloon during the storm period. Figures obtained from the simulation with a longer spin-up for D03 and D04 are very similar. Whereas in the troposphere, the signature in vertical velocity is fairly isotropic; in the lower stratosphere, we clearly see the main gravity waves east of the core, located in a region delimited by 12.5°S, 13.5°S, and 60.5°E–61.5°E and also a small region northwest of the core. We notice a wavefront propagating away radially from the wall cloud around the core at a speed of 25 m s^{-1} on the eastern half side of the storm, surrounded by wave packets with smaller amplitude and horizontal scale. The majority of the waves propagate against the mean easterly flow. This result is consistent with previous theoretical studies on the propagation of gravity waves in sheared flows [*Beres et al.*, 2002]. A graphical estimation of the typical horizontal wavelengths yields $\lambda_H \sim 12$–20 km (i.e., 12–20 δx, indicating that the waves are well resolved).

[33] In Figure 8, we show the cross section of the vertical velocity along the black line of Figure 7b at 2330 UTC. Vertically propagating gravity waves emitted by the wall cloud are seen on the flanks of the core with a larger amplitude on the upshear side of the storm, consistently with previous remarks. Above the core, the phase lines are nearly verti-

Table 4. Characteristics of the Dominant Mode From the Balloon Data and the Simulation

	Balloon Observations	Numerical Simulation
λ_H (km)	1	6
ω	0.2 N	0.5 N
T (min)	16	7
c (m s^{-1})	1	14
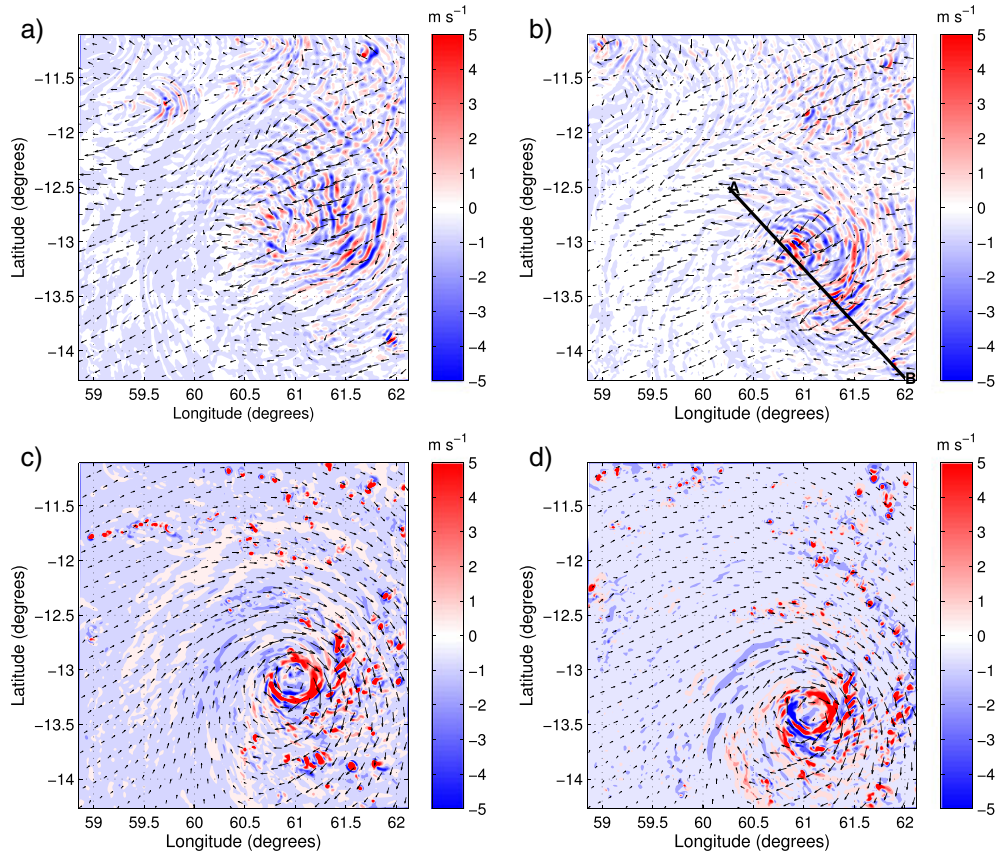
Figure 7. Vertical velocity (filled contours) and horizontal velocity vector (a) at 2030 UTC at 19 km of altitude and (c) at z = 7 km with overlaid reflectivity contour at 25 dBZ (black line). (b and d) Same as Figures 7a and 7c represented at 2210 UTC. The AB oriented line shows the slice used in subsequent figure.

cal. Those waves appear vertically trapped, and they do not carry much momentum flux vertically. As highlighted by *Lane and Knievel* [2005], increasing the resolution favors the appearance of phase lines on the flanks that are nearly vertical, indicating trapped waves. We estimate the vertical wavelength to be ~ 10 km. Using the dispersion relation for the gravity waves [*Fritts and Alexander*, 2003] and using the same previous mean value of N in the lower stratosphere above the storm yields $\hat{\omega} \sim N/\sqrt{2}$, equivalent to an intrinsic period as short as ~ 6 min.

[34] We also provide an estimation of the amplitude of the wind perturbations from the simulated field. We find $|\tilde{w}| \sim 2 - 3$ m s^{-1} at 19 km above ground level (AGL). Similarly, we get $|\tilde{u}| \sim 2$–4 m s^{-1} and $|\tilde{v}| \sim 2$–4 m s^{-1} for the horizontal zonal and meridional velocity perturbations. Those values are consistent with direct graphical estimations from the balloon time series and with a high-frequency wave.

4.2.2. Momentum Fluxes in the Simulation

[35] We have seen that the basic gravity wave characteristics derived from the numerical simulation are in agreement with those assessed from the balloon data. In the following paragraph, we carry out a more systematic calculation and comparison of the momentum fluxes from the model outputs to compare them with the momentum fluxes calculated in section 4.1.2.

[36] The momentum fluxes are calculated from the model outputs in a similar manner as in Plougonven et al. (submitted manuscript, 2012). The total wind components and the air density are interpolated at $z = 19$ km for
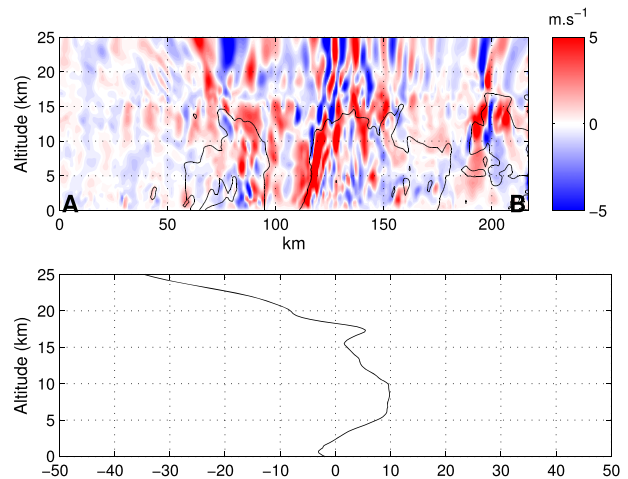
Figure 8. (top) Vertical cross section of vertical velocity (shaded contours) and reflectivity contour at 25 dBZ (black contour) along the black line on Figure 7b. (bottom) Vertical profile of the zonal velocity averaged along the vertical slice.
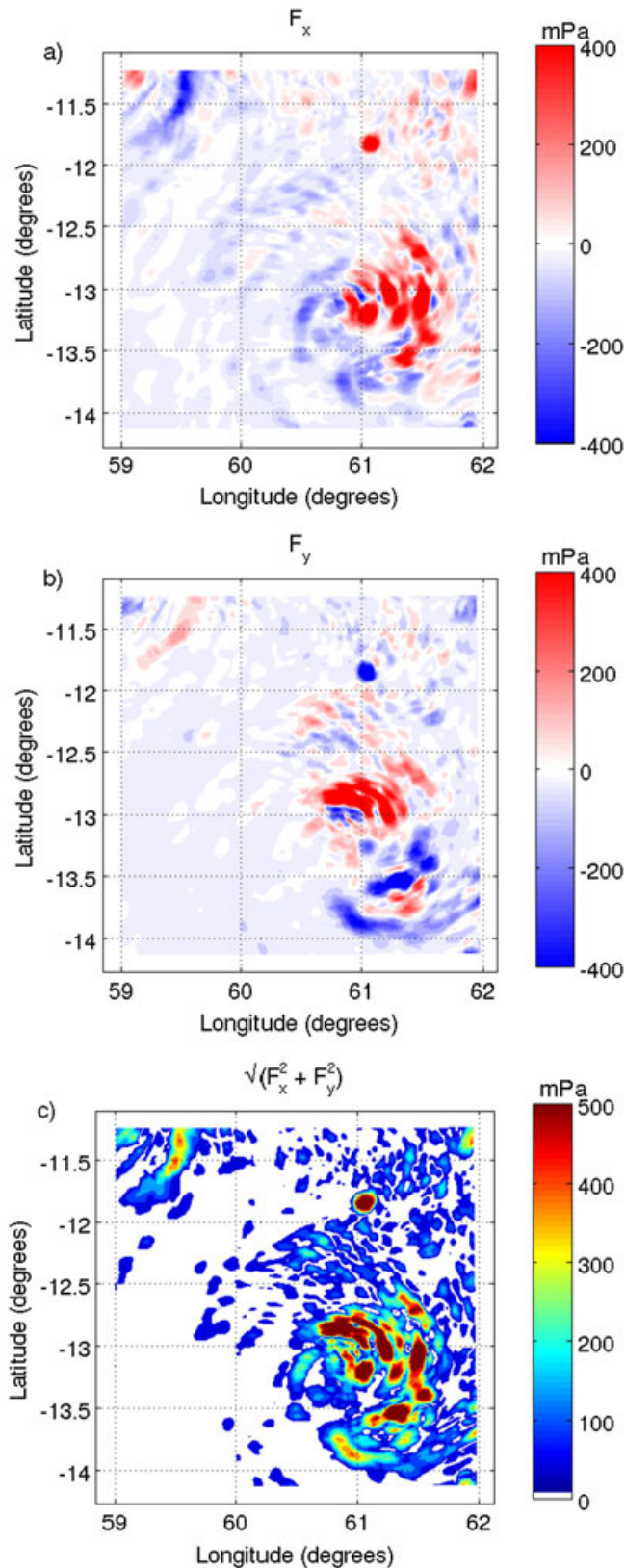
Figure 9. (a) Zonal, (b) meridional, and (c) absolute momentum fluxes in the numerical simulations on 15 February 2010, 2210 UTC, at 19 km.

comparison with the balloon. Then the wind perturbations fields are obtained at each output time step by removing the mean value over D04. We have tested removing a more local definition of the mean wind (e.g., with a 25 km averaging window). The resulting momentum fluxes are somewhat weaker and more localized. The amplitude and location of the maximum fluxes remain the same. Hence, we have preferred to keep the simplest definition for the mean flow to be removed. Zonal and meridional momentum fluxes are calculated as $\rho u'w'$ and $\rho v'w'$, respectively, and are subsequently smoothed with a 15-point averaging window.

[37] Figure 9 shows the momentum fluxes in the zonal and meridional directions calculated directly from the output velocity perturbations at 19 km AGL. The distribution of the zonal flux is highly directional as evidenced by the positive values in the eastern quadrant and the negative values mostly located on the western quadrant of the storm. The meridional distribution is also anisotropic, and the shift is parallel to the velocity vector at 19 km, as expected from the depiction of the waves in the vertical cross section.

[38] Absolute momentum flux at 19 km at 2200 UTC is represented in Figure 9c. We note that most of the momentum flux is located on the upshear side of the storm, and this is in agreement with *Sato* [1993] that stated that the maximum of the flux is on the leading side of the developing storm. This also suggests consistency with the argument of *Kuester et al.* [2008] who stated that 50% of the momentum flux emitted by a Hurricane during its lifetime is eastward flux. Our study only covers a period during the development of the cyclone; for that period, we calculate a value of 60%.

[39] In a previous case study comparing balloon-borne observations and mesoscale simulations of an orographic gravity wave, observed and simulated time series of wind and temperature along the balloon trajectory were found to agree [*Plougonven et al.*, 2008]. This was possible because the source of the wave was the orography (the Antarctic Peninsula), hence immobile and well known. For CGWs, the source of the waves is convection in the developing cyclone which, being itself simulated, unavoidably differs from the observed cyclone: we have previously seen a bias in the storm core location between the simulation and the satellite representation of convection. Hence we choose to compare the general aspect of time series from the simulations in a location comparable to that of the balloon relative to the storm core. In other words, since the balloon is located about 150–200 km north-northwesterly of the core, we illustrate the gravity waves by a local time series of momentum fluxes in D04 in a region 150–200 km north-northwesterly of the simulated core (61°E, 12°S). We have tested the sensitivity to the location chosen, within half a degree in all four directions, and have found that all time series are qualitatively similar. These time series (e.g., Figure 10) share qualitative similarities to that from the balloon data: maxima of momentum fluxes occur in short bursts (less than an hour) with about three large amplitude events in the time window analyzed, having values up to 100–250 mPa.

4.2.3. Spectral Characteristics

[40] In this section, we calculate the phase speeds and horizontal wavelengths spectra of momentum fluxes using the numerical simulation to compare them to the spectra derived from the balloon data in section 4.1.2.
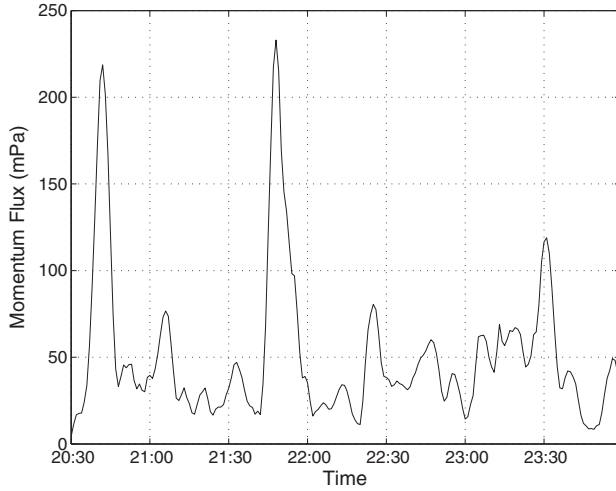
Figure 10. Time series of the momentum flux for the simulated CGWs at 61°E, 12°S.

[41] In order to perform a spectral analysis on the outputs as in *Kuester et al.* [2008], we compute the cospectra of (u', v') with w' as:

$$Co_x = Co(u'w') = \mathrm{Re}\left(UW^*\right) \qquad (11)$$

and

$$Co_y = Co(v'w') = \mathrm{Re}\left(VW^*\right), \qquad (12)$$

where (U, V, W) are the Fourier transforms of (u', v', w') and W^* is the complex conjugate of W. These 3-D (k, l, ω) cospectra are then transformed into 1-D (c or λ_H) cospectra and normalized so that they are in spectral density unit: respectively, $\mathrm{m^2\ s^{-2}}/\Delta c$ and $\mathrm{m^2\ s^{-2}}/\Delta\lambda_H$. The same values as in section 4.1.2 were used, i.e., $\Delta c = 2\ \mathrm{m\ s^{-1}}$ and $\Delta\lambda_H = 500$ m. The absolute momentum spectra are then obtained by summing the zonal and meridional components:

$$F(c) = \frac{1}{2}\bar{\rho}_0\sqrt{Co_x(c)^2 + Co_y(c)^2} \qquad (13)$$

and

$$F(\lambda_H) = \frac{1}{2}\bar{\rho}_0\sqrt{Co_x(\lambda_H)^2 + Co_y(\lambda_H)^2}, \qquad (14)$$

where $\bar{\rho}_0$ is the density averaged over the entire time and domain.

[42] We retrieve the mean integrated momentum flux (IMF) by integrating the latter over all the phase speeds or horizontal wavelengths:

$$\mathrm{IMF} = \int_c F(c)\mathrm{d}c = \int_{\lambda_H} F(\lambda_H)\mathrm{d}\lambda_H, \qquad (15)$$

i.e., the averaged momentum flux over the whole innermost domain (D04) throughout the developing storm period.

[43] As mentioned by *Kuester et al.* [2008], this Fourier analysis approach with the model outputs needs confirmation by verifying the consistency of the sampling rate. The Nyquist frequency should be at least twice the frequency of the highest waves frequency. Here the Nyquist frequency is approximately $0.1047\ \mathrm{s^{-1}}$; therefore, the expected frequency

of the highest waves frequency should be on the order of 1–$3 \times 10^{-2}\ \mathrm{s^{-1}}$. This value corresponds to a near Brunt-Väisälä frequency, as calculated from the ECMWF reanalysis, so the chosen Nyquist frequency is appropriate to sample the high-frequency part of the spectrum of the gravity wave activity. The maximum wavelength in the simulation is constrained by the domain size (about 350 km), and the minimum wavelength (2 km) is imposed by the minimum grid spacing.

[44] For the simulations, the distributions of momentum fluxes as a function of phase speed, $F(c)$, and wavelength, $F(\lambda_H)$, are represented on Figures 5 and 6 (dashed red lines). Most of the simulated momentum flux is associated with waves with phase speeds from 5 to 50 m s^{-1}, and horizontal wavelengths between 3 and 20 km (although some signals appear up to 50 km). Waves with wavelengths from 3 to 20 km carry about two thirds of the total momentum flux. The dominant mode has a horizontal wavelength of 6 km with an intrinsic frequency of 0.5 N (period of 7 min) and a ground-relative phase speed of 14 m s^{-1}. As stated earlier, this frequency is very close to the Brunt-Väisälä frequency. The spectral characteristics of the dominant mode of the simulated gravity waves are summarized in Table 4. One should note and keep in mind that, with a grid spacing of 1 km, a wavelength of 6 km corresponds to the minimum resolved scale.

4.3. Further Comparison

[45] The sections 4.1 and 4.2 have shown a reasonable agreement between the observed and simulated CGWs during the early development of Tropical Storm Gelane. We here provide additional informations to push the comparison further, and discuss the limitations of such comparison.

[46] In Table 5, we show the values of the IMF and the standard deviation σ of the fluxes calculated from the balloon data and the numerical simulation. The IMF and the standard deviation in the observations compare fairly well with those in the numerical simulations, with an underestimation in the simulations (which can also be seen by comparing Figures 4 and 10). Actually, we do not expect a perfect match between those values because of the limitations making a precise comparison difficult: sampling of the balloon observations (very localized, in the vicinity of the storm, potential overestimation of the flux when the balloon is over the storm) and averaging domain in the simulations (which both includes the storm and quiescent regions).

[47] The momentum flux distributions estimated with the observations and simulations (Figures 5 and 6) shows encouraging similarities: both emphasize short wavelengths ($\lesssim 10$ km) and agree regarding the importance of phase speeds between 5 and 20 m s^{-1}. However, significant discrepancies are also found. Regarding the distribution of momentum fluxes as a function of horizontal wavelength, discrepancies are found for short wavelengths ($\lesssim 5$ km)

Table 5. Comparison of the Observed and Simulated CGWs Characteristics

	Balloon Observations	Numerical Simulation
IMF (mPa)	133.8	89.9
Flux standard deviation (mPa)	69.4	42
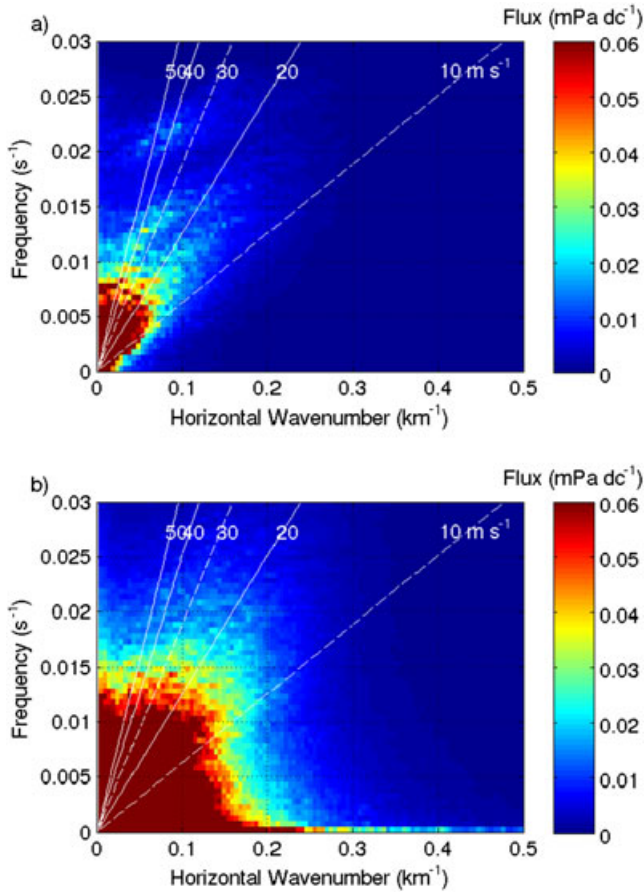
Figure 11. Momentum flux with respect to frequency and horizontal wave number (a) at z = 19 km and (b) at z = 15 km.

and also for long wavelengths (isolated peaks found in the simulations, not in the observations). The latter, isolated peaks simply results from the Fourier analysis (no smoothing was applied to the Fourier transform of the WRF fields). At shorter wavelengths, one needs to compare the two curves cautiously. In the simulations, wavelengths shorter than 6 km are absent because of the limited resolution of the simulations (the minimum resolved wavelength is $\sim 6 \Delta x$). In fact, we have calculated this spectrum from the output of domain D03 (where $\Delta x = 3$ km) and have found a broader peak around 15 to 30 km. Hence, the agreement found for the peak near $\lambda_h = 6$ km may be partly fortuitous, resulting from some unresolved scales being aliased onto the minimum resolved scale. Nonetheless, both curves agree quite encouragingly down to this minimum scale, with a strong contrast between weak momentum fluxes for wavelengths larger than 15 km, and stronger values for wavelengths shorter than 15 km. The simulated fluxes are very sensitive to resolution and further investigation at higher resolution would be necessary to reach firm conclusions. More worrisome are the discrepancies in the distribution as a function of phase speeds: The observed maximum fluxes are for nearly stationary waves, whereas the simulations have nearly no momentum fluxes associated with phase speeds less than 5 m s^{-1}. This is too great a difference to be explained simply by the limited sampling of the wavefield by the balloon. (The other

differences, i.e., the simulations emphasizing larger phase speeds than the observations, can reasonably be due to the different sampling.) The absence of waves with near-zero phase speeds in the simulations suggest that these may have been filtered by the wind, which displays a reversal between 15 and 20 km (see Figure 8; wind profiles averaged over the whole domain are similar). To verify that this is indeed the case, Figure 11 displays the 2-D distribution of simulated momentum fluxes in the horizontal wavelength/frequency plane at two altitudes: 15 and 19 km. Gravity waves with near-zero phase speeds are clearly present at 15 km and constitute a significant portion of the wave field. At 19 km, on the other hand, these waves have been filtered out, and only phase speeds of about 10 m s^{-1} or larger remain. This underlines an essential difficulty in comparing high-resolution numerical simulations and observations: the mesoscale simulations rely on analyses for their initialization. However, the analyzed winds in the Tropics have larger uncertainties than in the midlatitudes, due to the paucity of tropical observations as well as the absence of a balance to relate the wind and the mass distribution (which is observed by spaceborne instruments). The simulations can therefore suffer from significant biases in the background state, which can impact the convection organization and the wave propagation in the model.

[48] We have also examined how the model resolution affects the simulated convection and the CGW momentum fluxes. For this, we compared vertical cross sections of vertical velocity and reflectivity, as well as horizontal cross sections of instantaneous momentum flux (not shown) from all three domains, D02, D03, and D04. This cannot be regarded as a "real" sensitivity test to resolution since we used two-way nesting in the simulations. Nonetheless, we notice little difference between the waves in domains 3 and 4, whereas when resolution decreases by a factor 9 (between D04 and D02), the intensity of the updrafts and the magnitude of the waves decreases by a factor 3, as well as the steepness of the phase lines. As discussed by *Lane and Knievel* [2005] and *Kim and Chun* [2010], however, the best method to retrieve GW spectral characteristics from simulations is to use the highest available resolution as the GWs are better resolved with smaller grid spacing.

4.4. Discussion

[49] We now briefly discuss two further issues for which the above analysis of CGW in both observations and simulations may be helpful: (1) Do tropical cyclones, which stand out as the most energetic form of organized convection in the troposphere, have a significant contribution to momentum fluxes toward the lower stratosphere? (2) How do the CGW generated by Gelane appear in satellite observations, which are widely used to analyze gravity waves?

[50] *Kuester et al.* [2008] have described a simple estimation of the CGW momentum flux globally associated to Hurricanes every year in the subtropical lower stratosphere. We adapt their reasoning to our case study. The calculated IMF has a value of approximately 90 mPa, about 60% of which is eastward propagating CGWs. Emphasis is put on the eastward flux here, since the eastward propagating CGWs contribute to the forcing of the positive phase of the QBO observed in February 2010. *Webster et al.* [2005] provide an estimation of a total of 475 Hurricane days per
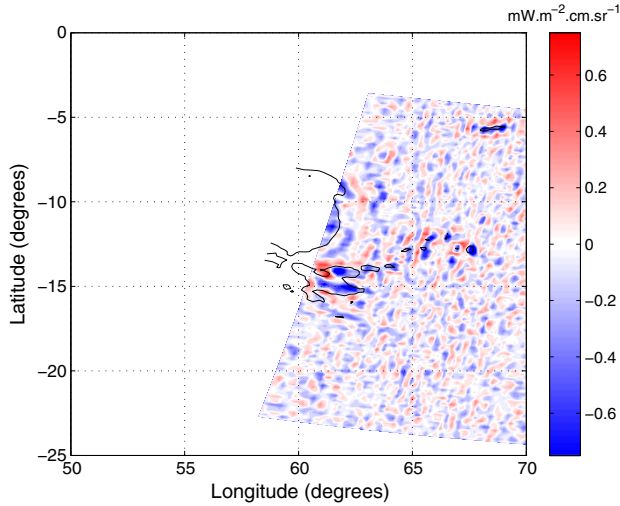
Figure 12. AIRS radiances perturbations at 2100 UTC for channel 149 on the central swath, and AIRS radiance contour at 25 m W^{-2} cm sr^{-1} (in black) to identify the deep convection regions.

year occurring across the globe. The mean zonal Tropical Cyclone momentum flux can be estimated as follows:

$$\overline{F}_{TC} = (90 \text{ mPa})0.6 \left(\frac{475 \text{ days}}{365 \text{ days}} \right) \left(\frac{3.1° \times 3.1°}{360° \times 40°} \right) \approx 4.7 \, 10^{-2} \text{ mPa},$$
(16)

where 3.1° is the size, converted in degrees, of domain D04 over which the IMF was calculated. The factor 3.1°/40° here accounts for an equatorial band with latitude ranging from 20°S to 20°N. The above value has the same order as that mentioned in *Kuester et al.* [2008]. (In their calculation, however, they include only one geometric factor, for the longitudinal extent of the domain. Including also the latitudinal factor would reduce their estimate (5×10^{-2} mPa) by an order of magnitude.) As a matter of comparison to $\overline{F}_{TC}$, *Dunkerton* [1997] and *Scaife et al.* [2000] estimated a value of 3–6 mPa to drive the QBO. Relative to this value, the estimate for $\overline{F}_{TC}$ found above is 2 orders of magnitude smaller. Several limitations and uncertainties of this estimate should be kept in mind: the simulated IMF depends on the model configuration and on the method of calculation. We have tested and found that it is little sensitive to the spin-up time. On the other hand, it does show considerable sensitivity to resolution (60% weaker in D03 than in D04) and the IMF could increase further with higher resolution. On the other hand, the methodology we have used to estimate the momentum fluxes (use of a domain averaged mean wind) will tend to overestimate momentum fluxes. Finally, the simulated IMF compares reasonably well with the observations, but these may underestimate the momentum fluxes due to limited sampling and to the position of the balloon relative to the storm. Note also that the real flux should be higher as we have used the number of cyclone days. Now, our estimate is in fact for a developing cyclone, and previous studies have brought evidence that fluxes were larger for a developing cyclone than for a mature one. If we include Tropical Storm days, using the same value of 90 mPa yields a mean zonal momentum flux of 0.23 mPa. This remains a relatively small contribution to the momentum fluxes needed to drive

the QBO, even if we allow some room for underestimation due to resolution.

[51] The analysis of the wavefield can be qualitatively completed using satellite data, especially for the eastern part of the Storm that was not sampled by the balloon. We have previously shown AIRS radiances at channel 763 (tropospheric channel) on 15 February 2010 (Figure 2c) to reveal episodic cellular convection occurring on the upshear side of the storm. We have seen in the previous sections that such convection associated with a Tropical Storm can emit CGWs in the core and outer bands. We now show AIRS radiance perturbations on channel 149 in Figure 12 to get a planar view of the CGWs from satellite observations. They are calculated by averaging the fields along the satellite track with a 70 km running window, and removing it from the total fields. These perturbations are representative of gravity waves with vertical wavelengths greater than 12 km [*Alexander and Barnett*, 2007], and a coherent pattern of waves stands out on the eastern flank of the storm in this channel. Caution is, however, needed because the width of the channel is such that it may intercept convective storm tops. Nonetheless, in accordance with previous studies [*Gong et al.*, 2012], it appears that the gravity waves are excited preferentially by the core and the outer bands clouds as seen in the simulation. Now, the AIRS weighting function resolves only waves with large vertical wavelengths, and the filtering we used is very restrictive and filters all the spatial scales smaller than $\sim$ 70 km. Hence, although the AIRS sounding instrument provides a complementary confirmation for the structure of the emitted waves, we did not attempt in the present case to use these observations for quantitative estimates of the waves.

5. Gravity Waves in the Three PreConcordiasi Flights

[52] The case study presented in the above section has provided an example of CGWs sampled by the balloons and has allowed to assess the realism of gravity waves in mesoscale simulations of a developing cyclone. The estimate of the contribution from tropical cyclones has shown that it
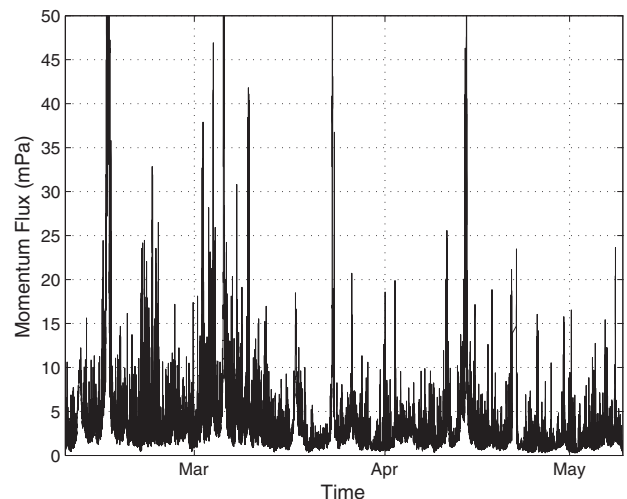
Figure 13. Momentum flux time series for the entire flight of the first PreConcordiasi balloon.

Table 6. Mean GW Momentum Flux, Momentum-Flux Weighted Averaged Phase Speeds, and Gini Coefficients for the Three PreConcordiasi Flights

Balloon #	1	2	3
IMF (mPa)	3.9	5.4	1.5
Flux standard deviation (mPa)	7.1	13.2	2.2
$\bar{c}$ (m s^{-1})	26.9	26.7	28
I_g	0.51	0.59	0.48

was necessary not to focus only on waves generated from these extreme but sparse events.

[53] In this section, making use of the whole flights of the three PreConcordiasi balloons, it is possible to analyze more generally the gravity wave field in the Tropics. We seek to characterize the CGWs and quantify their intermittency. Given the limited amount of data, we cannot derive a geographic distribution of the momentum fluxes and we restrict ourselves to the analysis of the time series.

5.1. Global Momentum Fluxes and Spectral Characteristics

[54] The momentum fluxes were analyzed from the balloon measurements using the same methodology as described in section 2.2. For illustration, we show in Figure 13 the time series of instantaneous momentum flux estimated for the entire flight of the first balloon. There are strong variations on fairly short timescales, yielding a noisy signal that is generally weaker than 10 mPa, but which contains short episodes with very intense values of several tens of mPa. As evidenced by these short and intense episodes, we observe strong GW activity in mid-February (Tropical Cyclone Gelane), throughout the month of March, and the first half of April. Table 6 summarizes different characteristics of the gravity waves observed during the flights. The comparison of the two balloons that remained in the Tropics (1 and 2, see Figure 1) shows comparable IMF values of about 4–5 mPa. The fact that both balloons yield comparable IMFs despite the differences in trajectories gives confidence that this value for the IMF is fairly robust, for the Tropics and for this time period. Yet, we find that the contribution of the waves with periods less than 20 min to the total momentum flux is about 40% to 50%. This suggests that those values are still sensitive to the sampling.

[55] We now review the spectral characteristics of the GWs observed by the balloons but for the entire flights. The distribution as a function of phase speed is represented in Figure 14. For Balloons 1 and 2 (black solid and dashed red), the spectra exhibit a single dominant mode with an amplitude approximately 10 times smaller than their respective counterpart in the Tropical Cyclone analysis. The momentum fluxes are integrated on a longer period of time; hence, the IMFs are reduced because the spectra results from intense CGW events such as associated with Tropical Cyclone Gelane, but also less intense convective events and weak GWs activity between two consecutive events. Although the maximum is attained for a phase speed close to zero, momentum fluxes decrease only slowly with increasing phase speed, yielding significant momentum fluxes carried by waves with phase speeds larger than 30, or even 50 m s^{-1} (about 20% of the momentum fluxes are carried by

waves with phase speeds larger than 50 m s^{-1}). Momentum flux weighted averaged phase speeds for the three balloons are found to be remarkably similar (about 27 m s^{-1}) as summarized in Table 6. The distribution for balloon #2 is slightly larger as that of balloon #1 for all phase speeds. This difference in amplitude can be explained by the fact that the second balloon observed more GW episodes as it stayed longer than balloon #1 in the Indian/West Pacific regions during intense multicellular convection. (For balloon #2, about 1 month from early April to early May 2010, versus no longer than ∼ 15 days for balloon #1.) The IMFs also reflect this difference with a value for balloon #2 that is 40% higher than that of balloon #1, and a standard deviation nearly twice as large (see Table 6). The main conclusion of the comparison between the two balloons should, however, be that these differences are fairly small, relative to our uncertainty on gravity wave momentum fluxes in this region, and that the shape of the distribution is robust and well-sampled. In other words, the sampling by the two balloons yields a robust shape for the momentum flux distribution (Figure 14) and a reasonable estimate of the amplitude (to within 40%).

[56] It is interesting to discuss the differences seen in balloon #3. As can be seen in Figure 1, balloon #3 drifted away from the tropics 1 month after its launch to fly poleward then in midlatitudes, in regions where deep convection occurs less frequently. The observed GW activity in the first 10 days of the flight (not shown) corresponds to periods when the balloon flew over Africa. Only one peak of significant activity is seen by the balloon once the African continent has been totally crossed. Therefore, the momentum flux distribution of balloon #3 can be interpreted as a midlatitude distribution. The IMF is 3 to 4 times weaker than that of the "Tropical" balloons. Note that it is consistent with values found from balloon measurements and mesoscale simulations at polar latitudes (0.9 mPa) [see *Plougonven et al.*, 2013, Table 2]. Interestingly, the shape of the distribution and the average phase speed are essentially the same as for the other two balloons, further suggesting the robustness of this distribution.
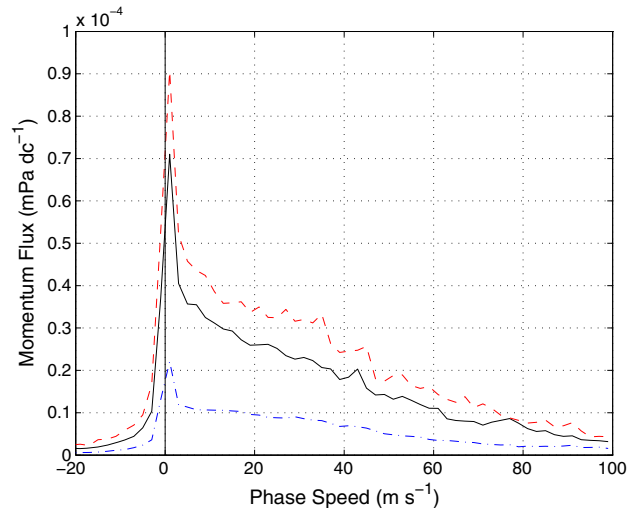
Figure 14. Same as Figure 5 for the entire flights of balloons 1 (solid black), 2 (dashed red), and 3 (strippled blue).
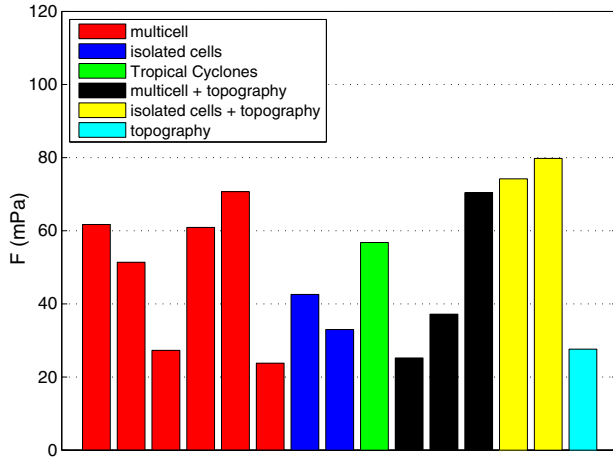
Figure 15. Convective and topographic sources of the mean GW momentum flux (greater than 20 mPa) for the three balloons. The number of bars denotes the number of a given type of event, and the height represents the mean flux during the event.

5.2. Gravity Wave Sources

[57] An important outcome of studies of gravity waves is to contribute to determine and quantify the different sources in the troposphere. At polar latitudes, *Hertzog et al.* [2008] and *Plougonven et al.* [2013] contrasted intense but very intermittent orographic sources with much weaker but more ubiquitous nonorographic sources (jets and fronts). In this section, we identify intense events (momentum fluxes larger than 20 mPa) and attempt to relate the GW to the convective or topographic environment near the balloon trajectories. We use satellite infrared radiances quick looks to determine if those episodes were associated to convection or orographic effects. When the balloons flew over or in the vicinity of convection, the event was denoted as convective, while it was marked as topographic when the balloon flew over mountains. Probable combinations of both effects were also identified. In order to get a comparison between those events in term of momentum fluxes, we have computed their associated mean flux. Those categories are summarized in Figure 15. The present observations do not suggest any conspicuous difference between the mean momentum fluxes carried by CGWs and topographic GWs. Convection appears to produce events that are as intense as orographic ones but are more frequent. We also note and emphasize that the tropical cyclone case does not stand out as a particularly intense event.

5.3. Intermittency

[58] We have seen previously that the CGW momentum fluxes vary significantly in time and space due to the sparse spatial distribution of the convective cells and the intermittency of the convective sources. As emphasized in previous studies [*Plougonven et al.*, 2008; *Hertzog et al.*, 2012], the intermittency can be quantified by momentum flux probability density functions (PDFs).

[59] Figure 16 displays the PDF of absolute momentum fluxes derived from the balloon observations. As underlined by *Hertzog et al.* [2012], PDFs exhibiting long tails account for the highly intermittent GWs in the lower stratosphere. Here they span for values up to 100 mPa for balloons #1 and #2 and 45 mPa for balloon 3. The PDFs are compared to the lognormal distribution having the same mean and standard deviation. *Hertzog et al.* [2012] have shown that over smooth terrain at high latitudes, the lognormal distribution provides a very good approximation of the PDF of momentum fluxes. We focus here on balloons #1 and #2. The lognormal distribution describes well the distribution of weak fluxes ($\lesssim$ 10 mPa) but overestimates the occurrence frequency for intermediate fluxes (10–50 mPa). At larger values ($>$ 50 mPa), the lognormal distribution underestimates the frequency of occurrence. This suggests that strong intermittency is associated with events of convective gravity waves: as for orographic gravity waves, it is likely that the PDF deviates from the lognormal distribution by a longer tail (intense events are less rare than expected for a lognormal distribution) [*Hertzog et al.*, 2012].

[60] The long tails of the PDFs are consistent with time series of momentum flux throughout the whole flight of balloon #1 for example (Figure 13) which revealed only a few temporally localized peaks. It may be noted that the PDFs for the two first balloons compare fairly well, especially for fluxes smaller than 25 mPa. The difference for greater momentum fluxes likely arises because the sampling is insufficient to observe many rare intense events. It is thus clear that the sampling of the tropical belt by two balloons is insufficient and that further observations would be needed for the PDFs to converge.

[61] Another way to quantify the global intermittency is to compute diagnostics. Recently, *Plougonven et al.* [2013] have suggested a diagnostic used in economics to quantify inequalities of income, the Gini coefficient [*Gini*, 1912], to measure the GW intermittency. For a series of values of absolute momentum fluxes f_n, it is given by:

$$I_g = \frac{\sum\limits_{n=1}^{N-1} \left(n\bar{f} - F_n \right)}{\sum\limits_{n=1}^{N-1} n\bar{f}}, \quad (17)$$
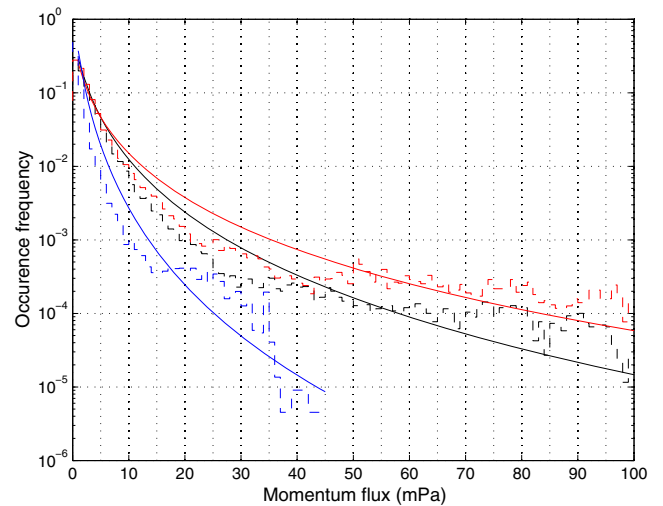
Figure 16. PDF of the momentum flux for balloons 1 (solid black), 2 (dashed red), and 3 (strippled blue).

where n represents the nth value (out of N values), $F_n = \sum_{i=1}^{n} f_i$ is the cumulative sum of the momentum fluxes f_i, and $\bar{f} = F_N/N$ is the averaged flux. A steady time series is the least intermittent series possible ($I_g = 0$) and a series with a single nonzero value is the most intermittent one ($I_g = 1$). *Plougonven et al.* [2013] argued that since this diagnostic involves summing of momentum fluxes, this method is robust to the sampling quality. We show the Gini coefficients computed for the three balloons in the last entry of Table 5. All three values are fairly close, with I_g for balloon #2 larger than the others, again reflecting the convective events from the Indian Ocean. The present results suggests that values between 0.5 and 0.6 should be expected for tropical regions, while values between 0.4 and 0.5 were typical of nonorographic regions at high latitudes and values up to 0.7 were found in regions of strong orographic gravity waves *Plougonven et al.* [2013].

6. Conclusion

[62] In situ measurements from superpressure balloons and high-resolution numerical simulations have been used to analyze gravity waves generated by convection in the Tropics. In the first part of this study, gravity waves generated by convective processes during the developing phase of the Tropical Cyclone Gelane have been analyzed and compared in balloon observations and in numerical simulations with the *Weather Research and Forecast* model. A reasonable agreement with previous numerical studies was found for the mean momentum fluxes (~ 90 mPa) and its distribution with phase speeds (main contributions associated with phase speeds in 10–40 m s^{-1}). Nevertheless, our simulations have emphasized that the major contribution to momentum fluxes was due to short horizontal wavelength (< 15 km) and short-period (< 20 min) waves.

[63] In contrast to previous studies, numerical results could here be compared to direct observations of GWs emitted by the storm. Mean momentum fluxes in the vicinity of the storm were found to be comparable and of the order of 100 mPa (for a domain of about 350 km by 350 km). The spectral analysis has shown that both observations and simulations emphasize GW with short wavelengths of 10 km or shorter. The observations suggest that it is necessary to further refine the resolution ($\Delta x = 1$ km was used in the innermost domain) in order to fully resolve the GW spectrum. Regarding phase speeds, both observations and simulations agree regarding the importance of phase speeds in the range 5–25 m s^{-1}. For larger phase speeds, larger fluxes are found in the simulations, but this could simply be due to the limited sampling of the wavefield by the balloon. A more significant disagreement is found regarding near-zero phase speeds: whereas these correspond to the largest momentum fluxes in the observations, they are nearly absent from the simulations. Analysis of the simulated wavefield at lower heights reveal that this part of the gravity wave spectrum was present a few kilometers below the flight level of the balloons but has been chopped off due to the variation of the background wind. In other words, the disagreement at near-zero phase speeds is likely due to biases in the simulation of the background wind. This illustrates how challenging it remains to precisely compare observations and mesoscale simulations

of convectively generated waves in the Tropics: the initial state and lateral boundary conditions come from analyses which are known to retain significant uncertainties, particularly at stratospheric heights and for the wind field. This contributes to making the realistic simulation of organized tropical convection a challenge, in addition to the intrinsic difficulties of simulating convection. In consequence, further case studies will be necessary to assess more precisely the realism of the simulated gravity wavefield.

[64] In the second part of this study, we have analyzed the entire time series for the three PreConcordiasi flights (February–May 2010). The two balloons that remained in the Tropics exhibit mean momentum fluxes of 3.9 and 5.4 mPa, suggesting that 5 mPa is a typical mean value for the Tropics during that time of year. However, these fluxes occur in very intermittent episodes. Fluxes were found to be concentrated during intense events with values of about 50 mPa over 1 day. Time series showed that peak values of several hundreds mPa could be reached on timescales of an hour or so. The intermittency of the gravity wavefield was quantified using PDFs and the Gini coefficient. Although sampling was insufficient to conclude, the PDFs suggest a deviation from the lognormal distribution (longer tail), as was found for regions of strong orographic GW activity [*Hertzog et al.*, 2012]. This may be partly summarized by a Gini coefficient between 0.5 and 0.6.

[65] The intense events were analyzed to identify likely sources: episodes tied to convection were found to be most frequent, but events tied to orography were also found. Both had comparable intensities. The cyclone that served as a case study did not stand out among convective events. This and an estimation based on the case study above suggests, as previous studies [*Kuester et al.*, 2008], that tropical cyclones do not have a particularly strong contribution to the overall momentum fluxes toward the Tropical stratosphere.

[66] Wavelet analysis was used to obtain the distribution of momentum fluxes as a function of phase speeds and horizontal wavelengths. Strikingly, the distribution as a function of phase speed exhibits a robust shape, with maximum fluxes for near-zero phase speeds and a slow decrease for larger phase speeds. The average phase speed was found consistently to be about 27 m s^{-1}. Besides, the contribution of waves with intrinsic periods shorter than 20 min was found to be about 40% to 50% of the total flux.

Appendix A: Effect of Depressurization Events on the Estimation of Gravity-Wave Momentum Fluxes

[67] The effect of balloon depressurization events on the momentum flux estimates can be assessed as follows. Consider a disturbance in air density (ρ') induced by a gravity wave packet, and let:

$$\zeta'_\rho = -\rho' \left(\frac{\partial \bar{\rho}}{\partial z} \right)^{-1} \tag{A1}$$

be the associated vertical displacement of the constant-density surface. When fully pressurized, ζ'_ρ corresponds to the balloon vertical displacement [*Boccara et al.*, 2008]. This is no longer the case when the balloon is not fully inflated, as its volume V_b is free to vary, and thus its density $\rho_b = M/V_b$ with M the total mass carried by the balloon too.

[68] Now, observations show that during depressurization events, the gas temperature, which primarily results from heat exchanges by conduction with the balloon envelop, stays nearly constant. As these events occur during overcast conditions, the balloon envelop integrates radiative fluxes that do not vary much, at least away enough from the start and end of these periods. At first order, the balloon density variations can therefore be related to the helium pressure variations (P_h) with the help of the perfect gas law:

$$\frac{\delta\rho_b}{\rho_b} = \frac{\delta P_h}{P_h}. \tag{A2}$$

But, when the balloon is depressurized, $P_h \sim P$, the atmospheric pressure. Hence, when the constant-density surface is displaced upward ($\rho' < 0$), the pressure in the balloon decreases, and so the balloon density. The depressurized balloon therefore tends to amplify its vertical displacement with respect to a fully pressurized (and thus constant-volume) balloon. Assuming that the background atmosphere is in hydrostatic equilibrium, one obtains

$$\frac{\delta\rho_b}{\rho_b} = -\frac{\bar{\rho}g}{\bar{P}}\zeta'_\rho$$
$$= -\frac{g}{R\bar{T}}\zeta'_\rho. \tag{A3}$$

The additional vertical balloon displacement (δz) due to this density change is therefore

$$\delta z = \left(\frac{\partial\bar{\rho}}{\partial z}\right)^{-1}\delta\rho_b$$
$$= \left(1 + \frac{R}{g}\frac{\partial T}{\partial z}\right)^{-1}\zeta'_\rho. \tag{A4}$$

Hence, in the tropical lower stratosphere where $\frac{\partial T}{\partial z} > 0$, $\delta z \lesssim \zeta'_\rho$: the momentum fluxes should be overestimated by at most a factor 2 during depressurization periods.

[69] During these events, the period of the balloon neutral oscillations may also become longer than the one mentioned in section 2.2 for a pressurized balloon, and potentially exceeds the Brunt-Väisälä period. The balloon oscillations may thus be confused with gravity wave disturbances. In particular, the balloon oscillations will also be associated with wind fluctuations in the presence of wind shear. Yet gravity wave momentum fluxes are estimated from the quadrature spectrum of wind and pressure disturbances [*Boccara et al.*, 2008], whereas the balloon oscillations will tend to produce in-phase perturbations. The balloon oscillations should therefore not significantly alter the momentum flux estimations, even when the balloon is not pressurized.

References

Alexander, M. J., and C. Barnett (2007), Using satellite observations to constrain parameterizations of gravity wave effects for global models, *J. Atmos. Sci.*, *64*, 1652–1665.

Alexander, M. J. A., et al. (2010), Recent developments in gravity-wave effects in climate models and the global distribution of gravity-wave momentum flux from observations and models, *Q. J. R. Meteorol. Soc.*, *136*, 1103–1124.

Aumann, H. H., et al. (2003), AIRS/AMSU/HSB on the aqua mission: Design, science objectives, data products, and processing systems, *IEEE Trans. Geosci. Remote Sens.*, *41*, 253–264.

Austin, J., et al. (2003), Uncertainties and assessment of chemistry-climate models of the stratosphere, *Atm. Chem. Phys.*, *3*, 1–27.

Barker, D. M., W. Huang, Y.-R. Guo, and Q. N. Xiao (2004), A three-dimensional (3DVAR) data assimilation system for use with MM5: Implementation and initial results, *Mon. Weather Rev.*, *132*, 897–914.

Beres, J. H., M. J. Alexander, and J. R. Holton (2002), Effects of tropospheric wind shear on the spectrum of convectively generated gravity waves, *J. Atmos. Sci.*, *59*, 1805–1824.

Boccara, G., A. Hertzog, R. A. Vincent, and F. Vial (2008), Estimation of gravity wave momentum flux and phase speeds from quasi-Lagrangian stratospheric balloon flights. Part I: Theory and simulations, *J. Atmos. Sci.*, *65*, 3042–3055.

Butchart, N., et al. (2010), Chemistry-climate model simulations of twenty-first century stratospheric climate and circulation changes, *J. Clim.*, *23*, 5349–5374.

Chen, F., and J. Dudhia (2001), Coupling an advanced land surface hydrology model with the Penn State-NCAR MM5 modeling system. Part I: Model implementation and sensitivity, *Mon. Weather Rev.*, *129*, 569–585.

Dewan, E., R. Picard, R. O'Neil, H. Gardiner, J. Gibson, J. Mill, E. Richards, M. Kendra, and W. Gallery (1998), MSX satellite observations of thunderstormgenerated gravity waves in midwave infrared images of the upper stratosphere, *Geophys. Res. Lett.*, *25*(7), 939–942, doi:10.1029/98GL00640.

Dhaka, S., M. Takahashi, Y. Shibagaki, M. Yamanaka, and S. Fukao (2003), Gravity wave generation in the lower stratosphere due to passage of the typhoon 9426 (Orchid) observed by the MU radar at Shigaraki (34.85N, 136.10E), *J. Geophys. Res.*, *108*(D19), 4595, doi:10.1029/2003JD003489.

Dudhia, J. (1989), Numerical study of convection observed during the winter monsoon experiment using a mesoscale two-dimensional model, *J. Atmos. Sci.*, *46*, 3077–3107.

Dunkerton, T. J. (1997), The role of gravity waves in the quasi-biennial oscillation, *J. Geophys. Res.*, *102*, 26,053–26,076.

Ern, M., P. Preusse, J. C. Gille, C. L. Hepplewhite, M. G. Mlynczak, J. M. Russell III, and M. Riese (2011), Implications for atmospheric dynamics derived from global observations of gravity wave momentum flux in stratosphere and mesosphere, *J. Geophys. Res.*, *116*, D19107, doi:10.1029/2011JD015821.

Evan, S., M. J. Alexander, and J. Dudhia (2012), WRF simulations of convectively generated gravity waves in opposite QBO phases, *J. Geophys. Res.*, *117*, D12117, doi:10.1029/2011JD017302.

Fetzer, E., et al. (2003), AIRS/AMSU/HSB validation, *IEEE Trans. Geosci. Remote Sens.*, *41*, 418–431.

Fritts, D. C., and M. J. Alexander (2003), Gravity wave dynamics and effects in the middle atmosphere, *Rev. Geophys.*, *41*(1), 1003, doi:10.1029/2001RG000106.

Gentry, M. S., and G. M. Lackman (2006), The sensitivity of WRF simulations of Hurricane Ivan to the choice of cumulus parameterization, paper presented at 27th Conf. on Hurricanes and Trop. Meteor. Amer. Meteor. Soc., Monterey, CA.

Gini, C. (1912), *Variabilità e mutabilità (Variability and Mutability)*, 156 pp., Libreria Eredi Virgilio Veschi (1955), Bologna.

Gong, J., D. L. Wu, and S. D. Eckermann (2012), Gravity wave variances and propagation derived from AIRS radiances, *Atmos. Chem. Phys.*, *12*, 1701–1720.

Hertzog, A., and F. Vial (2001), A study of the dynamics of the equatorial lower stratosphere by use of ultra-long-duration balloons, 2. Gravity waves, *J. Geophys. Res.*, *106*, 22,745–22,761.

Hertzog, A., et al. (2007), Stratéole/Vorcore - Long duration, superpressure balloons to study the Antarctic stratosphere during the 2005 winter, *J. Ocean. Atmos. Tech.*, *24*, 2048–2061.

Hertzog, A., G. Boccara, R. Vincent, F. Vial, and P. Cocquerez (2008), Estimation of gravity-wave momentum fluxes and phase speeds from long-duration stratospheric balloon flights. Part II. Results from the Vorcore campaign in Antarctica, *J. Atmos. Sci.*, *65*, 3056–3070.

Hertzog, A., M. J. Alexander, and R. Plougonven (2012), On the intermittency of gravity-wave momentum flux in the stratosphere, *J. Atmos. Sci.*, *69*, 3433–3448.

Holton, J. R., P. H. Haynes, M. E. McIntyre, A. R. Douglass, R. B. Rood, and L. Pfister (1995), Stratosphere-troposphere exchange, *Rev. Geophys.*, *33*, 405–439.

Hong, S.-Y., and H.-L. Pan (1996), Nonlocal boundary layer vertical diffusion in a medium-range forecast model, *Mon. Weather Rev.*, *124*, 2322–2339.

Kain, J. S. (2004), The Kain-Fritsch convective parameterization: An update, *J. Appl. Meteorol.*, *41*, 65–98.

Kawatani, Y., S. Watanabe, K. Sato, T. J. Dunkerton, S. Miyahara, and M. Takahashi (2010), The roles of equatorial trapped waves and internal inertia-gravity waves in driving the Quasi-Biennial Oscillation. Part I: Zonal mean wave forcing, *J. Atmos. Sci.*, *67*, 963–980.

Kim, S.-Y., H.-Y. Chun, and J.-J. Baik (2005), A numerical study of gravity waves induced by convection associated with Typhoon Rusa, *Geophys. Res. Lett.*, *32*, L24816, doi:10.1029/2005GL024662.

Kim, S.-Y., H.-Y. Chun, and J.-J. Baik (2007), Sensitivity of typhoon-induced gravity waves to cumulus parameterizations, *Geophys. Res. Lett.*, *34*, L15814, doi:10.1029/2007GL030592.

Kim, Y.-J., and H.-Y. Chun (2010), Stratospheric gravity waves generated by Typhoon Saomai (2006): Numerical modeling in a moving frame following the Typhoon, *J. Atmos. Sci.*, *67*, 3617–3636.

Kim, Y.-J., S. D. Eckermann, and H.-Y. Chun (2003), An overview of the past, present and future of gravity-wave drag parametrization for numerical climate and weather prediction models, *J. Appl. Meteorol.*, *41*, 65–98.

Kuester, M. A., M. J. Alexander, and E. A. Ray (2008), A model study of gravity waves over Hurricane Humberto (2001), *J. Atmos. Sci.*, *65*, 3231–3246.

Lane, T. P., and J. C. Knievel (2005), Some effects of model resolution on simulated gravity waves generated by deep, mesoscale convection, *J. Atmos. Sci.*, *62*, 3408–3419.

Mlawer, E. J., S. J. Taubman, P. D. Brown, M. J. Iacono, and S. A. Clough (1997), Radiative transfer for inhomogeneous atmospheres: RRTM, a validated correlated-k model for the longwave, *J. Geophys. Res.*, *102*, 16,663–16,682.

Morrison, H., G. Thompson, and V. Tatarskii (2009), Impact of cloud microphysics on the development of trailing stratiform precipitation in a simulated squall line: Comparison of one- and two-moment schemes, *Mon. Weather Rev.*, *137*, 991–1007.

Nastrom, G. D. (1980), The response of superpressure balloons to gravity waves, *J. Appl. Meteorol.*, *19*, 1013–1019.

Pawson, S., et al. (2000), The GCM-Reality Intercomparison Project for SPARC (GRIPS): Scientific issues and initial results, *Bull. Am. Meteorol. Soc.*, *81*, 781–796.

Pfister, L. W. P. L., S. Scott, M. Loewenstein, S. Bowen, and M. Legg (1993), Mesoscale disturbances in the tropical stratosphere excited by convection: Observations and effects on the stratospheric momentum budget, *J. Atmos. Sci.*, *50*(D5), 1058–1075.

Plougonven, R., A. Hertzog, and H. Teitelbaum (2008), Observations and simulations of a large-amplitude mountain wave breaking above the Antarctic Peninsula, *J. Geophys. Res.*, *113*, D16113, doi:10.1029/2007JD009739.

Plougonven, R., A. Hertzog, and L. Guez (2013), Gravity waves over Antarctica and the Southern Ocean: Consistent momentum fluxes in mesoscale simulations and stratospheric balloon observations, *Q. J. R. Meteorol. Soc.*, *139*, 101–118, doi:10.1002/qj.1965.

Plu, M. (2011), A new assessment of the predictability of tropical cyclone tracks, *Mon. Weather Rev.*, *11*, 3600–3608.

Rabier, F., et al. (2010), The Concordiasi project in Antarctica, *Bull. Am. Meteorol. Soc.*, *91*(1), 69–86.

Sato, K. (1993), Small-scale wind disturbances observed by the MU radar during the passage of Typhoon Kelly, *J. Atmos. Sci.*, *50*, 518–537.

Scaife, A. A., N. Butchart, C. D. Warner, D. Stainforth, W. Norton, and J. Austin (2000), Realistic quasi-biennal oscillations in a simulation of the global climate, *Geophys. Res. Lett.*, *27*, 3481–3484.

Singh, R., P. K. Pal, C. M. Kishtawal, and P. C. Joshi (2005), Impact of bogus vortex for track and intensity prediction of Tropical Cyclone, *J. Earth Syst. Sci.*, *114*, 427–436.

Skamarock, W. C., J. B. Klemp, J. Dudhia, D. O. Gill, D. M. Barker, W. Wang, and J. G. Powers (2005), A description of the Advanced Research WRF Version 2, *Tech. Note NCAR/TN-468+STR*, Natl. Cent. for Atmos. Res., Boulder, Colo.

Skamarock, W. C., J. B. Klemp, J. Dudhia, D. O. Gill, D. M. Barker, M. G. Duda, X.-Y. Huang, W. Wang, and J. G. Powers (2008), A description of the Advanced Research WRF Version 3, *Tech. Rep.*, Natl. Cent. for Atmos. Res., Boulder, Colo.

Vincent, R. A., A. Hertzog, G. Boccara, and F. Vial (2007), Quasi-Lagrangian superpressure balloon measurements of gravity-wave momentum fluxes in the polar stratosphere of both hemispheres, *Geophys. Res. Lett.*, *34*, L19804, doi:10.1029/2007GL031072.

Wang, L. M., M. J. Alexander, P. T. Bui, and M. J. Mahoney (2006), Small-scale gravity waves in ER-2 MMS/MTP wind and temperature measurements during CRYSTAL-FACE, *Atmos. Chem. Phys.*, *6*, 1091–1104.

Webster, P. J., G. J. Holland, J. A. Curry, and H.-R. Chang (2005), Changes in tropical cyclone number, duration, and intensity in a warming environment, *Science*, *309*, 1844–1846.

Wicker, L. J., and W. C. Skamarock (2002), Time splitting methods for elastic models using forward time schemes, *Mon. Weather Rev.*, *130*, 2088–2097.

2.5   Perspectives

Une des principales limitations qui ressort de notre étude en utilisant les données PreConcordiasi est le nombre restreint de ballons, qui ne permet pas d'obtenir de climatologies moyennes. Dans le cadre de Stratéole 2 qui débutera en 2018 et dans la continuité de PreConcordiasi, une vingtaine de ballons pressurisés (augmentation de près d'un facteur 10 par rapport à PreConcordiasi) longue durée seront lâchés aux tropiques, et qui permettront de documenter les ondes de gravité dans les régions tropicales. Etant donnée la densité plus grande d'observations par rapport à PreConcordiasi, on attend avec Stratéole 2 une meilleure caractérisation des flux de quantité de mouvement, des vitesses de phase, et de l'intermittence que précédemment.

Les autres informations que nous pouvons obtenir à partir des observations Pre-Concordiasi mais que nous n'avons pas analysées sont 1) la direction de propagation des ondes de gravité, et 2) la distinction entre convection profonde et superficielle dans les spectres de vitesses de phase qui intéressent particulièrement les modélisateurs qui écrivent les paramétrisations (Alexander, Bacmeister, Richter (2013), personal communication).

CHAPTER III

Les ondes de gravité aux hautes latitudes

3.1 Les ondes de gravité non-orographiques

Les ondes de gravité aux hautes latitudes participent au forçage de la circulation en moyenne atmosphère, en particulier pour la fermeture des jets en mésosphère et l'écoulement stratosphérique (*Andrews et al.*, 1987). D'autre part, certaines études récentes (*McLandress et al.*, 2012) attribuent les biais systématiques des modèles sur le moment de la destruction du vortex stratosphérique de l'hémisphère sud au printemps (*Eyring et al.*, 2010; *Geller et al.*, 2013) aux ondes de gravité. On note dans les modèles un déficit de traînée d'ondes de gravité sur une bande de latitude qui correspond à 60°S, qui n'est pas observé dans les mesures satellites. La question de la partie résolue ou paramétrée de ces ondes n'est pas encore tranchée, toutefois le manque de traînée d'ondes de gravité dans cette région au printemps en stratosphère de l'Hémisphère sud fait l'objet d'un consensus. *McLandress et al.* (2012) attribuent ce manque à un déficit d'ondes orographiques généré par les îles isolées situées à 60°S (*Alexander et al.*, 2009). Une autre raison potentielle donnée par *McLandress et al.* (2012) et observée dans des simulations à haute résolution par *Sato et al.* (2009) est la propagation méridionale d'ondes de montagne vers le cœur du jet stratosphérique qui se situe à 60°S, non représentée par les paramétrisations actuelles qui font l'hypothèse d'une propagation purement verticale. Toutefois, *McLandress et al.* (2012) n'excluent

pas la possibilité d'ondes non-orographiques mal représentées dans les modèles, même s'ils écartent cette possibilité avec des arguments peu convaincants.

Les ondes de gravité orographiques et leurs effets ont été beaucoup étudiés car leurs sources sont relativement simples à caractériser. Il n'en est pas de même pour les ondes non-orographiques pour lesquelles les sources sont mobiles et plus difficiles à étudier (*Plougonven and Zhang*, 2014). Il y a eu des études sur les mécanismes d'excitation des ondes par les dipôles, jets ou fronts (*Plougonven and Snyder*, 2006; *Snyder et al.*, 2007; *Wang et al.*, 2008; *Snyder et al.*, 2009), et par les anomalies de vorticité potentielle (PV) (*Lott et al.*, 2010, 2012). Cependant, peu d'études ont proposé des climatologies pour les ondes de gravité non-orographique en basse stratosphère avec des observations in-situ qui permettent de récupèrer l'ensemble de leurs caractéristiques (*Hertzog et al.*, 2008).

Une meilleure connaissance des ondes de gravité dans la stratosphère de l'hémisphère sud, le besoin d'obtenir leur climatologie et leurs caractéristiques (leur intermittence), et comprendre les sources d'incertitudes dans les modèles constituent les motivations de notre étude. En outre, l'amélioration des paramétrisations (*Orr et al.*, 2010) et des systèmes d'assimilation de données, ainsi que l'augmentation progressive de la résolution (horizontale et verticale) des modèles pose désormais la question du réalisme des champs d'ondes dans leurs analyses, ce que nous proposons de faire ici.

3.2   Données disponibles

Les observations utilisées dans cette étude sont des mesures par SPB provenant de la campagne Concordiasi (*Rabier et al.*, 2010). 18 ballons ont été lancés entre août et septembre 2010 depuis la station de McMurdo (78°S, 166°E) en Antarctique par le CNES. Ces ballons ont les mêmes caractéristiques que les SPB de la campagne PreConcordiasi décrits en section 2.2, et sont par conséquent bien adaptés à l'étude des ondes de gravité. Les ballons ont volé en basse stratosphère à 19-20 km d'altitude

pendant des périodes typiques de 3 mois.

Le champs d'ondes de gravité est aussi analysé dans les analyses opérationnelles de l'ECMWF. Avec l'augmentation de la résolution horizontale (0.125°) et verticale (encore 91 niveaux au moment de l'étude, 137 désormais) pour les ondes résolues, et l'amélioration des paramétrisations d'ondes de gravité, il est nécessaire d'examiner leur réalisme dans les analyses. Les analyses sont produites tous les jours à 0000, 0006, 1200, et 1800UTC par le système 4D-Var opérationnel de l'ECMWF (*Rabier et al.*, 2000; *Mahfouf and Rabier*, 2000; *Klinker et al.*, 2000) et constituent les conditions initiales pour les prévisions déterministes sur 10 jours.

3.3   Principaux résultats

Les résultats principaux de cette étude sont, en mettant l'accent sur les flux de quantité de mouvement des ondes de gravité:

1. Les flux moyens à partir des analyses ECMWF sont sous-estimés par rapport à ceux dans Concordiasi d'un facteur 5. Les valeurs moyennes sont de 1.8 mPa dans l'ECMWF et 9 mPa dans Concordiasi si on considère un échantillonnage identique des événements d'ondes de gravité. Cependant, on note un contraste plus fort dans l'ECMWF que dans les observations Concordiasi entre la région du plateau Antarctique et les régions montagneuses et océaniques (approximativement d'un facteur 2). Le facteur 5 reste valide au-dessus des océans mais surestime légèrement les flux au dessus des régions orographiques. Cette différence provient a priori de la résolution horizontale principalement. De plus, il est difficile de discerner les structures au dessus des océans en raison d'un nombre insuffisant d'observations.

2. Il y a un bon accord géographique et saisonnier entre Concordiasi et l'ECMWF. On retrouve les régions privilégiées dans l'ECMWF et Concordiasi (Péninsule,

sud des Andes, montagnes transantarctiques, îles dans l'océan, Tasmanie, Nouvelle Zélande). L'accord saisonnier s'observe aussi bien dans les cartes des flux que dans l'évolution des PDF. L'activité des GW est plus élevée pour les mois de printemps en raison de vents plus intenses. En décembre et janvier, l'activité est à son minimum en raison de la disparition du jet stratosphérique vers la fin du printemps. Les PDF des flux de quantité de mouvement montrent la même variabilité saisonnière avec une diminution de la valeur moyenne des flux entre novembre et décembre, qui s'accompagne d'une baisse de l'intermittence, en particulier pour les OGW. L'intermittence est plus élevée pour les OGW que les NGW, ce qui se traduit par des PDF avec des queues de distribution plus longues pour les OGW.

3. En utilisant les observations de Concordiasi, nous avons montré que la traînée d'ondes de gravité à 60°S présent dans les modèles provient principalement de NGW au dessus de l'océan. La contribution des NGW est de même ordre de grandeur en amplitude que celle des ondes excitées par la Péninsule, et domine largement celle des OGWs générées par les îles.

La suite est basée sur un article en préparation en anglais.

3.4 "Gravity waves in the Southern Hemisphere derived from balloon observations and the ECMWF analyses"

Gravity waves in the Southern Hemisphere derived from balloon observations and the ECMWF analyses.

Valérian Jewtoukoff, Albert Hertzog, and Riwal Plougonven.
Laboratoire de Météorologie Dynamique du CNRS, Ecole
Polytechnique, 91128 Palaiseau Cedex, France.

Abstract

Stratospheric balloons from the Concordiasi campaign constitute a unique dataset that provides a description of the gravity wave field and their entire characteristics in the lower stratosphere in the Southern Hemisphere including the Antarctica and the Southern Ocean in spring to summer 2010. On the other hand, the advances in numerical computation, data assimilation, and increase of horizontal and vertical resolutions pose the question of the realism of the simulated gravity wave field in the ECMWF analyses. First, we compare the observations from Concordiasi to the ECMWF fields throughout the whole campaign with an emphasis on gravity wave momentum fluxes and intermittency. Correct agreements are found for the geographical distributions and hotspots (southern tip of the Andes, Antarctic Peninsula, Transantarctic Mountains, islands) with typical mean values of 100 mPa over mountains, $\lesssim$10 mPa over islands and oceans. However, discrepancies arise on the magnitude with an underestimation of the fluxes in the ECMWF by a factor 5, owing to resolution and limitations in the representation of the gravity waves. A larger contrast (by a factor 2) is observed in the ECMWF relative to Concordiasi between the regions with low values (Antarctic Plateau) and higher values (Mountains, and over the ocean). The intermittency of the momentum fluxes is higher for orographic waves than nonorographic (Gini coefficients of 0.9 and 0.7 respectively). Monthly means show comparable seasonal variations in Concordiasi and ECMWF with a higher gravity wave activity in September-October

and a progressive decrease of 90% (30%) of the initial flux throughout spring over mountains (ocean), correlated with the weakening of the stratospheric jet. PDFs reflect this seasonal shift with a decrease of the mean flux, associated with a loss of intermittency (the tail of higher values vanishes). In December, PDFs over mountains and oceans are absolutely similar. Despite the good agreement on the time evolution of the PDF, it is shown that the contrast between orographic and nonorographic waves in the ECMWF is significantly smaller than in the observations. In the second part, we compare the momentum fluxes for two individual orographic and nonorographic events. The same conclusions as the global analysis arise: reasonable agreeement between Concordiasi and ECMWF on the spatial structure, in spite of an underestimation of the fluxes by 5 in ECMWF. The results suggest that the resolved gravity wave field in the ECMWF analyses can be used to study the geographical distribution, seasonal and interannual variations of momentum fluxes. Finally, we conclude on the sources of the missing gravity wave drag at 60°S in global models acknowledgely responsible of biases in the Southern Hemisphere spring circulation using the Concordiasi datasets. We find that the contribution from nonorographic effects significantly dominates orographic effects associated with the islands located at 60°S, suggesting a bias in the parameterized nonorographic gravity waves.

3.5   Introduction

Gravity waves (GWs) play a crucial role in the middle atmosphere. When they propagate vertically away from their tropospheric sources (i.e. topography, convection, fronts, unbalanced jets), they deposit their momentum fluxes to the mean flow in the middle atmosphere when they dissipate because of critical levels or density effects. In particular, the deposition of GW momentum flux closes the jet in the mesosphere (*Andrews et al.*, 1987). GWs also force the stratospheric circulation, like the Quasi-Biennal Oscillation in the Tropics (*Baldwin et al.*, 2001). Their intrinsic frequency

range being bounded by the planetary vorticity f and the buoyancy frequency N, they usually occur on relatively small scales of few to hundreds of kilometers (*Fritts and Alexander*, 2003). Therefore, since they have scales smaller than the typical resolvable scales by the models (500-1000 km) their effects need to be represented by parameterizations.

We distinguish two types of GWs: the orographic gravity waves (OGWs) which are excited by the topography, and nonorographic gravity waves (NGWs) emitted by frontal systems and unbalanced jets (*Plougonven and Zhang*, 2014). NGWs and OGWs show different physical properties (quasi-stationary versus non-stationary). Unlike the OGWs for which the sources are known, NGWs lack observational constraints and their sources are consequently represented arbitrarily and tuned in the NGW parameterizations. The discrepancies in these parameterizations are responsible for the uncertainties in the simulation of the middle atmosphere, therefore one of the main motivation for studying the GW is to provide constraints for their parameterizations (*Alexander et al.*, 2010).

Improving the current parameterizations necessitates to obtain the GW characteristics from observations and simulations (*Alexander et al.*, 2010). Superpressure balloons (SPBs) constitute unique datasets well adapted to study GWs because they provide in-situ observations in the framework moving with the mean flow. Thus, it is possible to observe directly the entire characteristics of the GW field, in particular their intrinsic frequencies. During the Concordiasi campaign (*Rabier et al.*, 2010), 18 SPBs were launched during the austral spring to summer 2010-2011 from the McMurdo station in Antarctica. Each balloon flew in the lower stratosphere at 19-20 km of altitude for durations of 3 months typically, performing measurements of position, altitude, pressure and temperature with a frequency of $1/(30 \text{ s})$. In contrast with the previous Vorcore campaign (*Hertzog et al.*, 2007), the increase of time resolution allows to observe the entire GW spectrum, providing an unprecedented dataset for

their study in the austral lower stratosphere, and complementing the climatology derived by *Hertzog et al.* (2008).

Following the progressive convergence of the ECMWF GW field due to the recent increase in spatial resolution (0.125° horizontally and 91 vertical levels), and improvements of parameterizations (*Orr et al.*, 2010), dynamical core, and data assimilation systems, studies are beginning to examine the realism of the GW in their analyses by comparison to observations (*Eckermann et al.*, 2006; *Alexander and Teitelbaum*, 2007; *Wu and Eckermann*, 2008; *Ern et al.*, 2008; *Schroeder et al.*, 2009). *Plougonven and Teitelbaum* (2003) compared the characteristics of inertia gravity waves (IGWs) derived from radiosoundings from the FASTEX campaign and the ECMWF analyses. Their results suggested that the ECMWF analyses can be used for qualitative indications on the location and time of generation of large-scale IGWs. *Alexander and Teitelbaum* (2007) analyzed a case study of large amplitude mountain wave event that occured over the Antarctic Peninsula on 10 September 2003 using measurements from the Atmospheric Infrared Sounder (AIRS) on the AQUA satellite and the European Centre for Medium Range Forecasts (ECMWF) forecasts and analyses. They found a similar properties between AIRS and the ECMWF in general with correct agreement on horizontal and vertical wavelengths, propagation direction, wave amplitude, and approximate timing of the event. Moreover, they did not remark significant differences between the fields in the ECMWF forecasts and analyses. *Wu and Eckermann* (2008) compared the GW variances obtained from the Microwave Limb Sounder (MLS) on the Aura satellite to the waves in the ECMWF model. They observed similar enhanced GW variances over regions with large background wind speeds, and over regions with topographic and convective forcing. *Ern et al.* (2008) and *Schroeder et al.* (2009) have compared temperature variances attributed to GW in the infrared limb sounder SABER (Sounding of the Atmosphere Using Broadband Emission Radiometry) and the ECMWF analyses. The minimum

resolvable horizontal and vertical wavelengths for SABER are ∼400 km and ∼4.5 km respectively (*Geller et al.*, 2013), therefore resolving a smaller portion of GW than the ECMWF. They found a good agreement for OGWs (emitted by the Southern tip of the Andes and Scandinavia), and for NGWs near the edge of the winter polar vortex. However, they noted significant low biases on the amplitude of the waves by a factor 2-3. *Shutts and Vosper* (2011) compared estimates from to HIgh Resolution Dynamics Limb Sounder measurements with those derived from the ECMWF and concluded that ECMWF is capable of capturing the overall strength and distribution of GW activity. More recently, *Preusse et al.* (2014) have analysed the sources of GWs using backward ray-tracing, assuming the validity of the simulated fields a priori. Those studies suggest a potential for various observations to investigate the realism of the ECMWF GW field and validate the model. Such validations for the GWs are relevant as the community using the ECMWF data is increasing. Moreover, differences between observations and analyses provide a better understanding of the systematic biases in simulated stratospheres, such as the delayed springtime breakdown of the Southern Hemisphere stratospheric polar vortex. *McLandress et al.* (2012) attribute the discrepancies of the model to missing gravity wave drag (GWD) at 60°S owing to misrepresented effects in OGWD parameterizations. They argue that one of the reason may be OGWD from small localized islands located near the 60°S latitude band (*Alexander et al.*, 2009). Another potential reason is the meridional propagation of mountain waves into the stratospheric jet core located at 60°S (*Sato et al.*, 2009), yet *McLandress et al.* (2012) do not fully discard NGWD effects in their study.

Hence, our goal in the present study is 1) to compare the GW in the ECMWF to in-situ observations from SPBs during the Concordiasi campaign (*Rabier et al.*, 2010) to estimate the realism of the wave field in the ECMWF, and 2) use those datasets to provide a climatology of the momentum fluxes over the austral regions including Antarctica and the oceans, quantify the seasonal variations, distinguish the OGWs

from the NGWs, and quantify their intermittency. Finally, we use the Concordiasi observations to provide elements to reinvestigate *McLandress et al.* (2012)'s conclusions on the source of the missing GWD to interpret the systematic biases in the Southern Hemisphere stratosphere in models.

The paper is organized as follow: in Section 3.6, we describe the Concordiasi and ECMWF datasets and the methodology to calculate the momentum fluxes. In Section 3.7, we describe the global comparison between ECMWF and Concordiasi and identify the hotspots of GW, then we investigate the seasonal and regional variability. We present a comparison on two case studies of OGWs and NGWs and provide a validation of the model for those events. Section 3.9 provides our conclusions and a discussion of our results.

3.6 Data and Methodology

3.6.1 Stratospheric superpressure balloons from the Concordiasi Campaign

During the Concordiasi field campaign (*Rabier et al.*, 2010), 18 long-duration stratospheric superpressure balloons (SPBs) were launched from August to September 2010 from the McMurdo station (78°S, 166°E) in Antarctica by the Centre National d'Etudes Spatiales (CNES; the French space agency). Those balloon were designed to drift on isopycnic surface and they aimed at studying the circulation and chemical species in the lower stratosphere. In particular, measurements of pressure and temperature were retrieved by the Thermodynamic SENsor (TSEN) meteorological package aboard the balloons, while the wind was calculated using the successive positions of the balloon throughout the flight measured by GPS. Each balloon flew for a typical period of 3 months in the lower stratosphere at typical altitudes of 19-20 km (50-70 hPa). As for the studies on Vorcore (*Plougonven et al.*, 2013), the density of

measurements is high enough to sample numerous GW events and derive climatologies for the southern austral regions. The SPBs' measurements constitute a unique and well adapted dataset to study the GWs, and retrieve all their characteristics in the referential moving with the mean flow, at high frequency (the sampling period is 10 s) and for wide temporal and spatial coverage.

3.6.2 ECMWF operational analyses

We use the ECMWF analyses available four times a day (000, 0006, 1200, and 1800 UTC) that result from the 4D-Var data assimilation operational system (*Rabier et al.*, 2000; *Mahfouf and Rabier*, 2000; *Klinker et al.*, 2000) and provide the initial atmospheric conditions for the 10-days lead time deterministic operational forecasts. The model has a T1279 spectral truncation that corresponds a horizontal resolution of $0.125° \times 0.125°$ of longitude and latitude, that is, approximately a grid spacing of 10-12 km, and 91 vertical model levels (137 as of 2013) with an increased resolution near the surface. The GWs in the ECMWF are divided in a parameterized part and explicit part. Here, the resolution used adds a constraint on the minimum resolvable GW scales (approximately 72 km horizontally).

3.6.3 Calculation of momentum fluxes

The methodology described in *Boccara et al.* (2008) and updated to the increased sampling in time and in the resolution of measurements (*Vincent and Hertzog*, 2014) was applied to the balloon observations of pressure, zonal and meridional velocities to estimate the vertical total momentum fluxes. A wavelet analysis is applied to select the disturbances solely induced by GWs, and the momentum fluxes are obtained by calculation of the cospectra. In contrast with previous studies using the Vorcore dataset (*Plougonven et al.*, 2013), the increased sampling (1 obs/30 s) allows us to apply our analysis to the entire GW spectrum.

For the calculation using the ECMWF analyses, the velocity perturbations are obtained by removing the atmospheric base state defined by the 15 first zonal modes from the total velocity fields using spectral truncation. The density and the correlation between horizontal and vertical components are then calculated to yield the vertical total momentum fluxes. Since the calculation of the fluxes in the ECMWF involve the velocity perturbations, those fluxes correspond to the GWs resolved in the model. Examining the partitioning between resolved and parameterized GWs is beyond the scope of our study.

3.7 Overall comparison between the ECMWF analyses and the Concordiasi dataset

Our goal in this section is to compare the GW field in the ECWMF and in the Concordiasi balloon observations. We chose to compare quantities relevant for modelling and parameterizations, that is momentum fluxes and intermittency (*Alexander et al.*, 2010; *Hertzog et al.*, 2012). Numerous parameterizations take spatial and time variations of the GW field into account, thus it is necessary to derive climatologies using model outputs and observations. First, we aim to verify whether the GW momentum fluxes and spatial repartition agree overall. Second, we examine the intermittency of the momentum fluxes, and their seasonal evolution from September 2010 to January 2011.

3.7.1 Comparison of momentum fluxes

The GW momentum fluxes derived from the balloon observations and in the ECMWF analyses at 70 hPa, averaged on the period September 2010 - January 2011, are shown in Figure 3.1. The figure has been split into four panels representing a) the ECMWF momentum fluxes with native resolution (0.125°), b) the ECMWF fluxes

upscaled to an horizontal resolution of 2.5°, c) the ECMWF fluxes taking into account the balloon sampling (those fluxes have been multiplied by 5), and d) the fluxes from the Concordiasi balloons. We have chosen a logarithmic color scale to handle the large variety of momentum flux amplitudes that arise in the datasets. For example, the mean value of the flux in Concordiasi (ECMWF with the balloon sampling) is 9 mPa (1.8 mPa) with local mean values as high as 160 mPa (155 mPa). Note that we have also multiplied the momentum fluxes in Fig. 3.1c) by 5 to take into account the ratio of the mean Concordiasi value to the mean ECMWF flux in our spatial comparison. The remarkable features for the GW momentum fluxes are the following:

1. The hotspots of gravity waves are clearly revealed in the ECMWF analyses with full resolution (Fig.3.1a)): topography (Andes, Antarctic peninsula, Transantartic Mountains, small islands in the Austral ocean, New Zealand, Tasmania) with typical values of ∼100 mPa, coasts and islands with values ∼10 mPa and over oceans (denoting fronts and jets) with typical values slightly below 10 mPa.

2. The order of magnitude for the momentum fluxes are the same in Concordiasi and all the ECMWF panels, although ECMWF underestimates them on average by a factor 5. The mean value in Concordiasi is 9 mPa as mentioned above. This underestimation in the ECMWF is likely related to horizontal resolution and numerical (implicit or explicit) diffusion. It is interesting to note that upscaling the resolution, and sampling the events taking account of the position of the balloons does not change significantly the mean values (a) 2.1 mPa , b) 2.1 mPa, c) 1.8 mPa respectively).

3. We remark a correct agreement overall on the spatial structure of the GW momentum fluxes for high and low values, even if the contrast between the Antarctic plateau and the rest (mountains, and ocean) is stronger in the ECMWF than in Concordiasi (even considering the factor 5). To illustrate that contrast, the

relative difference between the mean fluxes for regions located South of and North of 80°S calculated in the ECMWF yields a value of 89% whereas it is 43% in the observations. Thus, the difference is of a factor 2. The only major discrepancies are Transantarctic Mountains that do no show up in the ECMWF after applying the Concordiasi sampling. The factor 5 is valid over the oceanic regions, but leads to an overestimation of the fluxes in the ECMWF over the mountains (Andes and Antarctic peninsula). In contrast with the ECMWF fluxes at full-resolution, the structures over the oceans (high activity from the Lazarev Sea to the Somov Sea located in the latitude band 60-45°S, and weaker activity in the Amundsen Sea and Weddell Seas) are difficult to identify with the balloon sampling in ECMWF and in the balloon measurements. This reveals that we do not have enough measurements for those regions.

3.7.2 Intermittency

We have seen in the previous section, that mean GW momentum fluxes vary significantly spatially. Their amplitudes also fluctuate rapidly in time about their mean values, revealing their intermittent behavior. Quantifying this intermittency is necessary to give a realistic picture of the GWs in model parameterizations. A good tool to examine the intermittency is to use momentum flux probability density functions (PDFs) as in previous studies (*Plougonven et al.*, 2013; *Hertzog et al.*, 2012; *Jewtoukoff et al.*, 2013). In this section, ECMWF PDFs are calculated on the native ECMWF high-resolution grid.

Figure 3.2b) shows the PDF of absolute momentum fluxes calculated in the ECMWF (thick lines) and derived from the Concordiasi observations (thin lines) for the Peninsula and the oceanic regions depicted in Figure 3.2a). The momentum fluxes from the ECMWF have been rescaled by a factor 5 so that they have the same mean as the balloon measurements. The Peninsula is representative of the regions
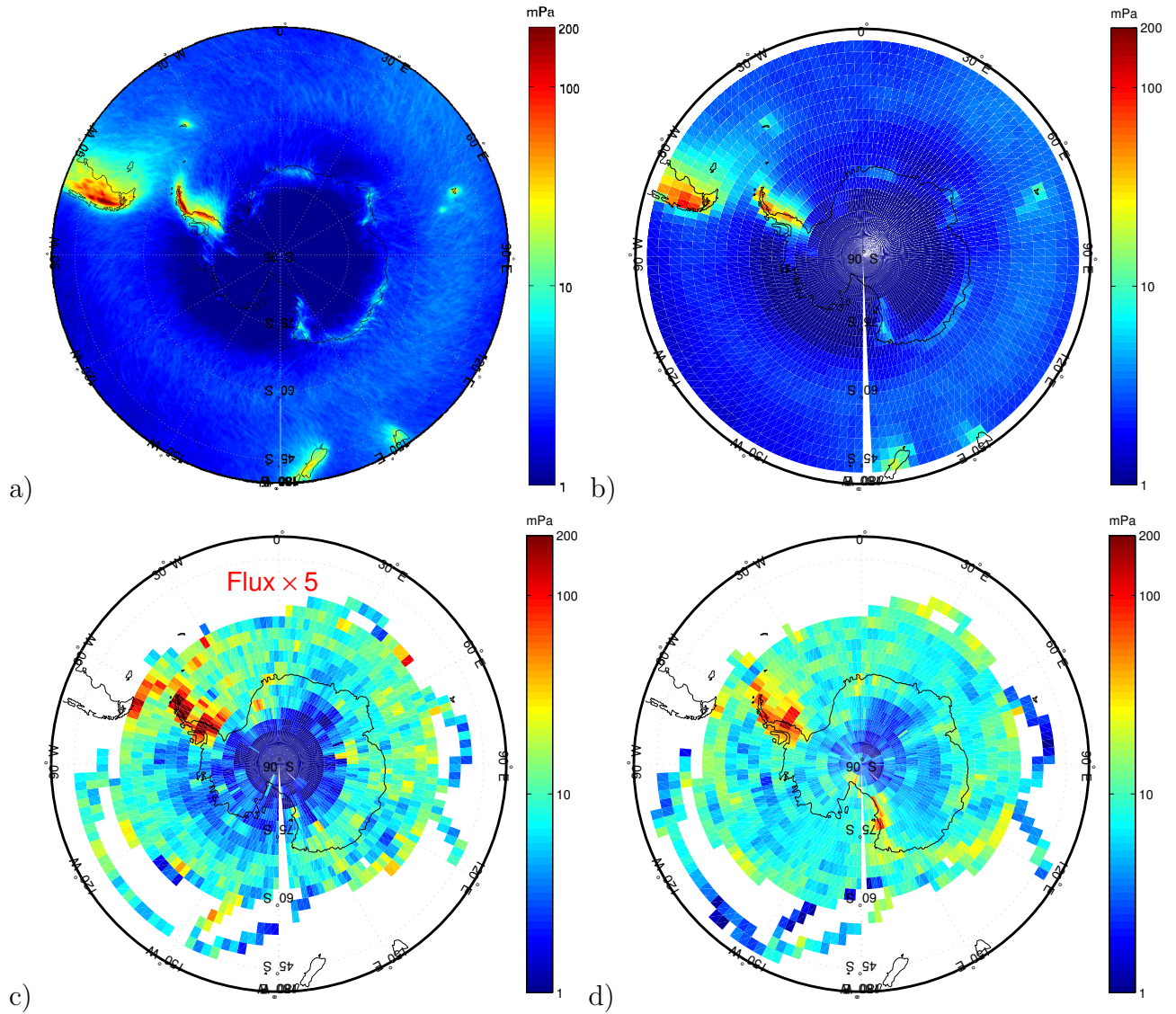
Figure 3.1: Time-averaged momentum fluxes a), b), c) from the ECMWF and d) from Concordiasi observations at 19 km. The ECMWF fluxes are shown a) with full resolution, b) averaged on the same grid as the Concordiasi data, and c) sampled at the same times as the Concordiasi balloons. The ECMWF fluxes represented in c) have been multiplied by 5.

a)   b)
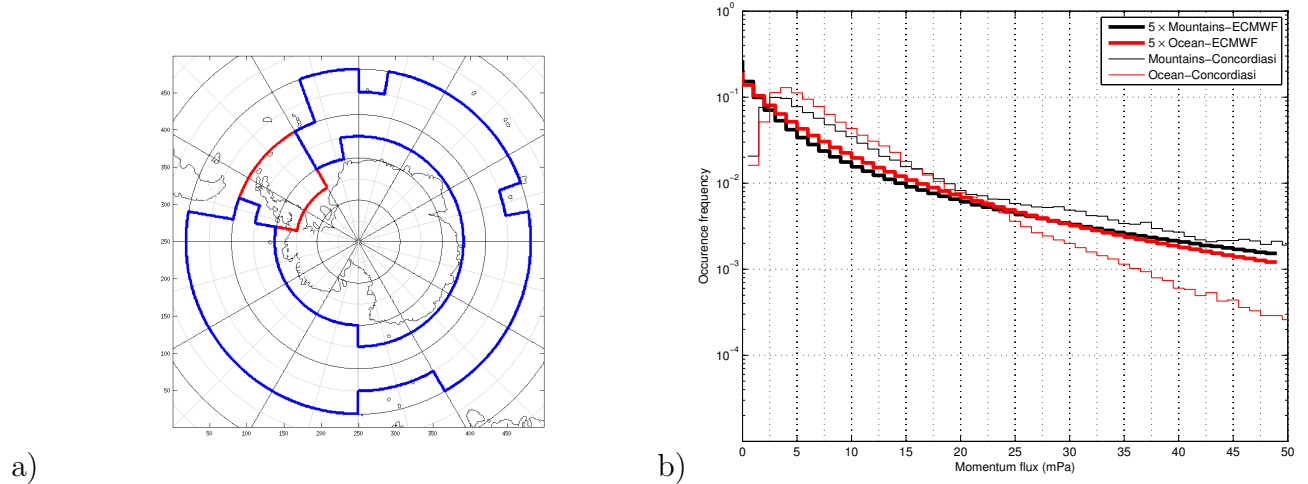
Figure 3.2: a) Map denoting the Moutain and Ocean regions, and b) regional PDFs of the momentum fluxes in the ECMWF (at 19 km) and in Concordiasi. The fluxes from the ECMWF have been multiplied by 5 before calculating their PDF.

with the orographic gravity wave (OGW) events, whereas the ocean regions devoid of any topography are associated mainly with nonorographic gravity waves (NGWs). The PDFs in ECMWF and Concordiasi exhibit long tails that account for highly intermittent GWs (*Hertzog et al.*, 2012), and are consistent with the momentum fluxes time evolution (not shown) that oscillates between weak fluxes (<10 mPa) and rare intense events where the fluxes exceed 500 mPa locally. The PDFs in the ECMWF and Concordiasi are very different, with a small contrast between OGWs and NGWs in the ECMWF. Intermittency over mountains and oceans is almost indistiguishable for fluxes smaller than 10 mPa (20 mPa) in the ECMWF (Concordiasi). For larger fluxes (>40 mPa), occurence frequency over mountains is approximately one order of magnitude bigger than that over oceans. Moreover, calculations of the 90th percentiles show that 86% (55%) of the total flux is due to the 10% largest GW events over topography (smooth terrain) in ECMWF, whereas they account for 64% (29%) of the flux in Concordiasi over mountains (oceans). In accordance, calculation of the Gini coefficient (*Gini*, 1912) yields values of 0.9 and 0.7 for OGWs and NGWs

60

momentum fluxes respectively. Hence, this results in more occurences of larger fluxes over mountains than over smooth terrain, which is consistent with the findings of *Hertzog et al.* (2012).

3.7.3 Time and spatial variability of the GW fluxes and their intermittency

We mentioned earlier the importance of quantifying time and spatial variations of the GW momentum fluxes to take this variability into account in the parameterizations. In the previous section, we have briefly examined the mean geographical distributions of the fluxes, but we have not analyzed the time evolution of the fluxes regionally. This is presented in the following section.

Figure 3.3 (left panel) displays the monthly-averaged GW momentum fluxes calculated in the ECMWF at high-resolution from September 2010 throughout January 2011. We note an increased GW activity in general, and particularly for NGWs over oceans from September to November and OGWs on the Peninsula. Note here that these maps are shown at 19 km, i.e. below the zonal wind revearsal in summer. Above this revearsal, it is expected that mountain waves also exhibit a significant decrease in summer (*Ern et al.*, 2011). The decrease of 90% in OGW momentum flux (see Table 3.1) from November to December is quite striking, compared to the 30% decrease on OGWs' fluxes for the same period. We have also represented the monthly-averaged isotachs at 70 hPa on the different panels of Figure 3.3 to identify the lower stratospheric jets. They provide evidence that the decrease seen in both NGW and OGW (in the vicinity of the Peninsula) is related to the weakening of the winds when entering the Southern Hemisphere summer in December. In the Southern Hemisphere, the polar jet centered at 60°S reaches its maximum speed in August-September (mid- to late winter), and breaks up in November-December (mid- to late spring). It explains the considerable depletion in OGW flux as the wave's amplitude

is directly proportional to the wind speed. This lack of intense events after November is also expected to show a strong variability on the intermittency of the momentum fluxes. The middle and right panels of Figure 3.3 depict the ECMWF fluxes with the balloon sampling ($\times 5$) and the Concordiasi observations as previously. A good seasonal agreement shows up, although a higher contrast (approximately by a factor 2 as before) is found in the ECMWF between the a region that includes the Plateau, the Ross and Amunsen Seas, and the other regions. With regard to the time average fluxes, the values of ~ 9.4 mPa obtained from Concordiasi for the NGWs in November is 10 times larger than the value of 0.9 mPa derived from the Vorcore observations by *Plougonven et al.* (2013).

We have represented the PDFs of the GW fluxes during the entire Concordiasi period in Figure 3.4, and distinguishing the contributions from OGWs and NGWs using the same regions as in Fig. 3.2a). A large portion of the differences between the ECMWF and Concordiasi arises because of the different sampling and its spatial and time evolution. In September, the balloons are progressively being released from the launch station, therefore the initially low density of measurements has increased by 70% and reached its maximum in October and November. In December, this density decreases by 50% relative to the maximum while the balloons land, and by January only one balloon remains flying over the ocean. Thus, the balloons do not intercept the Peninsula during that month, which explains the disappearance of the oceanic PDF in Fig. 3.4e). In contrast with Concordiasi, the GW events are observed in the ECMWF at every grid points, irrespective of the position. Therefore, there is no bias introduced by sampling methods in the ECMWF. However despite those differences, we identify the same robust seasonal variability seen in Figure 3.3, with a monthly decrease of the mean momentum fluxes in time, illustrated by the disappearance of the large values tails in December and January. This decrease of the tails also reveals a drop in intermittency with a minimum for the OGW momentum

Table 3.1: Monthly means ($\bar{F}$) of the Concordiasi and ECMWF (resolved) GW momentum fluxes (in mPa) and Gini coefficients. The first value corresponds to Concordiasi, and the second corresponds to the ECMWF.

	Oct		Nov		Dec	
	$\bar{F}$	I_g	$\bar{F}$	I_g	$\bar{F}$	I_g
OGW	54.3/9.8	0.73/0.86	36.2/13.2	0.64/0.89	5.6/1.2	0.34/0.69
NGW	11/2.8	0.4/0.67	9.4/2.1	0.36/0.66	7.1/1.5	0.36/0.63

fluxes in December. The weakening of the wind at 19-20 km of altitude during this period filters out the GW with lower phase speeds, that carry the largest portion of momentum flux, causing this drop in GW activity and intermittency. In spite of the agreement on the seasonal variations, the PDFs in the ECMWF show again a significantly smaller contrast between OGWs and NGWs. We may note that the PDF above oceans show less variability than those above mountains, which is also evidenced by the calculation of the 90th percentile. In September the amount of GW activity explained by the 10% largest events (i.e. 84% for OGWs and 54% for NGWs) reduces to 55% in January for the Peninsula, while it is only reduced to 44% over the oceans (values are shown only for the ECMWF because of the insufficient sampling of events by the balloons in September and January). Values of the Gini coefficient (see Table 3.1) are consistent with this observed decrease in intermittency from September throughout January. The values of Gini coefficients calculated from the ECMWF compare fairly well with the values of 0.8 and 0.5 obtained from Vorcore by *Plougonven et al.* (2013). Nonetheless, Gini coefficients from the ECMWF are usually larger than those derived from the observations by 5-25% for the OGWs, and by 50-55% for the NGWs, suggesting a possible effect of the sampling.

3.8 Case studies

Case studies on large OGW and NGW localized events are presented in this section, to assess the realism of the simulated waves in the ECMWF and compare the
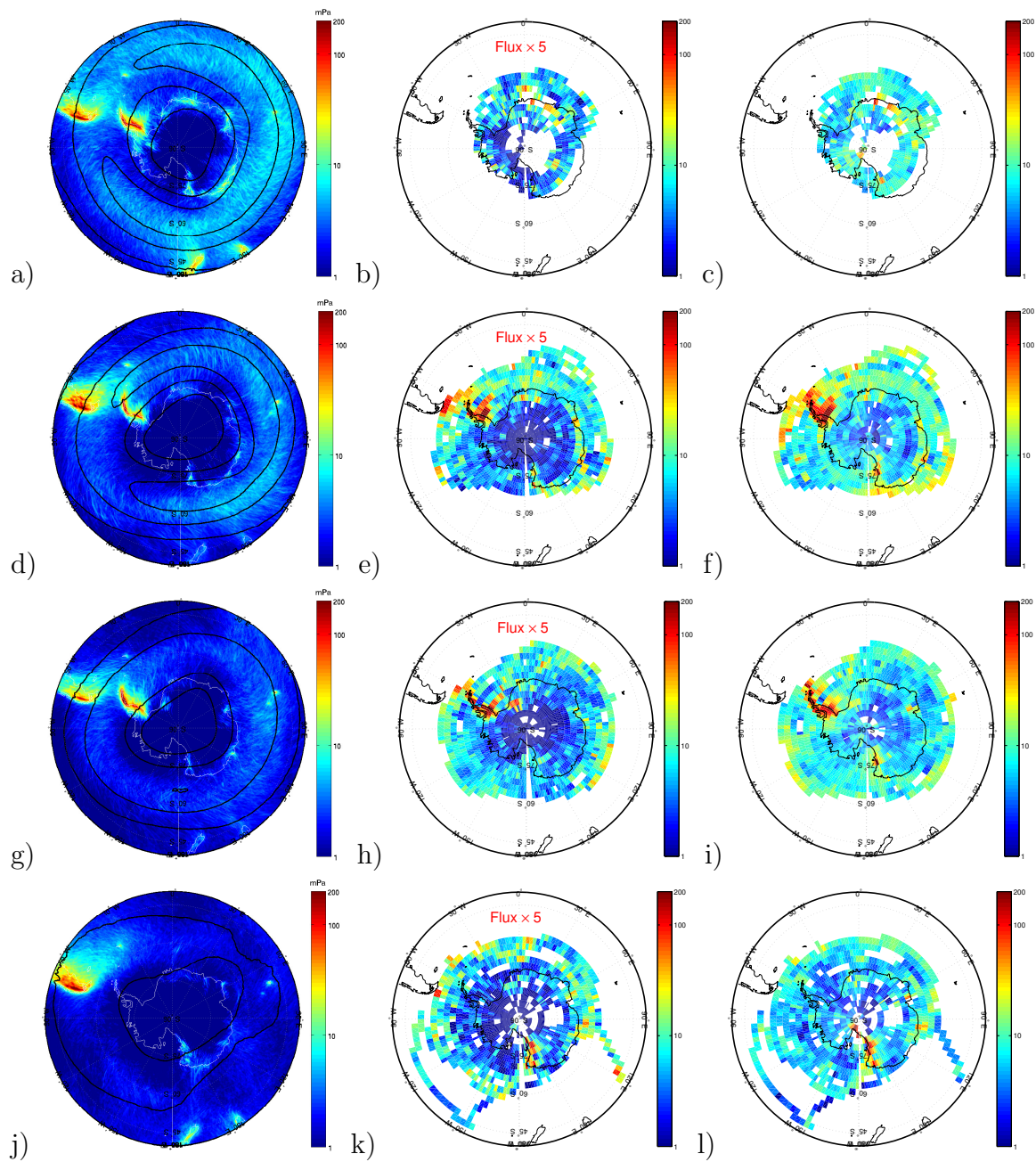
Figure 3.3: Monthly-averaged of the momentum fluxes at 19 km from (left panel) ECMWF, (middle panel) ECMWF with the balloon sampling (×5), and (right panel) Concordiasi, for (a,b,c) September, (d,e,f) October, (g,h,i) November, and (j,k,l) December. The black contours on the left panel represent isotachs at 19 km with increments of 15 m s^{-1}.

64
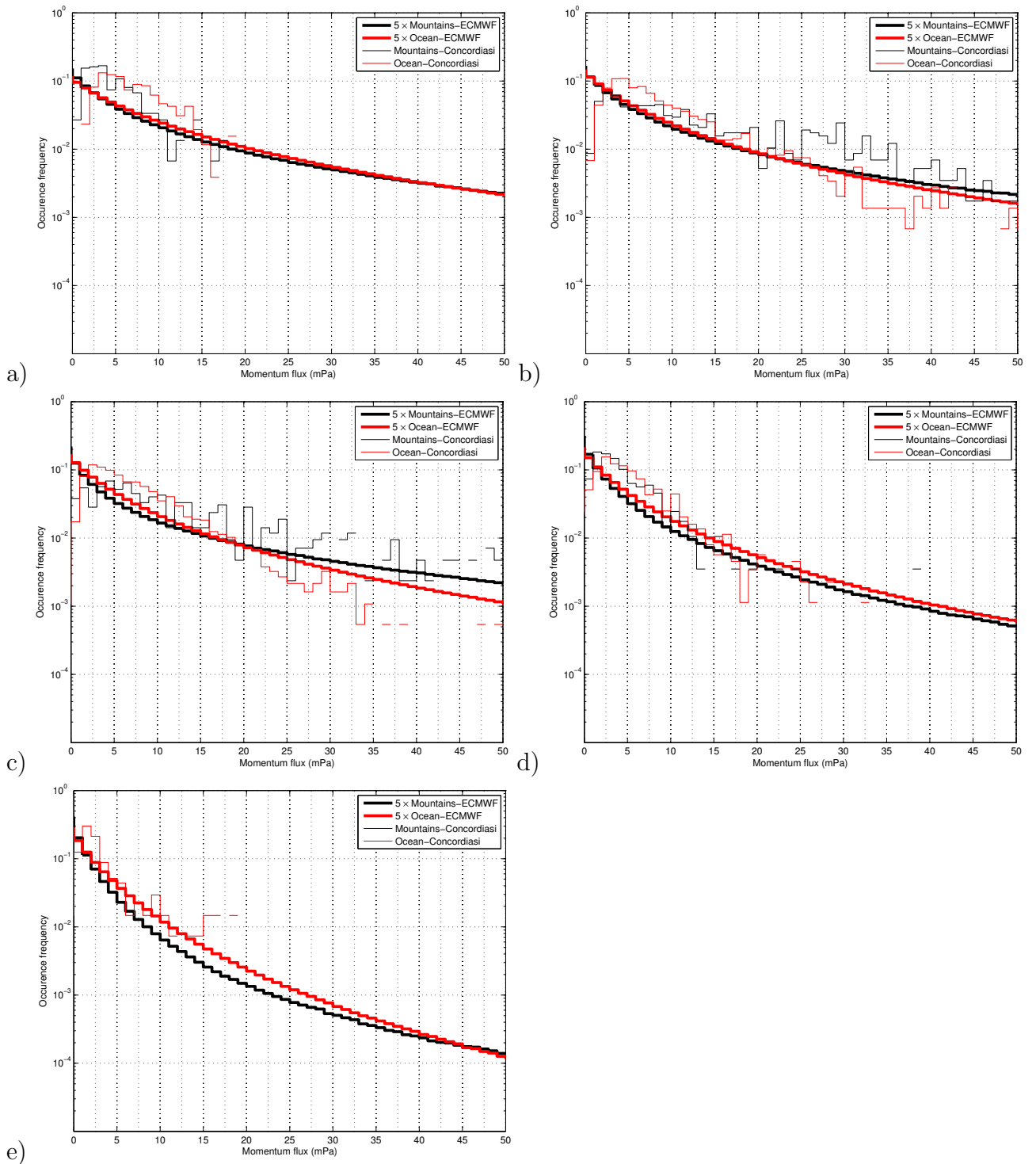
Figure 3.4: Monthly PDFs of the ECMWF and Concordiasi momentum fluxes by regions for a) September, b) October, c) November, d) December, and e) January. The ECMWF fluxes have been multiplied by 5 before calculating their PDFs.

simulated wave field to the balloon observations. The synoptic meteorological conditions are presented using the ECMWF analyses, and the mean spatial distribution of momentum fluxes and their magnitude are compared to Concordiasi for each case.

3.8.1 OGW event: 8-11 October 2010

The synoptic meteorological situation for the 9 October 2010 at 12UTC is illustrated in Figure 3.5. At mid-levels, the situation consists in a large cyclone west of the Peninsula and rather weak winds over the Peninsula . The upper analysis depicts a jet right exit region at the tropopause in the lee of the southern Andes and the Peninsula. During this period, the Concordiasi balloons were drifting in the vicinity of the Peninsula (Fig. 3.5a)), hence the observed GW activity is related to OGWs.

The maps of mean momentum fluxes are displayed in Figure 3.6, and represent the ECMWF fluxes a) at full resolution, b) with the balloon sampling (multiplied by 5), c) and the fluxes derived from Concordiasi. The GW fluxes calculated in the ECMWF with native resolution denote large OGW events generated by the Andes and the Peninsula with local values as high as 100 mPa, and smaller values over the ocean in their lee in the region 50-20°W. We note a connection between the activity upstream ($\sim$20 mPa) and over the Peninsula ($\sim$80 mPa). The geographical distribution of the large values of GW momentum fluxes ($>$30 mPa) agree very well in the ECMWF and Concordiasi. Over the oceans, general regions with fluxes between 10-50 mPa within the band 55-65°S correspond, but identifying structures clearly is still difficult due to the balloon sampling, as previously. On another hand, the contrast between the Peninsula and continental Antarctica (south of 70°S) is higher for the ECMWF than for Concordiasi. The mean value of the momentum flux for the region shown in Fig. 3.6 is 19.8 mPa.
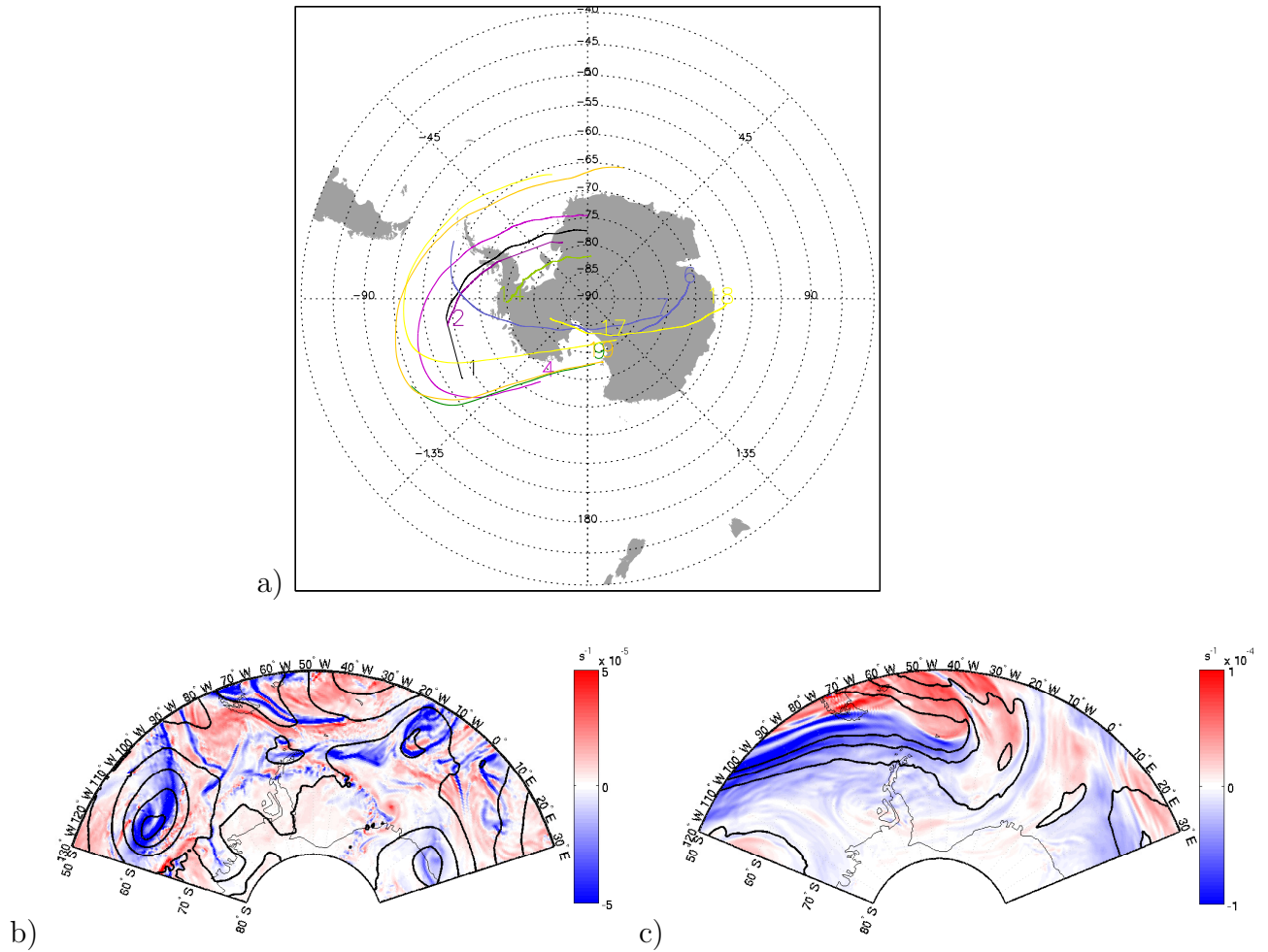
Figure 3.5: a) Map showing the balloon trajectories between 8-11 October 2010, b) map of vertical vorticity at the surface (shaded contours) and height of the 500 hPa geopotential surface in km (black contours) with increments of 100 m, and c) map of vertical vorticity (shaded contours) and isotachs (black contours) at the tropopause (200 hPa). b) and c) are valid on 9 October at 12UTC.

67
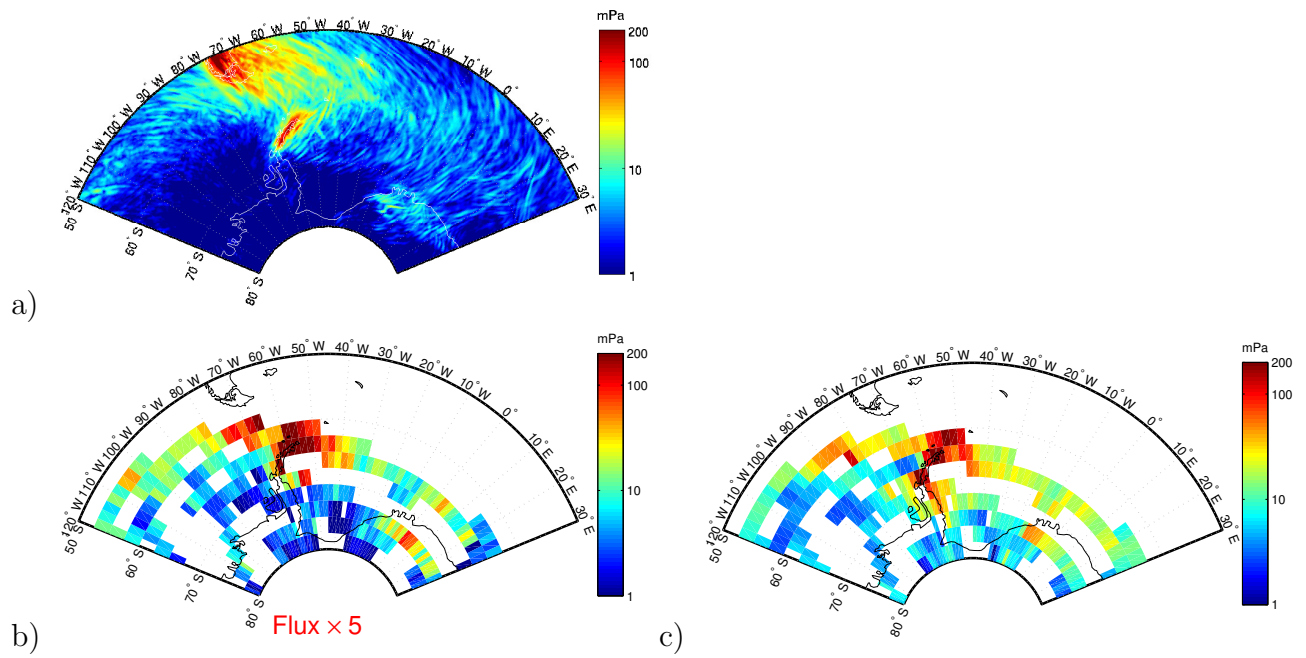
Figure 3.6: Time-averaged momentum fluxes for the period 8-11 October 2010 a), b) from the ECMWF and c) from Concordiasi observations at 19 km. The ECMWF fluxes are shown a) with full resolution, and b) sampled at the same times as the Concordiasi balloons. The ECMWF fluxes represented in b) have been multiplied by 5.

3.8.2 NGW event: 21-24 October 2010

On the 22 October 2010, 12UTC the meteorological situation consisted in a surface front oriented meridionally at 0-10°E, a longwave trough at midlevels (Fig. 3.7b)), and a relatively strong jet at the tropopause that intercepts the Peninsula (Fig. 4.7c)). The balloons were flying above the Peninsula and rather close to the shore in the Southern Ocean, observing this intense OGW episode and the high momentum fluxes in the lee of the mountains and also further above the ocean (Fig. 3.7a)).

The momentum fluxes in the ECMWF with full resolution depicted in Figure 3.8a) show a region with high values (∼100 mPa) in the vicinity of the Peninsula, and a larger region with smaller values within a range 10-50 mPa over the Southern Ocean collocated with the tropopause jet between 0-30°W, disconnected from the activity above the Peninsula (in contrast with the first case) and thus likely associated with NGWs. We focus on that particular wave packet here. The spatial distributions show a fair agreement on the location of the high values of the flux (although not as good as for the previous case). The observed fluxes are smaller than those for OGWs, but cover a wider area. The activity is collocated with the edge of the jet at the tropopause located 60°S. The factor 5 used here for the ECMWF slightly overestimates the values over the ocean here. Once again, we note the large contrast between ocean and Plateau and vicinity in the ECMWF data. The mean value of the momentum flux is smaller than for the first case by a factor 0.5 (8.7 mPa), owing to NGW momentum fluxes that are weaker locally than OGW in general.

3.9 Conclusions and discussion

We have examined and compared the GW momentum fluxes at 19-20 km of altitude in the Southern Hemisphere derived from in-situ measurements from the Concordiasi SPB (*Rabier et al.*, 2010), and from the ECMWF operational at 0.125°
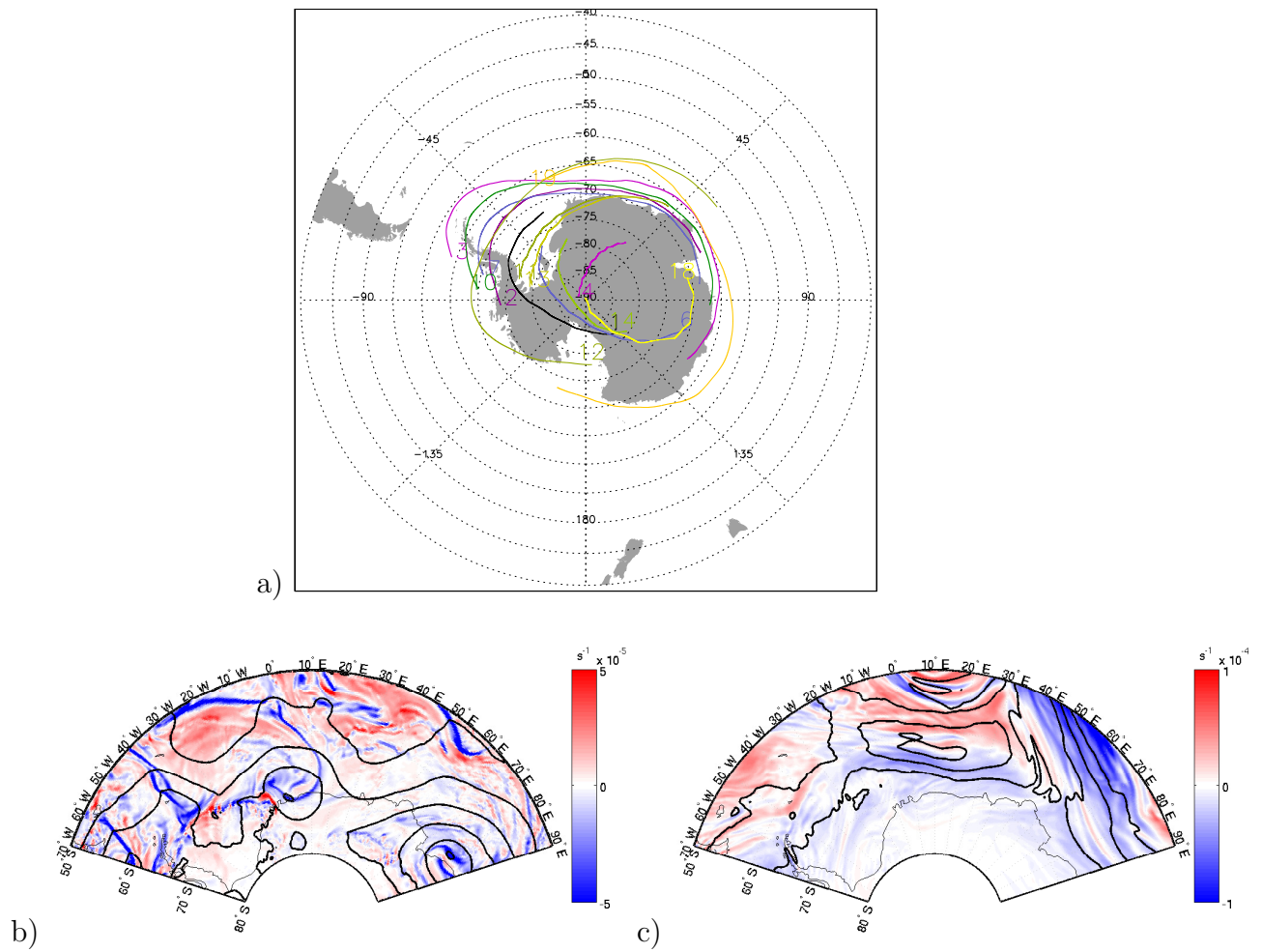
Figure 3.7: As in Figure 3.5, except for the period 21-24 October 2010. b) and c) are valid on 22 October at 12UTC.

a)

b) Flux × 5

c)
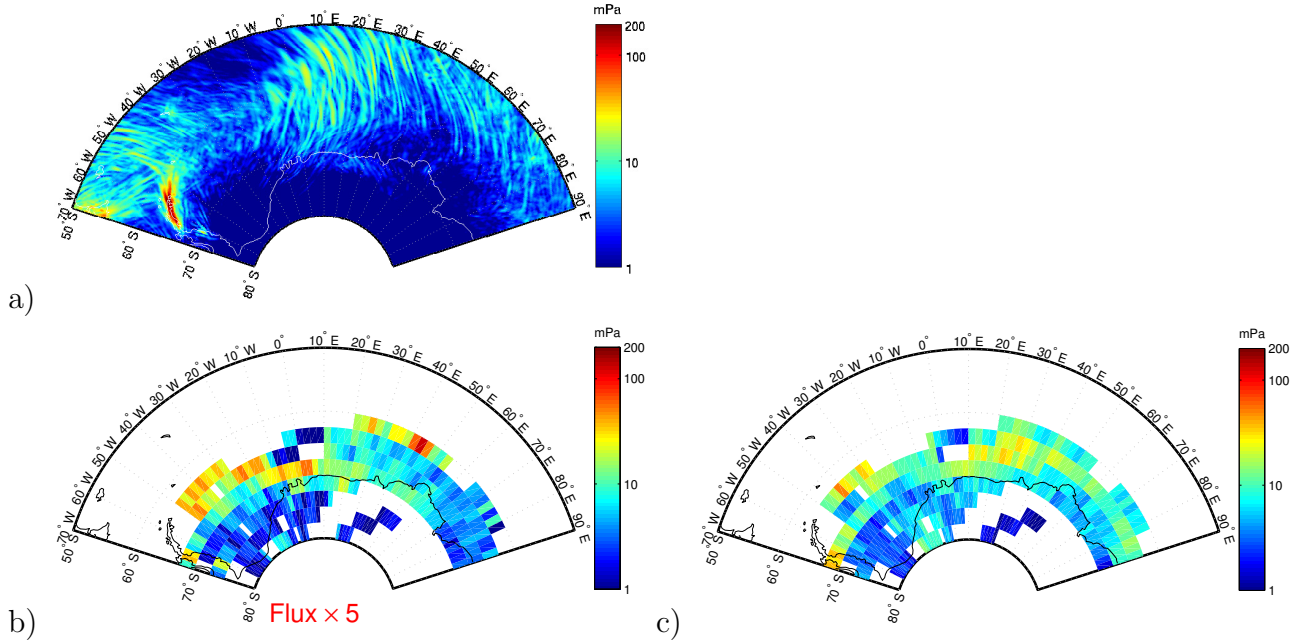
Figure 3.8: As in Figure 3.6, except for the period 21-24 October 2010.

horizontal resolution for the period September 2010-January 2011. The Concordiasi balloons constitute an unprecedented and unique dataset well adapted for studing the entire spectrum of GWs for long-duration and over large regions. The main purposes of this study were to 1) to assess the realism of the ECMWF GW field globally and for few cases of intense GW episodes by comparison with the Concordiasi observations, and 2) to provide mean climatologies of the GW momentum fluxes in the lower stratosphere for regions at high latitudes, examine their intermittency, and study the seasonal and regional variability.

First, we provide a mean spatial distribution of momentum fluxes. We find a reasonable agreement on the geographical locations of GW hotspots (southern tip of the Andes, Antarctic Peninsula, islands, over the ocean), although we note a difference on the magnitude by a factor 5. Mountains are associated with mean fluxes on the order of 100 mPa, and dissociate from islands or smooth terrain with fluxes $\lesssim 10$ mPa. The contrast between the Antarctic Plateau and the other regions is 2 times larger in

the ECMWF than in the Concordiasi observations. The PDF of the GW momentum fluxes exhibit similar shapes with long tails for the highest values, that evidence a more intermittent behavior over mountainous regions than oceans. We show that the 10% largest wave events account for 86% (55%) of the total momentum flux in regions with topography (flat terrain) in ECMWF, and 64% (29%) in the Concordiasi observations.

Seasonal maps of the fluxes at 70 hPa show a decrease of the GW activity between late spring and early summer associated with the weakening of the stratospheric jet, that filters the GWs with low ground-relative phase speeds. Mean values of the OGW and NGW momentum fluxes are reduced by 90% and 30% over that period, which is also evidenced by the disappearance of the high value tails of the PDFs. The filtering of the intense episodes also acts to produce a more equal distribution between low and higher values, and decreases the intermittency. Despite an overall agreement on the shape of the PDFs and on the time variations, we note that the distinction between OGWs and NGWs is much smaller in the ECMWF than in the observations.

In the last part of the present study, we have provided a comparison of the GW momentum fluxes in Concordiasi and the ECMWF for 2 individual intense GW cases. We draw the same conclusions as for the global study: we find a good agreement on the geographical distribution, although we observe discrepancies on the magnitude with mean fluxes 5 times bigger on average in Concordiasi than in the ECMWF. We observe once again a bigger contrast between the regions of small and high fluxes.

In conclusion, we note an overall correct geographical and seasonal agreement on the momentum fluxes calculated from the ECMWF analyses and the Concordiasi observations, and on the shape of their PDFs. However, the magnitude of the fluxes are 5 times bigger in the observations than in the analyses, and we remark a striking contrast between regions of low and higher values in the ECMWF resulting from resolution (*Plougonven et al.*, 2013). Those conclusions are valid at global scales

and also for individual GW events. PDFs from the observations show occurence frequencies on average 10 times bigger than those from the ECMWF. The results from the present study suggest that ECMWF is capable of representing GW accurately the geographical and seasonal variations of the resolved GW momentum fluxes, thus the ECMWF analyses can be used to study the spatial, seasonal and interannual variability.

In closing, we now discuss one issue identified by *McLandress et al.* (2012): A lot of studies are devoted to understand the bias in the simulated delayed springtime breakdown of the stratospheric polar vortex in global models (*Eyring et al.*, 2010; *Butchart et al.*, 2010). Using analyses increments, *McLandress et al.* (2012) affirm that this bias arise primarily because missing GWD at 60°S cannot act to decceler-ate the stratospheric jet. It is unclear whether resolved or parameterized GW are in cause (*Eyring et al.*, 2010), but the fact that there is insufficient GWD in the Southern Hemisphere stratosphere in winter and spring represents a general consensus. *McLan-dress et al.* (2012) attribute this gap in GWD to OGWD from small localized islands located at those latitudes, but they do not totally rule out NGWD. Both effects are not well represented in GWD parameterizations, therefore they both remain poten-tial candidates to explain this missing drag. The Concordiasi observations are fit to provide elements for this discussion. The zonally-averaged momentum fluxes for Oc-tober calculated from Concordiasi are represented in Figure 3.9. We observe a general progressive poleward decrease of the total GW fluxes south of 72°S, consistent with satellite calculations of momentum fluxes from HIRDLS and SABER (*Geller et al.*, 2013). The peak at 70-75°S here is likely associated to the Antarctic Peninsula. More relevant to the question of the missing drag are the contributions from OGWs by the islands in the 55-60°S latitude band (black line) and the NGWs over the ocean (red line). NGWs peak significantly higher (by 80-85%) than OGWs with a value of 16-17 mPa and almost merging with the total mean. This means that the primary

contribution comes from NGWs over the ocean, and clearly dominates the secondary contribution from small islands in this region. Thus, we conclude that the missing GWD is likely related to missing NGWD. However, we need to stay cautious because of the limitations of our data, that consist only in one occurence over the year, and with a large impact of the balloon sampling over oceanic regions. Climatologies over several years using more SPBs are necessary for more definitive conclusions. 5 years seems to be adequate to take the annual variability into account and is the value advocated by *McLandress et al.* (2012). We have not studied the other potential reason proposed by *McLandress et al.* (2012), that is the meridional propagation of mountain waves into the jet core, as it involves calculations of phase speeds and directions of propagation and this is beyond the scope of the present study. Hence, we cannot rule out this effect.
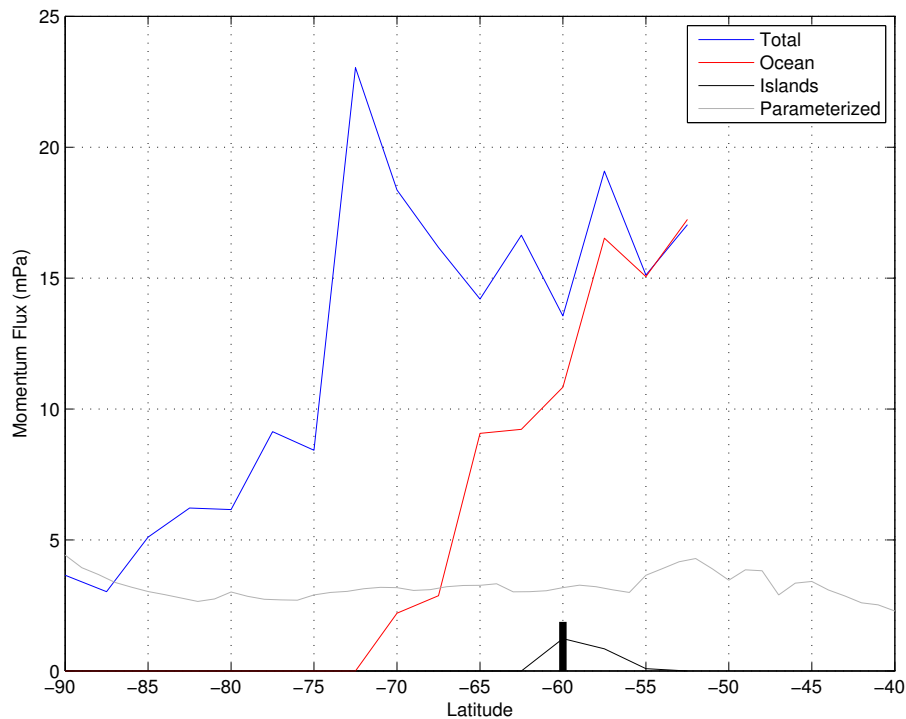
Figure 3.9: Zonally-averaged momentum fluxes weighted by the number of observations for october 2010 at 70 hPa from the Concordiasi observations. Islands denotes the region with small isolated islands located in the 55-60°S latitude band (region 3 in *Plougonven et al.* (2013)'s Figure 5).

3.10 Acknowledgements

3.11 Perspectives

Nous avons montré dans la présente étude qu'il y a un bon accord géographique et saisonnier sur les flux de quantité de mouvement des ondes de gravité et l'intermittence entre l'ECMWF et les observations ballons. En revanche, la grandeur des flux est sous-estimée d'un facteur 5 dans les analyses ECMWF.

Pour aller plus loin, des perspectives communes avec l'étude PreConcordiasi se dégagent comme l'étude des spectres de vitesses de phase et de longueurs d'ondes, et la direction de propagation des ondes aussi bien dans les données Concordiasi que les analyses de l'ECMWF, avec les mêmes objectifs que pour l'étude Concordiasi : l'étude du réalisme du champs d'onde de l'ECMWF et la validation ou non, et obtenir des climatologies globales pour les régions de l'hémisphère sud incluant l'océan austral et le continent Antarctique. En outre, *McLandress et al.* (2012) ont proposé une autre raison pour l'explication de la traînée manquant à 60°S : des simulations à haute résolution ont montré qu'il y avait propagation méridionale d'ondes de montagne à l'intérieur du coeur du jet qui se situe près de 60°S (*Sato et al.*, 2009). Nous n'avons pas étudié cet effet, mais l'analyse de la direction de propagation des ondes permettrait de quantifier cet effet. Cela nécessiterait un travail supplémentaire.

CHAPTER IV

Prévisibilité des trajectoires lagrangiennes de ballons stratosphériques ouverts

4.1 Problématique de la prévision opérationnelle des trajectoires ballons

Les possibilités pour pouvoir continuer à étudier l'atmosphère en utilisant des Ballons Stratosphériques Ouverts (OSB) dépendent de plus en plus de nos capacités à pouvoir prévoir la trajectoire des ballons. Il y a donc un besoin crucial d'améliorer la prévision afin de pouvoir continuer d'utiliser des mesures ballons. Pour répondre aux mesures de sécurité appliquées à ce type de vol, les OSB n'ont pas le droit d'attérir dans des zones densémment peuplées ou construites comme les routes à fort traffic, ou les villages. Par conséquent, réduire les incertitudes sur la descente finale et le point de chute des enveloppes des ballons et leur chaîne de vol (qui peuvent peser jusqu'à une tonne) est vital pour faciliter les opérations OSB et implémenter ces règles de sécurité et réduire les risques.

A l'heure actuelle, le CNES utilise les sorties du modèle de l'ECMWF, ce qui conduit à d'importantes incertitudes sur la position finale de descente du ballon. La réduction des incertitudes sur les prévisions des trajectoires ballon passe par une meilleure représentation de l'écoulement atmosphérique d'un modèle numérique. Les

limitations pour la prévision des trajectoires ballons dans l'atmosphère proviennent de plusieurs origines. La production d'une prévision nécessite un modèle qui simule l'écoulement atmosphérique, et un modèle qui calcule le vol du ballon à partir de cet état atmosphérique. Les incertitudes dans les prévisions proviennent :

1. du fait que le modèle est imparfait ;

2. des limites en résolution et sur la fréquence de sortie du modèle ;

3. d'une connaissance imparfaite de l'état de l'atmosphère et la nature chaotique des mouvements atmosphériques (*Aref*, 1984, 1990).

Dans ce chapitre, nous tentons de répondre au $2^{\text{ème}}$ type d'incertitudes en examinant si l'utilisation d'un modèle méso-échelle améliore les prévisions, et s'il est possible d'améliorer et d'aborder le $3^{\text{ème}}$ point en assimilant des données de radiosondages disponibles avant le vol des ballons.

4.2 Quelques bases sur l'assimilation de données

Comme nous l'avons mentionné précédemment, l'amélioration des prévisions passe par une meilleure connaissance de l'état initial atmosphérique. Les *prévisions* (forecast) sont entachées d'erreur qu'on cherche à réduire au moyen d'observations, qui contiennent elles-aussi des erreurs, pour produire une *analyse*. L'assimilation de données dans un modèle consiste donc à combiner sorties modèles et observations de manière optimale.

4.2.1 Le filtre de Kalman

Nous décrivons ici le filtre de Kalman qui est à la base du filtre de Kalman d'ensemble. Considérons le vecteur d'état $\mathbf{x}$ qui décrit les variables d'état du modèle

78

et supposons que sa fonction de densité de probabilité (PDF) suit une loi normale de moyenne μ et de covariance B :

$$p(\mathbf{x}) \propto exp\left(-\frac{1}{2}(\mathbf{x} - \mu)^T B^{-1}(\mathbf{x} - \mu)\right), \tag{4.1}$$

où $p(\mathbf{x})$ est la PDF dite a priori, obtenue en propageant le modèle dans le temps et qu'on va corriger en utilisant des données supplémentaires. L'indice ^{T} indique une transposition de matrice. On suppose la distribution des erreurs d'observation connue. Dans le cas d'observations provenant de radiosondages par exemple, elles ont été déterminées à partir de comparaisons de profils verticaux par rapport aux analyses du NCEP prises comme référence. On suppose que les observations $\mathbf{y}$ ont aussi une PDF de moyenne $H\mathbf{x}$, et de covariance R en lien avec l'erreur d'observation. La fonction qui fait le lien entre les observables et $\mathbf{x}$ est appelée opérateur d'observation et est représenté par la matrice H dans l'éEquation 4.1. $H\mathbf{x}$ décrit la moyenne pour des observations sans erreurs, et R est l'erreur d'observation. La probabilité conditionnelle $p(\mathbf{y}|\mathbf{x})$ d'obtenir $\mathbf{y}$ connaissant $\mathbf{x}$ est donnée par la relation suivante :

$$p(\mathbf{y}|\mathbf{x}) \propto exp\left(-\frac{1}{2}(\mathbf{y} - H\mathbf{x})^T R^{-1}(\mathbf{y} - H\mathbf{x})\right). \tag{4.2}$$

En utilisant les équations 4.1 et 4.2 et le théorème de Bayes, on obtient la probabilité à postériori $p(\hat{\mathbf{x}}) = p(\mathbf{x}|\mathbf{y})$ (*Anderson and Moore*, 1979) :

$$p(\hat{\mathbf{x}}) = p(\mathbf{y}|\mathbf{x})p(\mathbf{x})$$
$$\propto exp\left(-\frac{1}{2}(\hat{\mathbf{x}} - \hat{\mu})^T \hat{B}^{-1}(\hat{\mathbf{x}} - \hat{\mu})\right), \tag{4.3}$$

où $\hat{\mu} = \mu + K(\mathbf{d} - H\mu)$, $\hat{B} = (I - KH)B$, avec le gain de Kalman défini par $K = BH^T(HBH^T + R)^{-1}$. I est la matrice identité. A partir du gain de Kalman, on

peut calculer l'analyse par la relation suivante:

$$\hat{\mathbf{x}} = \mathbf{x} + K(\mathbf{y} - H\mathbf{x}). \tag{4.4}$$

4.2.2 Le filtre de Kalman d'ensemble (EnKF)

Le filtre de Kalman d'ensemble (*Evensen*, 2003) est une approximation de Monte Carlo moins couteuse numériquement (selon le nombre de membres de l'ensemble choisi) du filtre de Kalman, qui ne nécessite pas de mettre à jour la matrice de covariance de la PDF de $\mathbf{x}$. Au lieu de celà, B est évaluée dans un ensemble de réalisations du modèle à partir de perturbations sur l'état initial. Le choix des perturbations initiales est donc essentiel afin d'échantillonner correctement la PDF des états atmosphériques possibles.

4.3   Données disponibles

Dans l'étude présente, nous examinons la prévisibilité des trajectoires OSB sur 3 cas d'étude durant la campagne Strapolété (*Huret et al.*, 2010). Au cours de l'été 2009, le CNES a lancé 9 OSB depuis la base d'Esrange $(21.107°\text{E}, 67.894°\text{N})$ non loin de Kiruna en Suède. Les OSB sont des ballons ouverts (non pressurisés) qui ont des durées de vol relativement courtes (<24 h) et qui volent depuis la surface jusqu'à près de 35 km dans la stratosphère avec du matériel scientifique embarqué qui peut atteindre au total 1 t. Ces ballons sont soumis à des équilibres thermodynamique et radiatif complexes. Le volume de ces ballons ouverts varie en fonction des conditions environnementales. Contrairement aux radiosondages, les OSB en vol ne se comportent pas comme des traceurs passifs, puisqu'un opérateur au sol peut contrôler l'altitude en relachant du gaz ou des ballasts. L'altitude et la position horizontale des ballons durant Strapolété ont été mesurées par GPS, et la température est donnée par un sondeur à ozone. Les mesures sont effectuées toutes les 10 s. Les composantes

du vent horizontal ont été déterminées à partir des positions successives du ballon, comme il se fait habituellement. Le but de Strapolété était de mesurer des espèces chimiques à longue durée de vie et des aérosols en stratosphère polaire.

En plus des OSB, le CNES a lancé des radiosondages journaliers plusieurs heures avant le lancer des ballons (horaire variable, entre 6 à 10 h), afin d'évaluer les conditions météorologiques. Les mesures de ces radiosondages ont été faites toutes les 2 s.

4.4   Principaux résultats

Les résultats principaux sont résumés ici:

1. L'utilisation de simulations numériques à méso-échelle sans apport additionnel d'observations améliore les prévisions des trajectoires des ballons par rapport aux trajectoires simulées à partir de l'ECMWF, en raison du gain en résolution spatiale et temporelle. La réduction de l'erreur sur la position finale varie selon les cas d'étude de plus de 50% à 10%.

2. L'assimilation d'un radiosondage unique disponible produit des incréments verticaux et horizontaux significatifs à l'analyse de plusieurs m s^{-1} sur le vent.

3. Pour des échánces (lead times) supérieures à 4-5 h, les corrections sont néanmoins rapidement advectées vers l'exterieur par l'écoulement simulé et l'information apportée par les observations disparait au centre du domaine.

4. L'assimilation d'un profil vertical peu de temps ($\sim$1 h) avant que le ballon n'atteigne son plafond a un impact positif sur la prévision des trajectoires et du point de chute du ballon. Par exemple, l'erreur sur la position finale est réduite sur un des cas de plus de 85%, par rapport a ce qu'on obtient avec l'ECMWF.

Cependant, on obtient des résultats un peu moins bons sur les 2 autres cas, qu'on attribue à des structures de petite échelle mal représentées par le modèle.

5. Les limitations les plus importantes de la configuration actuelle sont:

    (a) la simulation de la basse stratosphère. En effet on note une sensibilité à la hauteur du toit, et il faudrait par conséquent étendre le modèle plus haut encore verticallement, ce qui ne pose pas de difficultés particulières.

    (b) la connaissance de l'écoulement en basse stratosphère, pour bien décrire la phase plafond qui est critique. Ici, cela représente un véritable défi car les ondes de gravité peuvent contribuer à la dérive des trajectoires simulées. Il y a un besoin d'observations supplémentaires pour représenter ces ondes proches du toit, même si le modèle peut les décrire.

Les parties qui suivent sont basées sur un article en préparation. Elles sont donc rédigées en anglais.

4.5 "Prediction of Lagrangian balloon trajectories using the DART Ensemble Kalman Filter"

Prediction of Lagrangian balloon trajectories using the DART Ensemble Kalman Filter

Valérian Jewtoukoff[1], Riwal Plougonven[1], Albert Hertzog[1], Chris Snyder[2], and Glen Romine[2].

[1]Laboratoire de Météorologie Dynamique du CNRS, Ecole Polytechnique, 91128 Palaiseau Cedex, France.

[2]National Center for Atmospheric Research, Boulder, Colorado.

Abstract

Safety compliance issues for operational studies of the atmosphere with balloons require quantifying risks associated to the descent phase, and developing strategies to reduce the uncertainties on the location of the touchdown point. Traditionnally, trajectory forecasts are computed from ECMWF products. Here we use past experiments to investigate possible strategies for improving these forecasts. Trajectories for Open Stratospheric Balloons (OSBs) short-term flights are computed using mesoscale numerical ensemble simulations with the Weather and Research Forecast (WRF) model initialized with ECMWF operational forecasts, and with assimilation of radiosoundings using the Data Assimilation Resesarch Testbed (DART) Ensemble Kalman Filter (EnKF), for 3 case studies during the Strapolété summer 2009 Campaign in Kiruna, Sweden. It is shown that the use of mesoscale simulations slightly reduces the uncertainty on the final position of the balloon by 10% (70% in the best case scenario) relative to the ECMWF, owing mostly to the increase in spatial resolution and time output frequency. Assimilation of a vertical profile from a single radiosounding with DART produces significant increments in the velocity fields of several m s^{-1}, and the resulting forecast trajectories can be improved by 50%. We show that assimilation of a radiosounding ~1-2 hours prior to forecast reduces significantly errors and can reduce errors on the touchdown position by 90%. However, the improvements are not

systematic and remain very case dependent. Possible reasons to explain the discrepancies relative to the observed trajectories are then discussed and we find out that the trajectories are highly sensitive to small-scale horizontal or vertical features close to the maximum altitude of the balloons, that the model does not simulate correctly. The ensemble spread is analyzed to give insight on the predictability of the balloon trajectories, and we note that the initial ensemble perturbations can be improved in the future for better forecasts.

4.6 Introduction

As safety constraints become tighter, the possibility of pursuing the investigation of the atmosphere using large Open Stratospheric Balloons (OSB) has come to depend crucially on our capacity to forecast the balloons' trajectories. Improving these forecasts is therefore vital to ensure the continuation of such observational campaigns. In compliance with range safety procedures for this type of flight, OSBs cannot touchdown in densely inhabited or constructed areas such as high-traffic roads, or villages. Currently, the forecasts for balloon trajectories during campaigns coordinated by the Centre National des Etudes Spatiales (CNES; French Space Agency) are based on the European Centre for Medium-range Weather Forecasts (ECMWF) operational model outputs. There are major uncertainties on the balloon touchdown location of the order of several tens of kilometers for one whole trajectory. Reducing those uncertainties during the final balloon descent (under parachute) and improving the uncertainties on the landing position of both the flight chain and the balloon envelope is necessary to facilitate OSB flights with the more recent and tighter safety requirements. Indeed, each OSB flight is associated with a prior risk assessment that aims at quantifying the probability of balloon operations to cause catastrophic damages on the ground. As loads up to 1 ton reach the ground under an uncontrolled parachute, this risk value must keep below a given threshold so that the flight can be eventually

performed. The risk computation includes factors associated with the launching operations, the balloon flight and the landing operations. This last factor is generally the most important one. The risk evaluation, knowing the population density, obviously strongly depends on the ability to forecast the trajectory and the location of the landing of the balloon. Hence, large uncertainties on the wind profile along the balloon flight and descent result in a wide landing area during the risk assessment, and a larger a priori probability for the balloon and flight chain to induce damages, which may induce the cancellation of the flight.

Reducing the uncertainties on the forecast trajectories requires the prediction of the atmospheric flow, using numerical simulations. A great deal of effort has been devoted in the last decade to improve the atmospheric flow predictions using high-resolution mesoscale models (*Coniglio et al.*, 2010) and assimilation of surface and radiosondes (*Wheatley et al.*, 2012), radar (*Snyder and Zhang*, 2003; *Zhang et al.*, 2004; *Caya et al.*, 2005; *Aksoy et al.*, 2009, 2010), and satellite data (*Liu et al.*, 2012). In the ocean, Lagrangian techniques have been developed to predict drifter trajectories including Lagrangian stochastic models (*Paldor et al.*, 2004; *Griffa et al.*, 2004), Kalman filtering (*Özgökmen et al.*, 1999; *Piterbarg*, 2001; *Özgökmen et al.*, 2001), and Particle Filter methods (*Chin and Mariani*, 2009). Overall, these studies show positive outcomes from the assimilation. By assimilating clusters of drifters for short-term prediction (typically 3 days) with a Kalman-type filter, *Piterbarg* (2001) reduced the error distance from 100-130 km with a dispersion model to less than 20 km. Interestingly, he also showed that prediction for long term (15 days) were actually better than for the 5-10 days lead time and hence, the error in this case is not cumulative. *Özgökmen et al.* (2001) also conclude that assimilation of additional data with a Kalman filter is significantly beneficial for the prediction of drifters position with improvement up to 30% for timescales on the order of the week. In the atmosphere, *Hertzog et al.* (2003) have examined the accuracy of stratospheric analyses compared

to long-duration Lagrangian balloons and have showed that they agree fairly well, and that the discrepancies result from misrepresentation of mesoscale inertia-gravity waves in the analyses. *Keil et al.* (2001) also present a comparison between long-duration balloon data and analyses and forecasts. They showed that better initial conditions resulted in better forecasts for 2-5 days lead times with a reduction of 50% on average of the distance relative to the balloon in the Northern Hemisphere. They attribute the mismatch between analyses and balloons to large scale biases. Other studies have examined the accuracy of simulated trajectories in the stratosphere using the ECMWF analyses (*Knudsen and Carver*, 1994; *Knudsen et al.*, 1996). They conclude that the sparse spatial and time resolution of the ECMWF analyses used to compute their trajectories and biases between real and ECMWF winds caused significant errors. *Knudsen et al.* (2001) compared trajectories integrated using the ECMWF, U.K Meteorological Office (UKMO) and National Center for Environmental Prediction (NCEP) analyses. They showed that as of 1999 when the ECMWF introduced their new variational data assimilation system, it predicts air parcel trajectories significantly better than UKMO and NCEP. To our knowledge however, studies in the atmosphere for short-term prediction of balloons in mesoscale flows are still lacking.

The uncertainty in the forecast of a balloon trajectory results from several contributions with different origins. Producing the forecast involves a model describing the atmospheric flow, and a model for the flight of the balloon in this simulated atmospheric flow. Uncertainty in the forecasts arises from:

1. Uncertainty of the forecast flow, that results from:

    (a) the imperfect nature of the model,

    (b) the limitations in terms of resolution and output frequency (*Walmsley and Mailhot*, 1983; *Kahl and Samson*, 1986; *Kuo et al.*, 1985; *Knudsen and*

86

Carver, 1994),

(c) the imperfect knowledge of the initial flow and the chaotic nature of the atmospheric motions (*Aref*, 1984, 1990).

2. uncertainty in the modeling of the flight physics.

In our study, we aim at reducing the uncertainty related to point 1, mainly 1b and 1c. The use of a mesoscale model allows us to increase both spatial and time resolution but it is not clear a priori how much improvement on the trajectories this will bring. Moreover, mesoscale simulations alone cannot reduce errors that would be due to errors in the flow described by the ECMWF. Therefore, this motivates the assimilation within the mesoscale model of any additional data to reduce further uncertainties. For the CNES OSB campaigns, the only in-situ observations consist in a single available radiosounding released at the launch site a few hours before the balloon takes off, and data from the OSB itself. To summarize, our study aims at answering the following questions based on three case studies during the Strapolété 2009 Summer Campaign in Sweden:

a. Can we significantly improve the OSB trajectory forecast with mesoscale numerical simulations?

b. Can we further improve the forecast by assimilating a single radiosounding available a few hours before the OSB launch?

c. Can we make use of the OSB data during its ascent to improve the forecasts?

The article is organized as follows. In Section 4.7, we present the Strapolété Campaign, and the numerical and experimental setups using numerical simulation and data assimilation. In Section 4.8, results from those experiments are shown for the case studies. In the last section, we give our conclusions about the improvement

87

of predictability for balloon trajectories forecasts and discuss the limitations of our analysis.

4.7 Data and methodology

4.7.1 The Strapolété summer Campaign

From August 2$^{\text{nd}}$ to September 16$^{\text{th}}$ 2009, the French Space Agency (Centre National d'Etudes Spatiales (CNES)) launched nine Open Stratospheric Balloons (OSB) from the Esrange Space center launch base $(21.107°E, 67.894°N)$ near Kiruna in Sweden (see flight informations in Table 4.1) (*Huret et al.*, 2010). OSBs are open (zero-pressure) balloons that have one or several openings in their envelope. These balloons are used for short-lived experiments ($\sim$ 1-10h) and fly up to the stratosphere with significant payloads up to 1 t. Those balloons are subject to a complex thermodynamic/radiative equilibrium. Their volume varies as the environmental conditions change. It is influenced by radiative effects that increase or decrease the temperature of the balloon gas. In addition to this fairly complex flight physics, the flight after launch is not passive as for a radiosounding: the operator has some control on the altitude through the possibility of gas discharge or ballast release. This further complicates prediction of their trajectories (*Alexander and de La Torre*, 2003). In the Strapolété Campaign, the gondola transported about 35000 to 400000 m^3 of volume transporting a scientific payload of 90 to 500 kg. The altitude and horizontal location of the balloon are measured by a GPS and the horizontal wind components are inferred from the successive positions of the balloon. The temperature was also measured by ozone sounders. Measurements are performed every 10 s. The data from the OSBs were not assimilated within the ECMWF model suite. Those balloons aim at measuring long-lived species and aeorosols in the stratosphere with spectrometers and photopolarimeters. Once in the mid stratosphere, the balloons drift for a few

Table 4.1: Strapolété balloon flights. The red rows are the flights selected for our experiments.

Flight	Launch dd/mm/yyyy	Launch time (hour UTC)	Duration (hour)	Ceiling (km)
1	2/8/2009	1800	4h00min	29.56
2	7/8/2009	0125	5h15min	33.5
3	14/8/2009	0926	5h58min	33.5
4	16/8/2009	1620	7h13min	30.142
5	18/8/2009	1322	7h08min	30.086
6	24/8/2009	2028	5h42min	33.283
7	25/8/2009	1454	6h56min	36.122
8	26/8/2009	1953	4h41min	30.11
9	7/9/2009	1459	15h58min	33.911

Table 4.2: Strapolété radiosoundings

Case	Launch dd/mm/yyyy	Launch time (hour UTC)	Max altitude (km)
1	16/8/2009	0552	34.3
2	2/8/2009	1349	36.33
3	14/8/2009	0156	36.277

hours at typical altitudes of 29 to 36 km. Examples of OSBs' altitude time series and trajectories are shown in Figure 4.1 for the three balloons denoted by the rows overlined in red in Table 4.1.

During the Strapolété Campaign, CNES also released daily radiosoundings from the launching site typically $6 - 10$ h before the OSBs flights to evaluate the meteorological conditions. Those radiosoundings constitute the unique available observations to provide detailed information on the atmospheric state before each OSB launch. Measurements are done every 2 s from the surface up to about 35 km. Just like the OSBs those radiosounding were not assimilated in the ECMWF system. Informations about those radiosoundings are summarized in Table 4.2.
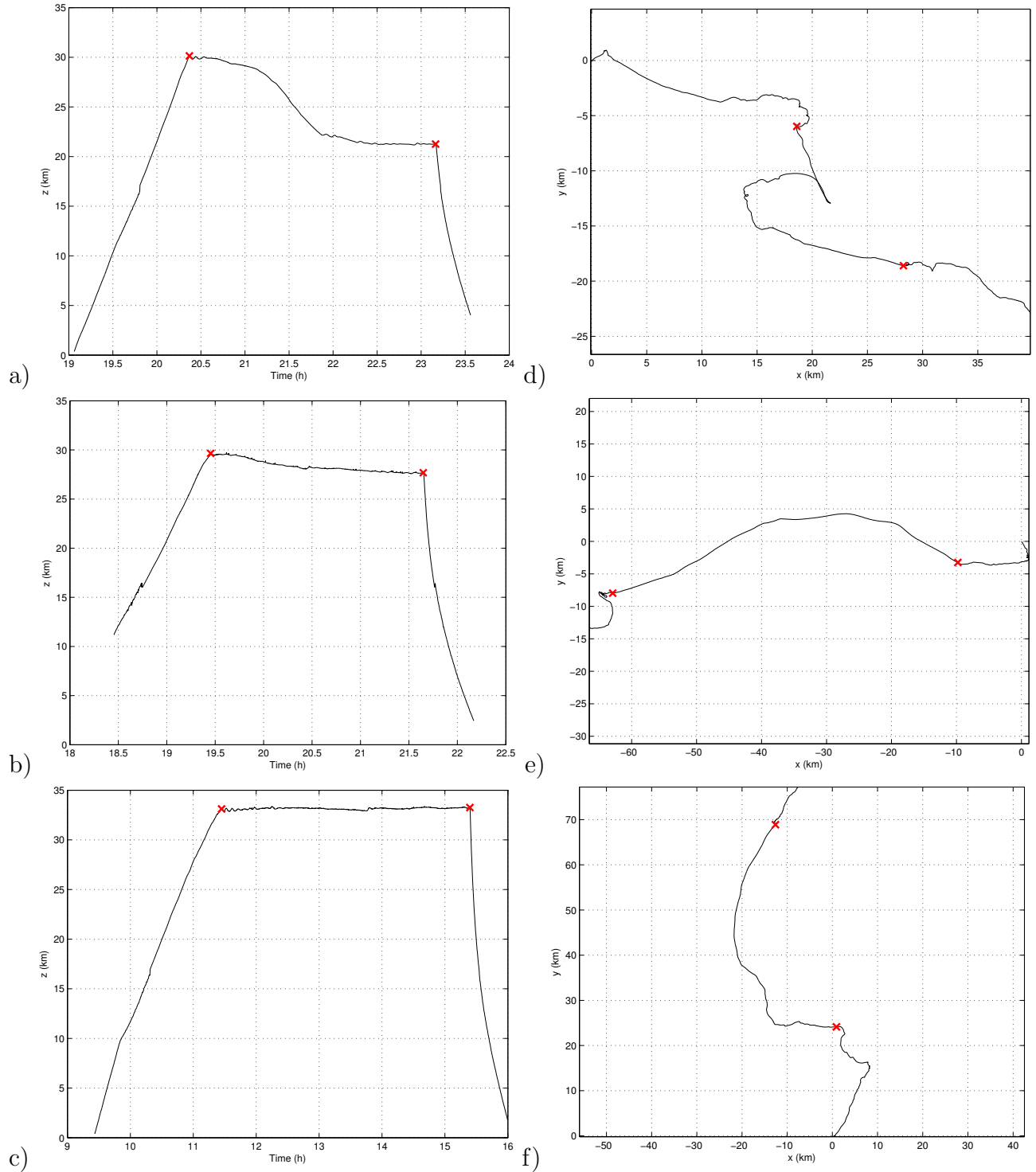
Figure 4.1: Altitude of the OSB for a) Case 1 (16 Aug 2009), b) Case 2 (02 Aug 2009), and c) Case 3 (14 Aug 2009) as a function of time. OSB trajectories are represented on the left side. The red crosses denote the start and end of the ceiling. Distances are calculated from the launch site. Note that the scale on the right is adjusted to each trajectory.

4.7.2 Numerical setup and EnKF data assimilation

We evaluate the predictability of Lagrangian OSB trajectories with the Weather Research and Forecast (WRF) Model (*Skamarock et al.*, 2008). WRF is a nonhydrostatic compressible mesoscale model well adapted for mesoscale prediction. It uses a staggered horizontal Arakawa C-grid (*Arakawa and Lamb*, 1977), and vertical stretched terrain-following grid. The dynamical core integrates the momentum and conservation equations using a flux-divergence 5th order scheme. Time integration uses a third-order Runge-Kutta split-explicit scheme to handle the acoustic waves on a small time step (*Wicker and Skamarock*, 2002). The model is well suited for data assimilation experiments and has been widely used with the DART package for convective prediction purposes using radar data assimilation (*Aksoy et al.*, 2009, 2010).

We use a single 1000 km × 1000 km grid centered on Kiruna in our experiments, with horizontal grid spacing of 10 km. We prescribe 120 vertical levels from the surface up to the pressure level of 5 hPa ($\lesssim$ 40 km), to resolve accurately the flow in the lower and mid- stratosphere. In order to avoid wave reflections at the model top, a sponge layer is applied damping vertical velocity within the 5 km below the model lid. The model levels are prescribed manually for our stratospheric simulations. We use physical schemes and parameterizations that are used in the NCAR's Antarctic Mesoscale Prediction System (AMPS; *Powers et al.* (2012)). The mean constant temperature in the stratosphere is chosen to be $T = 270$ K based on the mean temperature calculated in the ECMWF forecasts. The model outputs the dynamical fields at a hourly frequency. Summary of our WRF implementation is shown in Table 4.3.

The atmospheric initial and boundary conditions are provided by the ECMWF operational ensemble perturbations and forecasts from the Ensemble Prediction System (EPS; *Molteni et al.* (1995)). The ECMWF ensemble consists of an unperturbed

Table 4.3: Model physics.

Model physics	References
WRF single-moment 5-class scheme microphysics	*Hong et al.* (2004)
Grell-Devenyi 3D convective scheme	*Grell and Devenyi* (2002)
Yonsei University planetary boundary layer scheme	*Hong and Pan* (1996)
MM5-derived surface layer scheme	*Skamarock et al.* (2005)
Noah land surface model	*Chen and Dudhia* (2001)
RRTMG for longwave radiation	*Iacono et al.* (2008)
RRTMG for shortwave radiation	*Iacono et al.* (2008)

control forecast and 50 members generated by perturbing the operational analysis. The perturbations are constructed from singular vectors using a forward adjoint linear of the ECMWF model (*Molteni et al.*, 1995) to get a maximal growth for lead times of 48-72 h. The forecasts are available every six hours starting from each analysis and for 10 days. The perturbed analysis and forecasts have horizontal grid spacing of 0.25° of longitude and latitude corresponding to 15-20 km. The perturbed analysis has 62 vertical model levels from the surface up to 0.01 hPa and is used as our ensemble initial conditions, while the forecasts have 16 pressure levels extending up to 5 hPa and we use them for our lateral boundary conditions during time integration. Therefore, the minimum pressure allowed by the forecasts constrains the model height we use.

We use an Ensemble Kalman Filter (EnKF) system to assimilate the available data. The reader is referred to *Evensen* (2003) for a comprehensive explanation of the EnKF technique. In the present study, the Data Assimilation Research Testbed (DART; *Anderson et al.* (2009)) is used to perform data assimilation of the radiosoundings and part of the OSBs' observations in WRF. DART uses the ensemble adjustment filter method (*Anderson*, 2001) to control the effects of an underestimated analysis-error covariance resulting from the use of a finite number of members in an ensemble. For simplicity, we use the ECMWF ensemble, and hence our WRF ensemble comprises 50 members. Limitations of this choice will be described in Section

4.9. We use *Gaspari and Cohn* (1999)'s horizontal localization correlation function which is equal to 1 at the location of the observations and we choose a radius of 300 km. The observation error variance has been determined in previous studies from comparison between NCEP and radiosondes, with typical values of 3 m s^{-1} at the upper tropospheric jets and constant value of 2 m s^{-1} throughout the stratosphere. We assimilate all the available data within an assimilation window of 3 h. We have chosen to assimilate the horizontal wind components and temperature from the nearest radiosoundings for each case. Finally, we use an adaptative inflation technique (*Anderson*, 2009) to maintain the ensemble spread.

Since assimilation of data will only be relevant at lengthscales comparable to or larger than the grid spacing, we need to smooth the vertical profiles (OSB and radiosounding) consequently prior to assimilation. We apply a local regression using a weighted linear least squares and a second order polynomial so that it filters out the vertical wavelengths smaller than $\sim$ 500 m. Then, the profiles are undersampled so that the vertical ratio of the number of vertical observations to the number of vertical model levels is roughly 4.

4.7.3   Description of the experiments with and without data assimilation

For each case, we conducted three experiments using WRF and DART to investigate the impact of the assimilation of very few localized observations on the forecast of Lagrangian balloon trajectories. In the first one referred to as WRF-Ens, we initialize the 50 WRF members with the EPS forecasts and run the simulations for 48 h straight as an ensemble control forecast without assimilating any data (see Figure 4.2 a)). The second experiment differs by the assimilation of a radiosounding prior to the launch of the OSB: the WRF ensemble is restarted from an update with DART. In this experiment, the model is run for a typical period of $\sim$ 24 h to allow the perturbations to grow and optimize the ensemble spread before encountering the first

observation to be assimilated. Since those perturbations are constructed to grow the most unstable dynamical modes for lead times of $\sim$ 72 h, this value of $\sim$ 24 h was found to be a good compromise between predictability, computational cost and ensemble spread. We verified that the ensemble spread after 24 h lead time was enough by computing the covariance between the observations and the WRF ensemble. Then, the radiosounding is assimilated at its mid ascent time (i.e. the time evolution during the radiosounding ascent is not taken into account). The model is run from this perturbed analysis until the OSB touches the ground. This experiment will be referred to as DART-RS. The last experiment (DART-OSB) differs from the second one by the assimilation of the subsequent OSB observations during the ascent. We only use wind and temperature data during the ascent of the OSBs in our assimilation experiments. This is equivalent to assimilating a single radiosounding $\sim$ 1h before the balloon reaches its ceiling. In contrast with experiment 2, this time the assimilation takes place at launch time to constrain the low-level flow. In operational condition, this type of setup is equivalent to a nowcasting situation. See Figures 4.2 b) and 4.2 c) for schematics of experiments 2 and 3.

4.7.4   Integration of Lagrangian trajectories

Comparison between the model outputs and the balloon trajectories is easily done by calculating Lagrangian trajectories using the Eulerian forecast flow. Trajectories usually are integrated using a smaller time step than the output period. Here, they are interpolated linearly in time to get the same time frequency as the OSBs' sampling (i.e. 10 s). The OSBs have a complex flight physics, making the prediction of their vertical position difficult a priori. In practice, interventions (gas release, ballasts drops) introduce an external element, making prediction impossible. Therefore, the Lagrangian assumption for the OSBs is not valid anymore; implementation of the flight physics and knowledge of the operator's commands would be necessary to
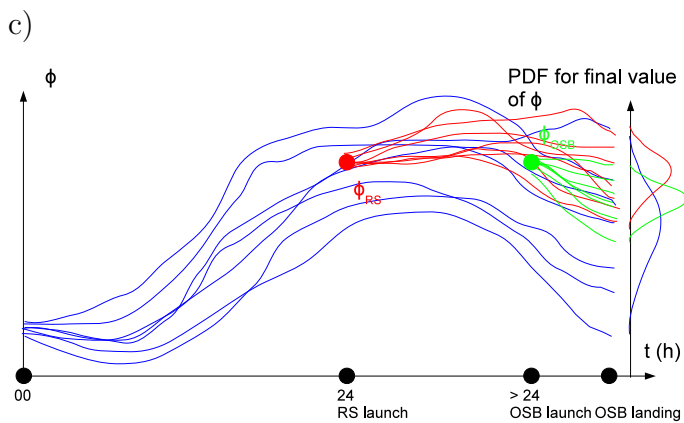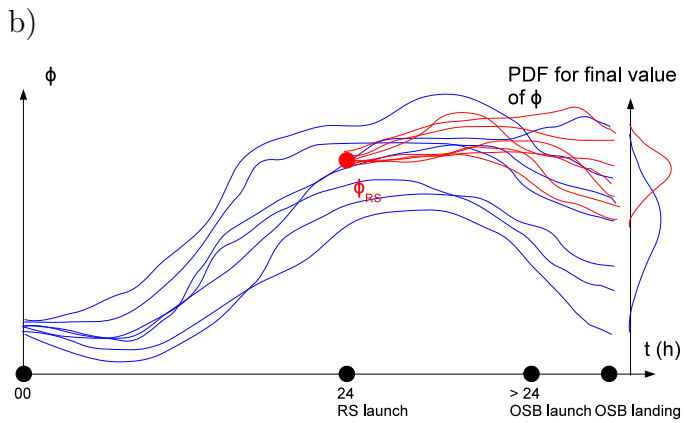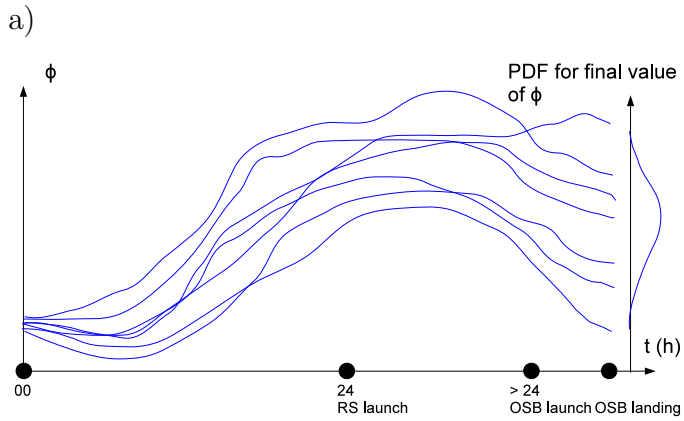
a)

b)

c)

Figure 4.2: Schematics of a) the WRF-Ens (no data assimilation), b) DART-RS (assimilation of a single radiosounding), and c) DART-OSB (assimilation of a radiosounding and the OSB's ascent) experiments for a scalar ϕ.

completely calculate trajectory forecasts (*Alexander and de La Torre*, 2003). This is beyond the scope of the present study. Hence, we chose an alternative simple solution. We prescribe the vertical level using the OSBs' altitude and only integrate the horizontal wind components using a simple forward Euler scheme. This is sufficient to investigate the uncertainty tied to the forecast of the atmospheric state (point 1 in the Introduction).

4.8   Case studies and results

In this section, three case studies are presented. For each, the WRF-Ens, DART-RS, and DART-OSB forecasts are presented and compared to the observations and the ECMWF forecasts. We focus on the ensemble means in this section.

In this study, we focus only on Flights 4, 1, and 3 that are referred to as Cases # 1, 2, and 3 respectively from now on (see the red rows in Table 4.1). Case # 1 was chosen because its root-mean square error compared to the ECMWF velocities was the highest. The second and third cases have the shortest intervals between the radiosounding and the OSB launch time.

4.8.1   Case # 1: 16 August 2009

The synoptic situation from 15, 00UTC to 17 August, 00 UTC in the ECMWF consists of a geopotential shortwave trough at mid altitude moving eastward across the Scandinavian Mountains. As depicted in Figure 4.3 a), the tropospheric westerly winds are stronger approximately 500-1000 km south of the launch site location but they are relatively weak above the launch site. At the upper levels, the launch site is located slightly north of a shear zone.

As shown in Figure 4.1a), OSB # 1 reaches a maximum altitude of $\sim$ 30 km after an ascent that lasts 1h30min. It slowly drifts at that level for about 30 min before slowly flying downward to a second lower ceiling located at $\sim$22 km that lasts

approximately 1 h. Then, the OSB descends back to the surface under parachute in less than 30 min (Fig. 4.1 a)). The trajectory of OSB # 1 is depicted in Figure 4.1d). At the beginning of its flight, the balloon first encounters a southwesterly flow and drifts of few kilometers near the surface, before moving southwestward for approximately 20 km. At the ceiling, the OSB flies through a region where u and v reverse sign for a moment and the balloon makes a small loop no wider than 10 km. Then, its trajectory inflects again toward southwest and the OSB flies 20 km until the end of the flight.

The vertical profiles of the horizontal velocity interpolated along the radiosounding (RS) position at the DART-RS analysis is shown in Figures 4.4 a) and 4.4 b) (blue curves). The WRF-Ens simulation forecasts accurately u. In contrast, v is more problematic and the surface, mid to upper troposphere and most of the flow in the stratosphere higher than 18 km are not well represented in WRF-Ens. The impact of the assimilation of the radiosounding is also represented in Figure 4.4 (red curves). It shows that the assimilation succeeds in producing a significant local increment, in particular on the v-component with increments in the range of 3-5 m s^{-1} between 5 and 10 km of altitude (Fig. 4.4 b)). On u, the correction is greater at the 10 km jet stream (Fig. 4.4 a)) where the observation error is the greatest (i.e. $\gtrsim 3$ m s^{-1}). The root-mean square error with respect to the radiosounding is slightly reduced on u and significantly reduced on v with a difference of almost 1 m s^{-1} (see Table 4.4). Note however that there remain discrepancies between the observed and analysed v between 18 and 25 km. Now, the critical region to predict the Lagrangian OSBs' trajectories is between 25-33 km on average as the balloon spends most time flying at the ceiling. The red curves fit the OSB observations closer than WRF-Ens on average in this region, although the 5 km vertical wavelengths waves are damped by the ensemble mean. The horizontal structure of the increment at the mean altitude of the balloon at the ceiling (28 km) is represented in Figure 4.4 c). The correction

Table 4.4: RMSE along the radiosounding profile at the DART-RS (upper part) and DART-OSB (lower part) analysis time for the three cases.

	Case # 1		Case # 2		Case # 3	
Experiment	RMSE(u) (m s^{-1})	RMSE(v) (m s^{-1})	RMSE(u) (m s^{-1})	RMSE(v) (m s^{-1})	RMSE(u) (m s^{-1})	RMSE(v) (m s^{-1})
WRF-Ens	2.26	2.45	2.73	3.60	3.86	2.00
DART-RS	2.10	1.57	1.73	1.36	1.90	1.29
DART-RS	3.93	3.01	3.23	4.40	3.67	2.30
DART-OSB	2.78	2.44	2.85	3.28	2.36	3.79

is largest in the center of the model domain and vanishes at the lateral boundaries because of the localization radius of 300 km. The effect on the flow is to displace the jet toward the north: a region with stronger u now embeds the launch site zone in DART-RS.

We show the vertical wind profiles interpolated along the OSB's ascent in Figure 4.5 at the DART-OSB analysis time (19UTC). DART-RS (red curve) agrees satisfactorily with the observations overall especially in stratosphere, but it fails to simulate the surface jet and it overestimates the tropospheric upper jet. In contrast, the assimilation of the OSB's ascent brings major corrections on these regions of the flow, but the analysed v still slightly overestimates the amplitude of the tropospheric jet. Let us note that DART-OSB fits the observations closer at the uppermost part of the OSB's ascent.

The trajectories integrated in WRF-Ens, DART-RS, and DART-OSB are represented along with the observed trajectory in Figure 4.6 a). The ECMWF trajectory (dashed black line) is also shown for comparison. The trajectory in the ECMWF ensemble forecast (dashed black line) sees mainly zero u and positive v-wind and drifts mostly northward during the integration period. At the end of the time integration, the distance between the OSB and the ECMWF trajectory is 90 km (Fig. 4.6 b)). In contrast, the use of the mesoscale model greatly improves the trajectory as evidenced in Figure 4.6. At the beginning, the trajectory is toward the east but is
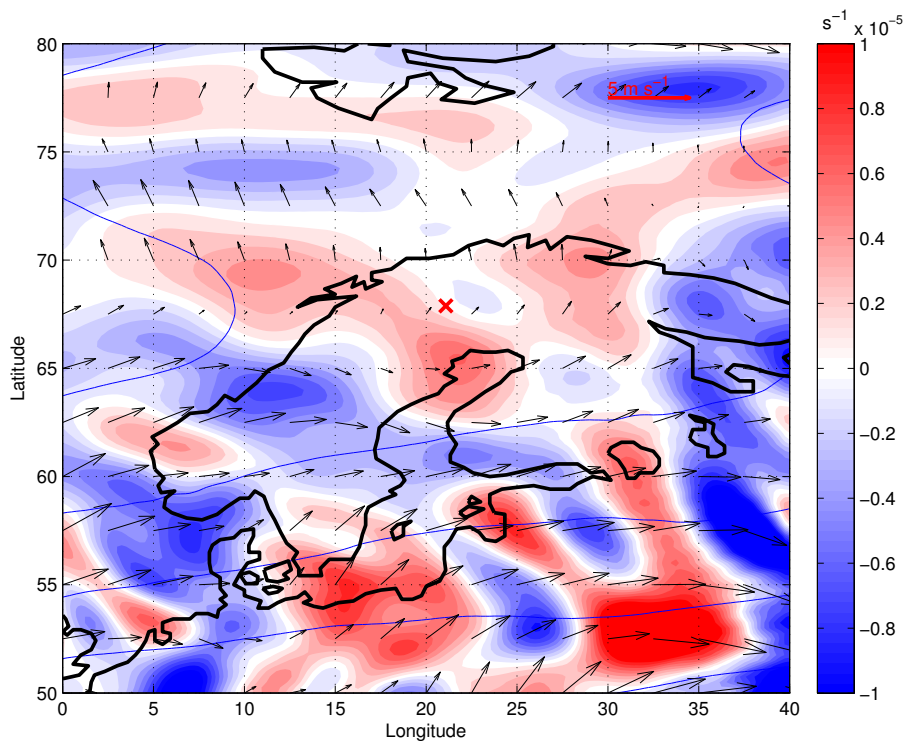
a)
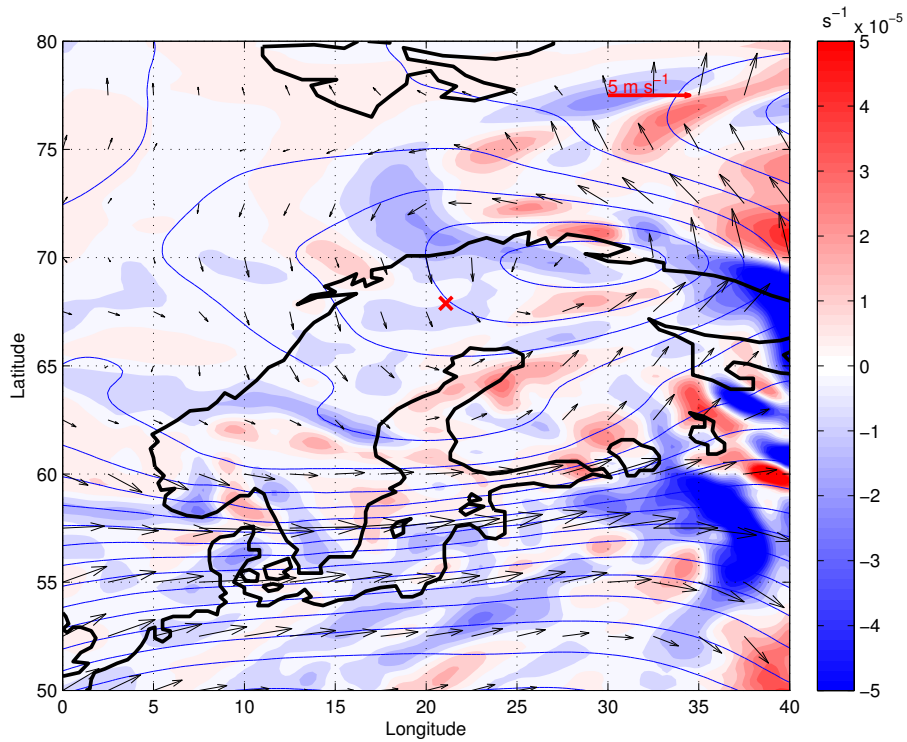
b)

Figure 4.3: Wind field (vectors), geopotential height (blue contours), and relative vorticity (shaded contours) for Case # 1 from the 24 h lead time ECMWF control forecast on 16 August 2009 at 18UTC a) at 500 hPa and b) at 50 hPa. The contour interval for the geopotential height is 25 m. The red cross denotes the launch site.

quickly corrected in the mid-upper troposphere and compensate its initial drift. The simulated trajectory at the ceiling is located approximately 5 km east of its observed location. Then, the trajectory is oriented southeasterly and the simulated landing is only 30 km away from the OSB, thus reducing the error by a factor 3 (Fig. 4.6 b)). The DART-RS trajectory is almost identical to that in WRF-Ens during the balloon ascent, then it is slightly corrected in the stratosphere and the distance is further reduced to 15 km at the end of the flight. Plots of time evolution of the difference between the DART-RS and WRF-Ens fields (not shown) provided evidence that most of the correction was quickly advected away outside of the computational domain by the westerly flow at the ceiling. This explains the similarity between the WRF-Ens and DART-RS trajectories. In the DART-OSB experiment, the balloon is seen to fly in the southeast direction immediately after take-off, and it reaches ceiling almost at the same location as the OSB. The balloon drifts further south than in WRF-Ens/DART-OSB and lands only $\sim$ 5 km from the OSB. DART-OSB reproduces the slight inflection toward the east in the trajectory during the descent (also present in DART-RS but not in WRF-Ens). Overall, the error has been reduced with a factor 18 in this case study for the final time. We note however that all the experiments miss the initial inflection in the trajectory at the ceiling present in the observations. We have evidence in Figure 4.5 that this is because the ensemble mean significantly damps the short vertical wavelength wave between 28-30 km of altitude. Therefore, the computed trajectory does not see this gradient when the balloon slowly decreases in altitude during the ceiling phase. The impact of the vertical structure will be discussed in Section 4.9.

4.8.2 Case # 2: 02 August 2009

The meteorological situation between August 01, 00UTC and 03, 00 UTC as seen in the ECMWF control forecast is characterized by a high-geopotential zone at
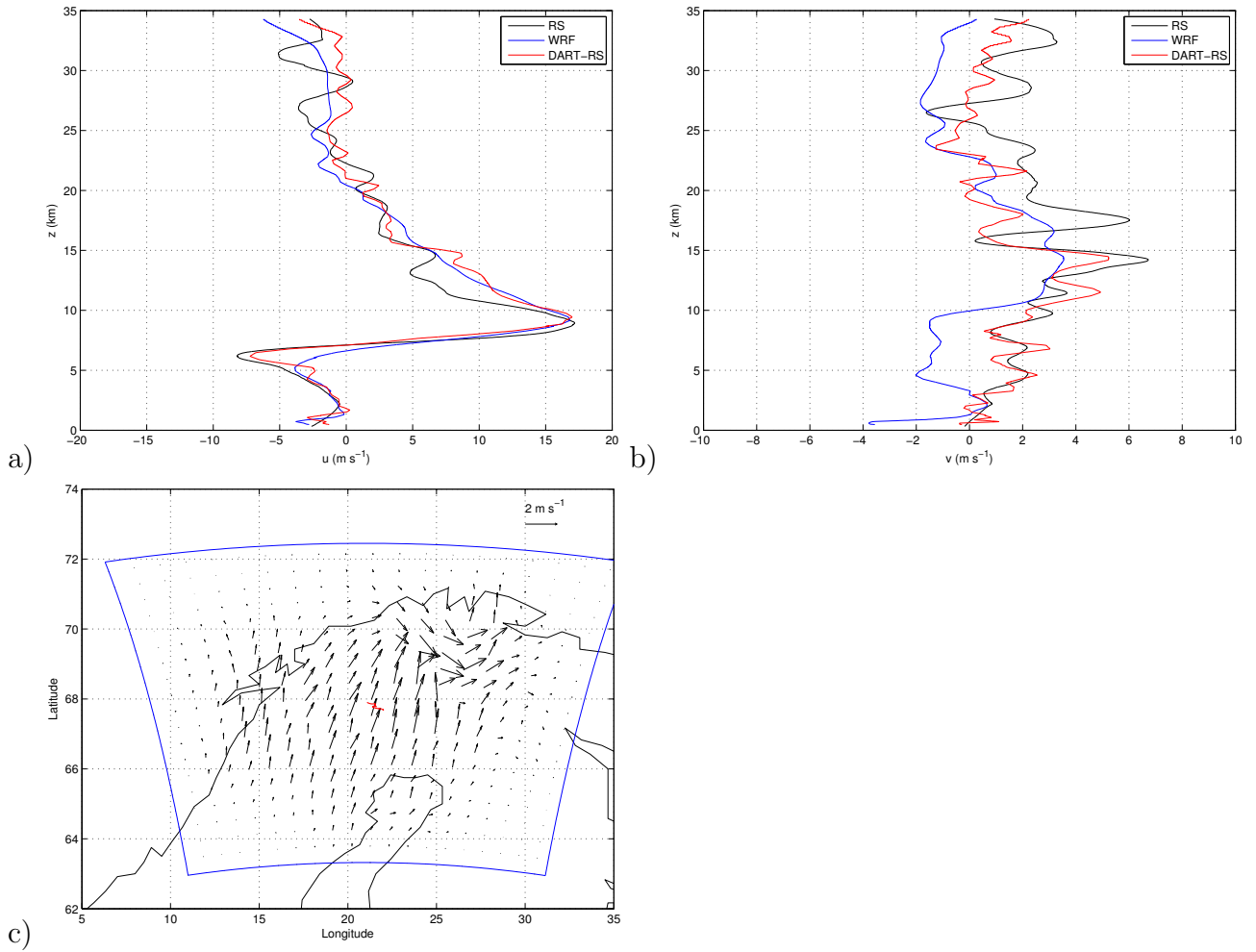
Figure 4.4: Vertical profiles for Case # 1 of a) the zonal and b) meridional wind components at DART analysis time (07UTC). c) Vector field of the horizontal velocity increment at $z = 28$ km for Case # 1. The OSB trajectory is represented as a red solid line, and the blue line denotes the boundaries of the model domain.
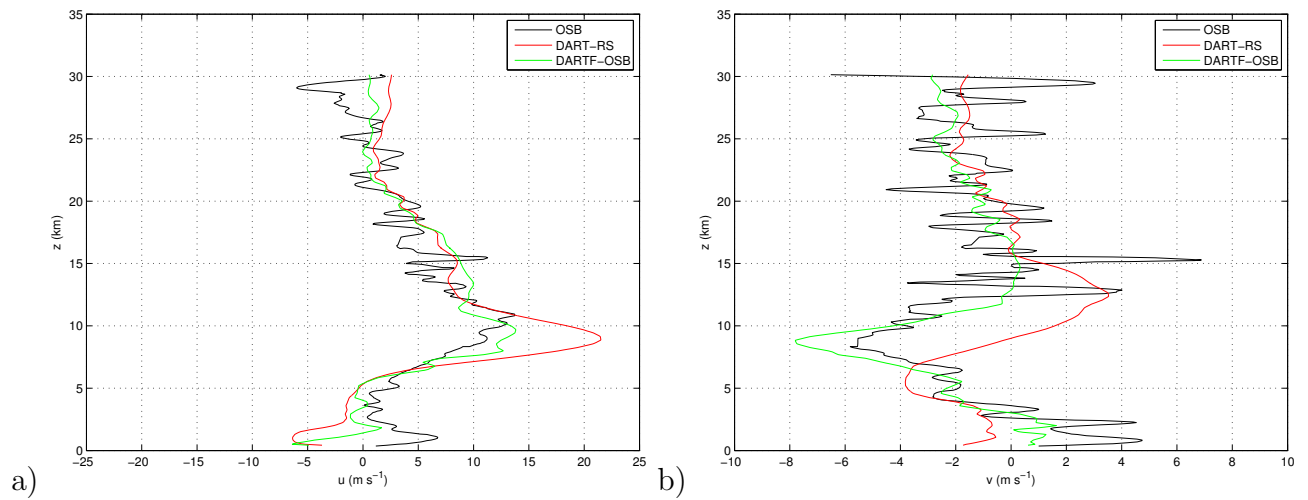
Figure 4.5: As in Figure 4.4, except at DART-OSB analysis time (19UTC).
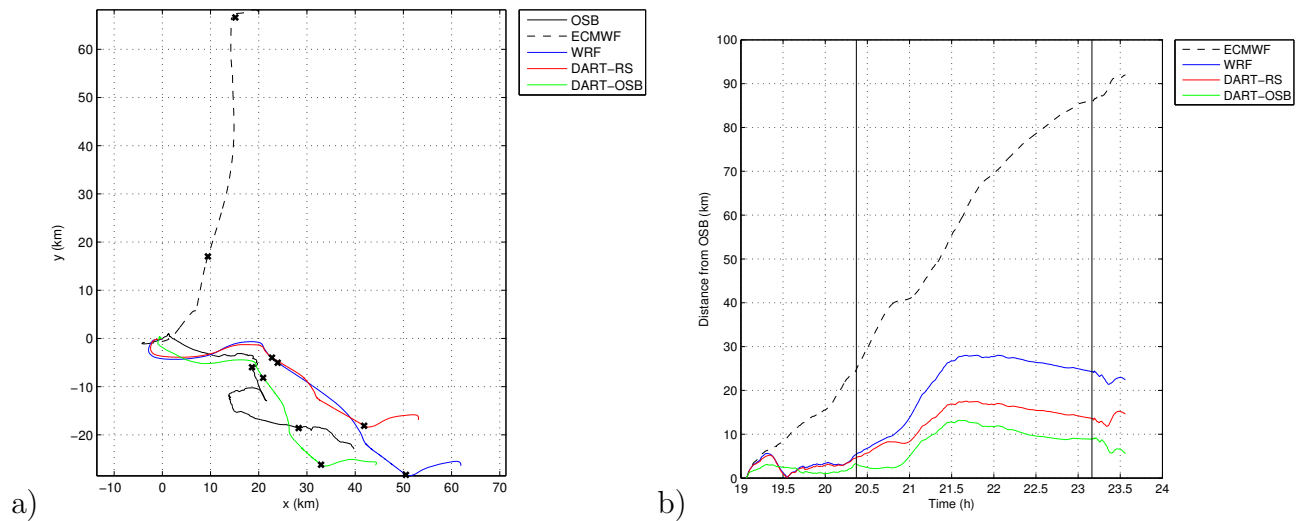
Figure 4.6: a) Trajectories for Case # 1 integrated from the surface, using the vertical position of the OSB. The black dots correspond to the start and end of the ceiling. b) Distance between the numerically integrated and the observed OSB trajectories for Case # 1. The solid black lines correspond to the start and end of the ceiling.

102

a)
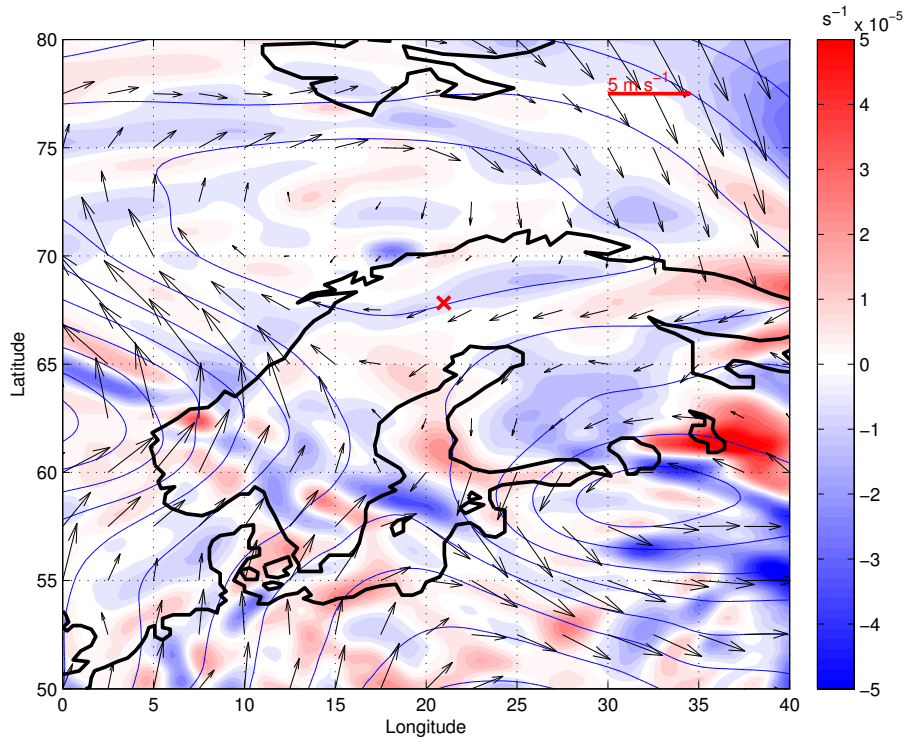
b)
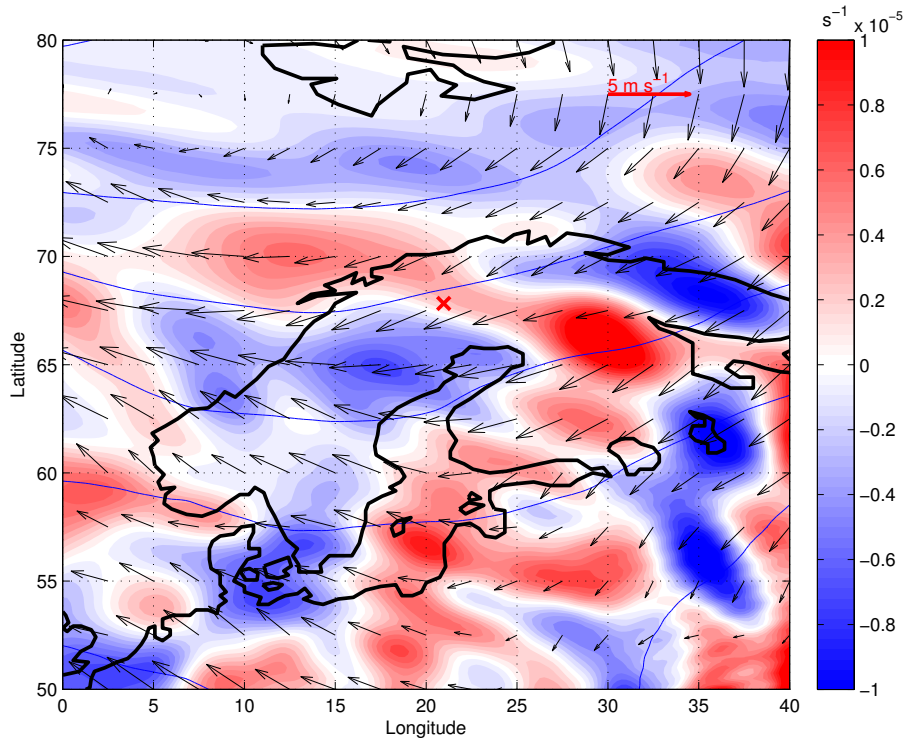
Figure 4.7: As in Figure 4.3, except for Case # 2 the 02 August 2009 at 18UTC.

103
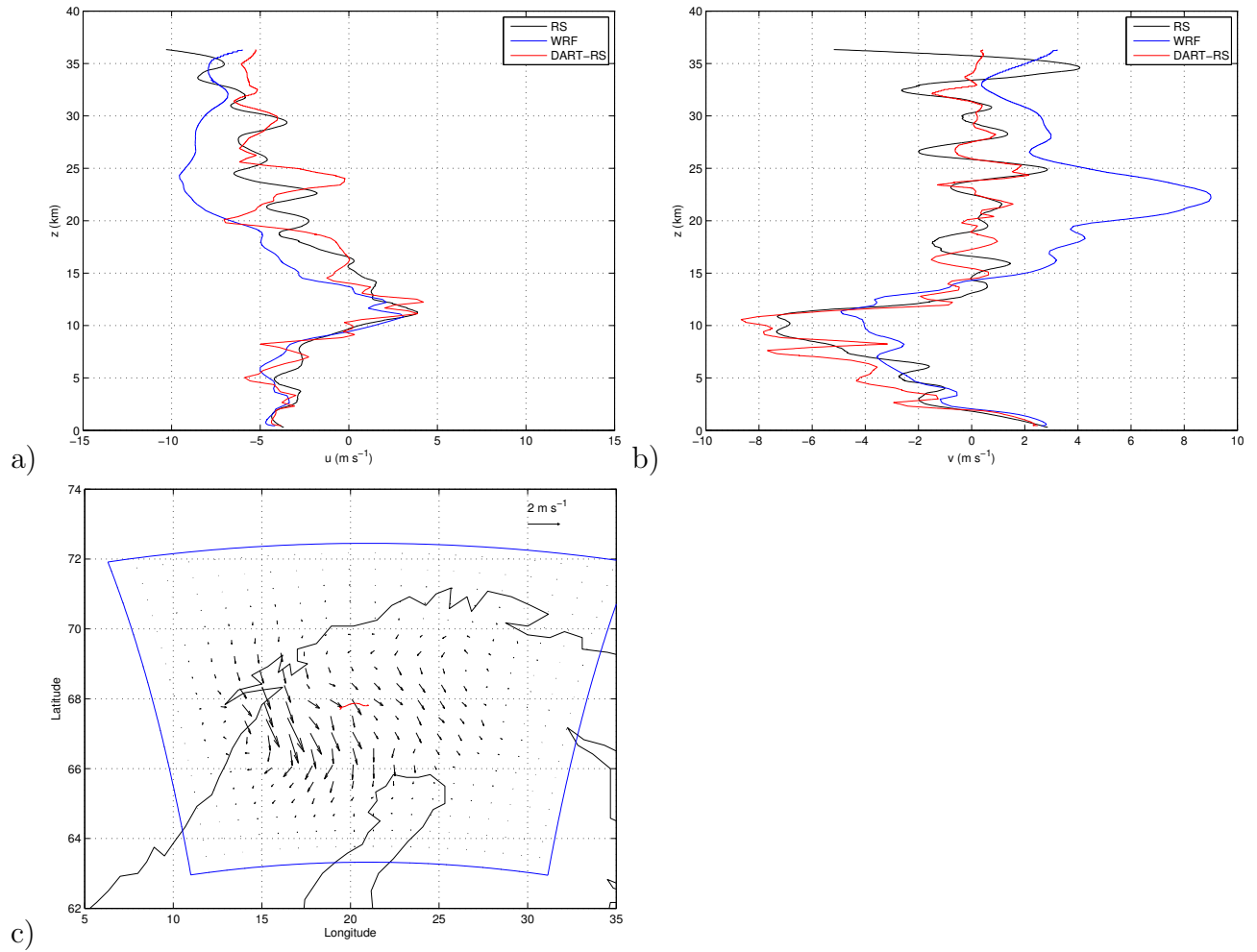
Figure 4.8: As in Figure 4.4, except for Case # 2 the 02 August 2009 at 15UTC.
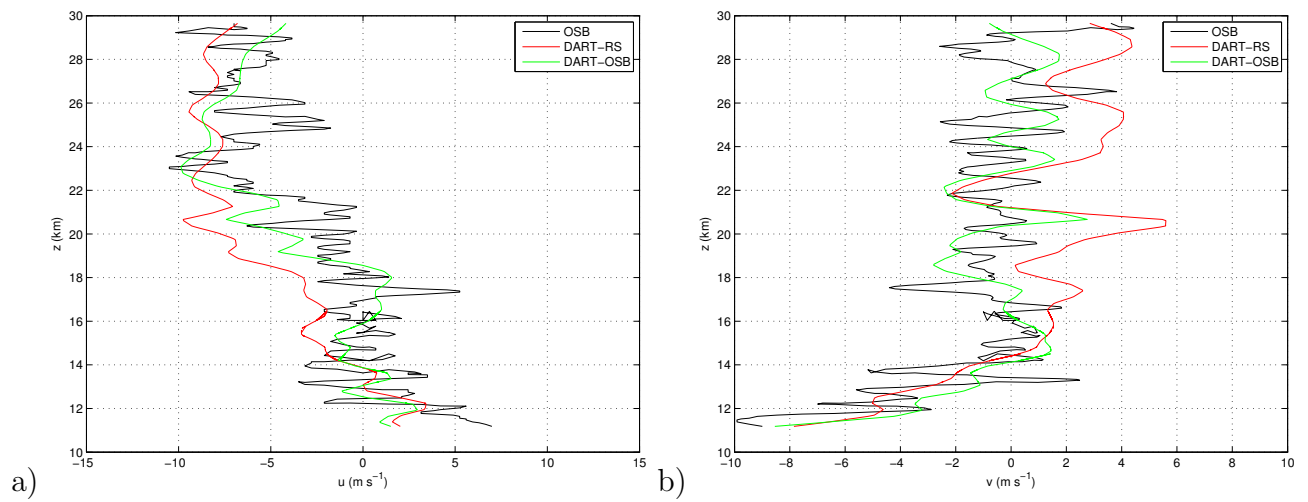
Figure 4.9: As in Figure 4.5, except for Case # 2 the 02 August 2009 at 18UTC.

500 hPa over the northwest of the Scandinavian Mountains that surrounds the OSB's launch site (Fig. 4.7 a)). At mid-levels, the wind is mostly easterly when converging toward the Scandinavian Mountains, and relatively weak over Kiruna. At 50 hPa, the flow has a dominant large scale component that is mainly easterly with typical values of 2 m s^{-1} over the region of interest (see Fig. 4.7 b)).

The data from OSB # 2 starts at ∼11 km of altitude as shown in Figure 4.1 b). The balloon's ascent lasts approximately 1h30min and reaches maximum altitude of approximately 30 km at the ceiling and then flies down slowly for 2h to 28 km, before the instruments detach from the balloon and fall under parachute in 30 min. In contrast with Case 2, there is only one long ceiling in this flight. The trajectory is depicted in Figure 4.1e). The balloon initially moves southward for less than 5 km then turns east for approximately 10 km. After reaching its ceiling, the balloon drifts slowly northwestward for a few kilometers, then purely westward, then southwestward for about 40 km. After detaching itself from the balloon, the gondola makes a small loop when going down through the troposphere.

The assimilation of the radiosounding at 15UTC produces local significant increments on the both components of the wind (Fig. 4.8). Apart from the increase of the amplitude of the 10 km jet on v, most of the correction is effective in the stratosphere with increments that reach as much as 8 m s^{-1} at 23 km. The RMSE is reduced by 1 m s^{-1} (37%) on u and more than 2 m s^{-1} (62%) on v (Fig. 4.4). At 28 km of altitude we have represented the horizontal cross section of the increment in Figure 4.8 c). The correction is maximum downstream of the OSB launch site and right over the Scandinavian Mountains. The assimilation reduces the northward and westward components of the wind. We show the vertical profiles of the velocity at the DART-OSB analysis time at 18UTC in Figure 4.9. Note once again here that for Case # 2, the OSB starts transmitting the data after it reaches the altitude of 11 km (see Figures 4.1 b) and 4.9), and therefore the surface flow in DART-OSB does

not benefit much from the assimilation of the OSB's wind. The DART-RS profiles overestimate the magnitude of the wind at altitudes higher than 10 km. DART-OSB provides a significant correction on the wind profiles with local increments of 2-3 m s^{-1}, but DART-RS is closer to the observations at the uppermost point of the OSB's ascent. The RMSE on the velocity components after assimilation of the OSB is reduced typically by 1 m s^{-1} (10-25%).

The integrated trajectories show a smoother structure than the observations (Fig. 4.10). The OSB initially drifts toward the west-northwest, then the wind progressively changes in direction at the ceiling from easterly to east-southeasterly. The ECMWF ensemble mean consists of a northwestward trajectory where the balloon touch down is located 90 km away from the real trajectory. Each successive correction (WRF-Ens, DART-RS, DART-OSB) progressively reduces the angle with the observed trajectory, but all the simulated trajectories miss the inflection at the ceiling seen in the observations. This results from the fact that during its slow descent at the ceiling, the model fails to simulate the same vertical structure as in the observations, and thus the balloon does not see the sharp gradient on v between 28-30 km (Fig. 4.9 b)). The wave is absent from the ensemble mean but also from most of each individual member. In order to determine whether this wave near the ceiling is an inertia-gravity wave (IGW), we have represented the hodograph of the disturbance velocities in Figure 4.11 (*Plougonven and Teitelbaum*, 2003). The hodograph shows an horizontally oriented ellipse with an aspect ratio close to 0.5, suggesting an IGW with an intrinsic frequency of $2f$. The anticyclonic rotation of the hodograph reveals that the enery is propagating upward. We note that there is no significant differences between the DART-RS and DART-OSB trajectories in this case study. Those results, and the fact that the OSB launch site is located in the lee of the (southward) wind suggest that this wave is likely to be an IGW. Assuming that this wave has a persistence of only a several hours, it will be present during the ascent but not during

106

the descent. Thus, the OSB sees the phase of the wave during the ascent, but the deviation is not compensated while going downward a few hours later. Although the integrated trajectories after assimilation do not agree with the observations as well as in Case # 1, the error distance has been reduced by a factor 2 (i.e. the final error is 40 km).
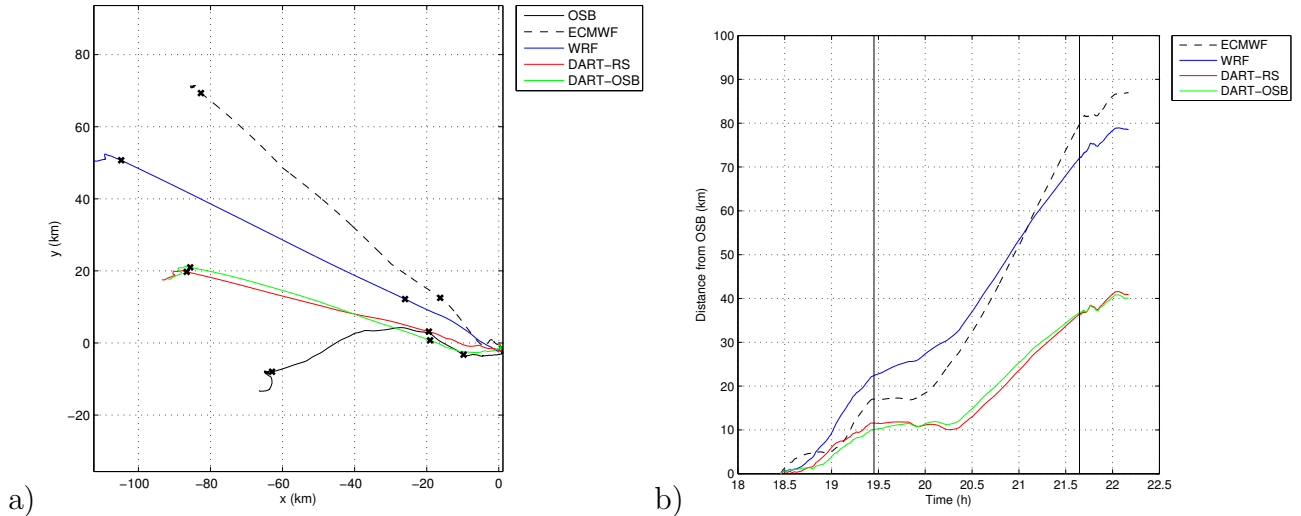
Figure 4.10: As in Figure 4.6, except for Case # 2.

4.8.3   Case # 3: 14 August 2009

On 14 August 2009, the flow at 500 hPa shows a large synoptic cyclone located northwest of the Scandinavian Mountains and the shore and a shortwave trough over most of Scandinavia (Fig. 4.12 a)). The launch site is located in the eastern quadrant of the low pressure system, in a region where the winds are mostly oriented toward north-northeast. In the stratosphere, the flow shows a left exit jet region with relatively weak winds oriented towards the north at 67°N over the OSB launch site and Cape North (Fig. 4.12 b)).

The altitude time series for OSB # 3 is shown in Figure 4.1 c). This time, data starts from the surface as in Case # 1. This balloon reaches the highest altitudes
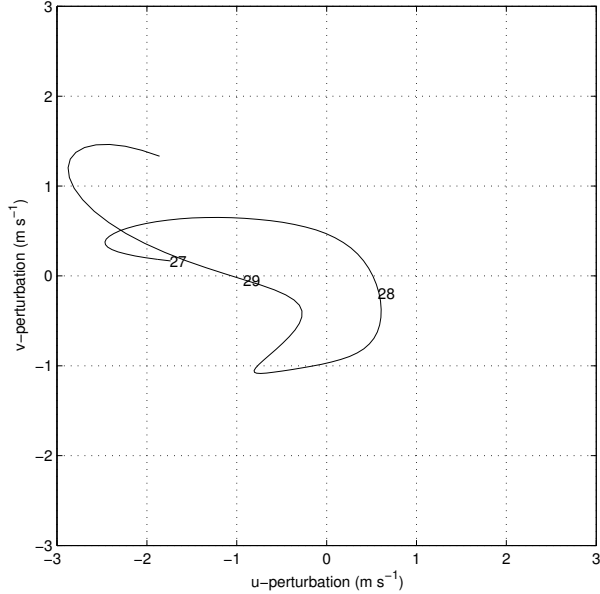
Figure 4.11: Hodograph for OSB # 2 in the height interval 27-30 km, from the velocity disturbances obtained by filtering out the scales larger than 5 km and shorter than 300 m. The numbers indicate the altitude in km.

and flies at almost constant altitude of ∼33 km throughout its ceiling that lasts approximately 2 h. We show the OSB's trajectory in Figure 4.1f). The balloon takes off with an initial northward component for approximately 20 km. Then, it turns west at the ceiling in the low wind zone before turning north again and drifting for a few tens of kilometers.

The results of the assimilation of the radiosoundings are shown in Figure 4.13. Overall, WRF-Ens is very similar to RS below 20 km. Above this altitude, WRF-Ens overestimates the wind magnitude. The correction provided by DART-RS is greater in this region of the flow. The RMSE is reduced almost by half on both components of the wind (see Table 4.4). The horizontal structure of the increment at 28 km is a zonal dipole that is centered on the OSB launch site as evidenced in Figure 4.13 c). This increment suggests that the EnKF used the observations to correct the position of the background forecast cyclone and move it to the west. At the DART-OSB analysis time, the error is greater in the mid-troposphere on u and v and above

25 km in DART-RS above 25 km on v as we see in Figure 4.14. The correction in DART-OSB on u in the stratosphere agrees overall with the observation but fails to retrieve the waves present in the upper part of the trajectory. For v, the assimilation even degrades the results starting at 10 km of altitude, and the RMSE increases of more than 1 m s^{-1} (39%) as we see in Table 4.4.

The resulting integrated trajectories are represented in Figure 4.15. The real OSB initially flies northward then deviates slightly to the west when it reaches the ceiling before drifting with an almost pure northward component. ECMWF is the only trajectory that manages to reproduce that northward extension, but it overestimates the westward motions of the balloon. Thus, it predicts its touchdown point 80 km away from that of the OSB (Fig. 4.15 b)). The trajectory forecasts by WRF-Ens and DART-RS show the initial northward drift, but they both inflect at the ceiling and move back toward the south. Here, those two experiments do not reduce the error distance significantly (10 km at final time relative to ECMWF). DART-OSB does not simulate the southward drift seen in WRF-Ens and DART-RS but it stills fails to reproduce the northward extension of the OSB, although the error distance is reduced by half compared to ECMWF. Those results suggest a bifurcation of the trajectory within the complex horizontal velocity gradient seen in Figure 4.12. The sensitivity of the integrated trajectories to the location of the OSB's ceiling initial point will be discussed in Section 4.9.

4.9 Summary and discussion

We have investigated the prediction of three Open Stratospheric Balloons trajectories during the Strapolété summer Campaign in Sweden in 2009. For these predictions we have examined the impact of using 1) ensemble simulations with the mesoscale model WRF, 2) assimilation of a single available radiosounding in WRF using DART, and 3) assimilation of both the radiosounding and additional data from

a)
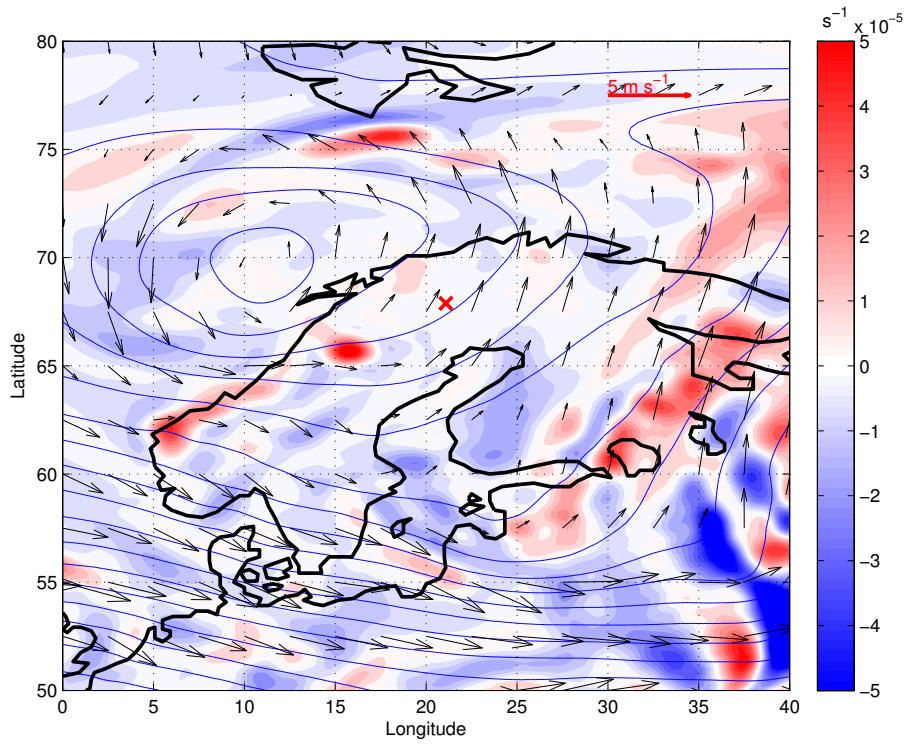
b)
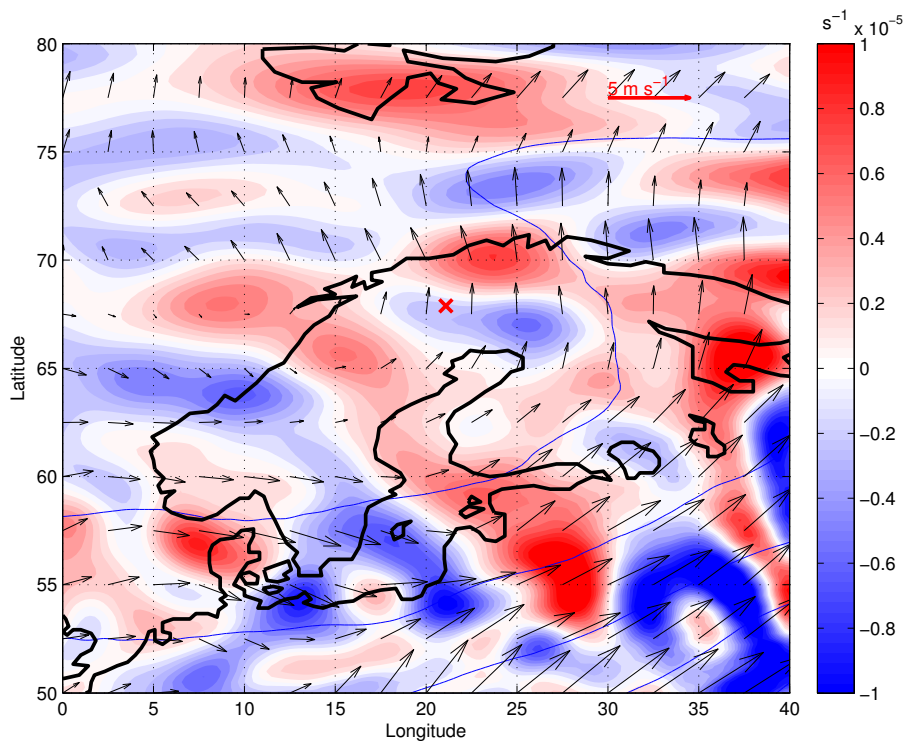
Figure 4.12: As in Figure 4.3, except for Case # 3 the 14 August 2009 at 12UTC.
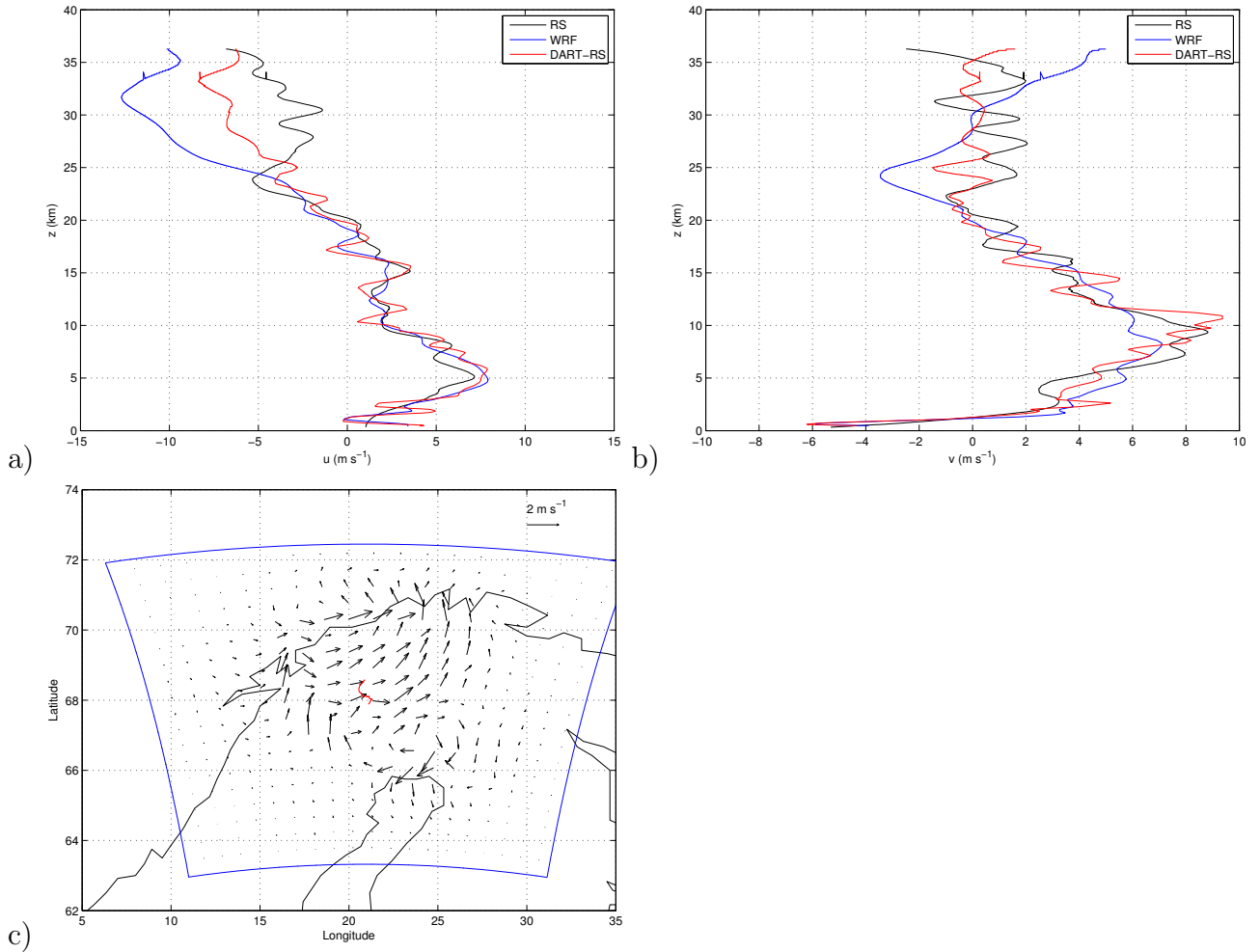
Figure 4.13: As in Figure 4.4, except for Case # 3 the 14 August 2009 at 03UTC.

ascending OSB.

On its own, the use of a mesoscale model (WRF) already has a significant potential for improving the trajectory forecasts. This is illustrated by Case # 1, where the final position of the trajectory in WRF-Ens is 70 km (relative to the OSB) better than the ECMWF trajectory. However, this improvement is not systematic as demonstrated in Cases #2 and #3, for which the forecast final position of the position are only 10-15 km better than the ECMWF relative to the OSB. There are two aspects that explain the benefit of the WRF-Ens over the ECMWF in general:

1. Using WRF allows us to tackle the limitations in terms of resolution and output
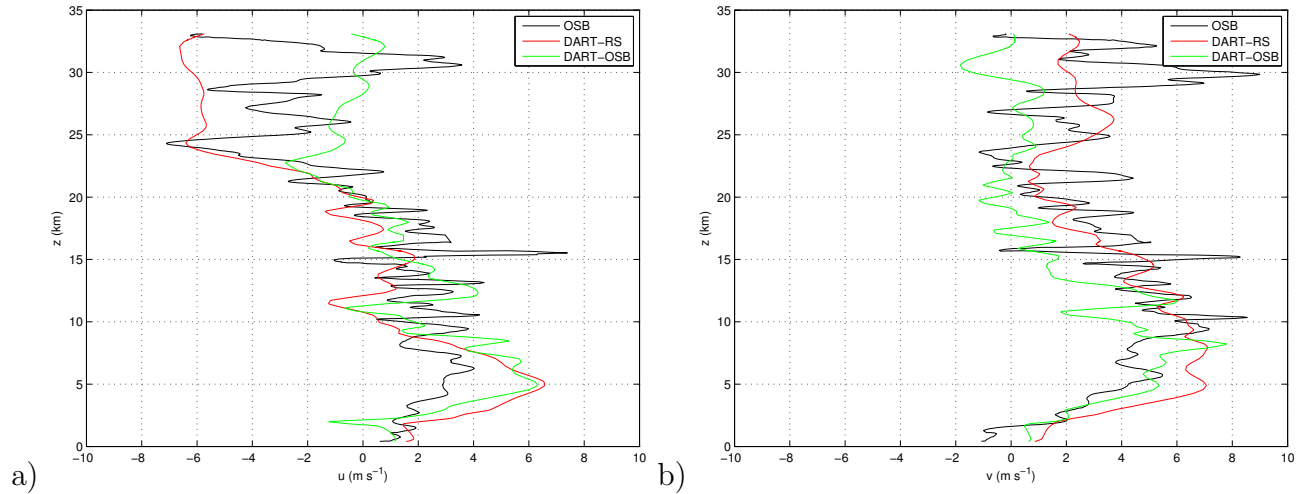
Figure 4.14: As in Figure 4.5, except for Case # 3 the 14 August 2009 at 10UTC.
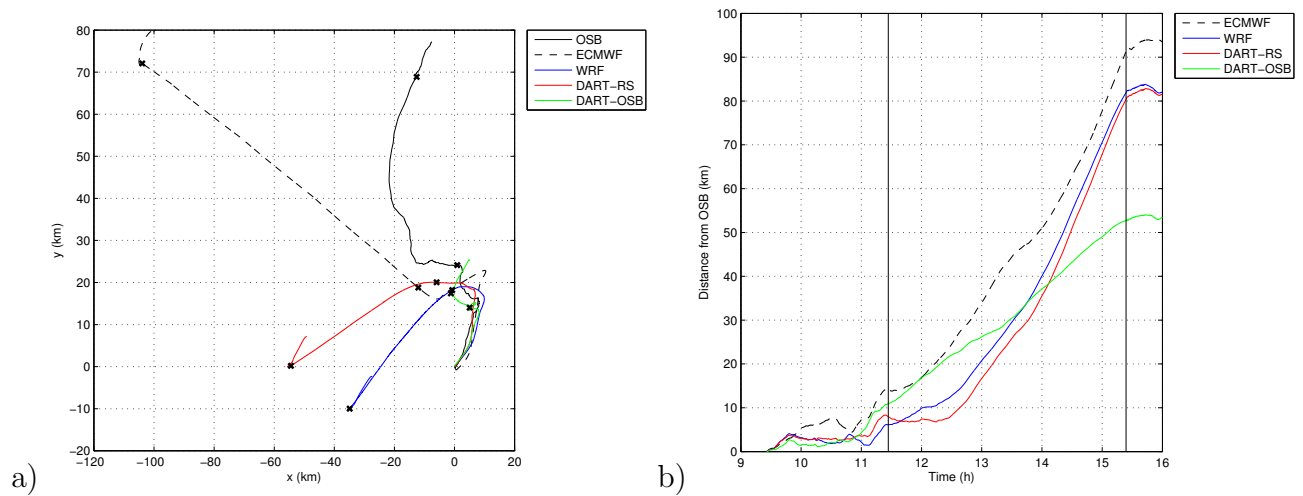
Figure 4.15: As in Figure 4.6, except for Case # 3.

frequency (*Walmsley and Mailhot*, 1983). The ECMWF model has a typical horizontal resolution on the order of ∼10-20 km, therefore it is not able to simulate correctly the forcing that the balloon experiences at scales on the order of ∼1-10 km due to scale truncation (*Kahl and Samson*, 1986). In our case, the increase of resolution in our WRF simulations (10 km) is enough to resolve parts of the complex orographic flow near the Scandinavian Mountains but vertical resolution is too coarse to simulate short vertical waves as evidenced

in Case # 2. *Kuo et al.* (1985) and *Knudsen and Carver* (1994) also showed that sparse time resolution (6h for the ECMWF) is also likely to affect computed trajectories because it is too coarse to identify the local accelerations of the flow. Although the increase in spatial and temporal resolution has positive impacts, we have not examined further the sensitivity of the simulated trajectories to spatial and time resolution and cannot say what optimal resolutions would be.

2. The mesoscale model WRF is not subject to the same physical limitations as the ECMWF. For example, the ECMWF model is subject to the hydrostatic approximation, therefore it fails at representing nonhydrostatic flow features, in contrast with WRF. However, WRF still suffers from physical approximations and limitations. For instance, tests with different model top heights underline the importance of having a top as high as possible for prediction of the flow in the stratosphere. Indeed, we used model tops located approximately at ∼33 km in our preliminary experiences (compared to ≲40 km now), causing the ceiling of the OSBs to be in the sponge layer. This proved to be detrimental to the accuracy of the forecast trajectories with an increase of the error by 20% relative to ECMWF for the location of the final position for case # 3. Although it is unclear how the sponge layer impacts the trajectories, it seems logical for stratospheric simulations to use a top as high as possible.

On the other hand, Cases # 2 and #3 suggest that the main limitation with the use of WRF is that the initial and boundary conditions provided by the ECMWF are not always sufficient to represent the real atmospheric state accurately (*Knudsen et al.*, 2001). Hence, the use of additional available observational data is justified.

Using standard values for the observational errors, assimilation of only one single radiosounding produces significant local horizontal and vertical increments on the wind velocity with typical values of ∼1 m s^{-1} or more, and the root-mean square error

is significantly reduced. The resulting simulated trajectories are 10-40 km better for the final position than those calculated in WRF-Ens. Assimilation of the OSB's ascent also produces significant increments, and the trajectories are generally improved as we see in Cases $\#$ 1 and $\#$ 2, although this is not systematic (Case $\#$ 3). In order to identify the problematic parts of the trajectory, we have represented the trajectories integrated from the start of the ceiling and the descent in Figure 4.16. Most of the error adds up in the ceiling part (left panel) of the trajectory. Although this seems logical because the ceiling accounts for 50-70% of the whole trajectories, this may also seem surprising because one may expect the stratospheric flow to be dominated by the large scale balanced flow, which is well observed and constrained from satellite observations of temperature. Our case studies suggest that the trajectories can be strongly influenced by wind oscillations having short vertical wavelengths (2-4 km). These are presumably inertia gravity waves, with amplitudes of several m s^{-1}. In the few hours of a balloon's ceiling, a balloon experiences and is advected only by one phase of the wave. Forecasting such components of the flow accurately (right characteristics and phase) will remain a challenge unless significantly more observations are available. The descent phase on the other hand, which is crucial for the operations, greatly benefits from the successive assimilations of available data (Fig. 4.16 (right panel)).

In the present study, we have analyzed three cases that are very different and for which the forecast trajectories were different. This suggests that predictability is not the same for different types of flows. Estimating this predictability is important for the operations, and the spread of the ensemble gives this information. We have represented the spread of the trajectories in Figure 4.17. Case #1 is the most predictible case with the OSB trajectory embedded in the DART-OSB ensemble trajectories and the root-mean square final distance (RMSD) of 12 km (see Table 4.5). In contrast, the real trajectory is not captured well by the ensemble trajectories in Case $\#$ 2

114

Table 4.5: Root mean square distance of the DART-OSB ensemble for the final position.

	Case # 1	Case # 2	Case # 3
RMSD (km)	12.0	40.9	69.2

(Fig. 4.17b)), although the dominant eastward component is simulated correctly. The RMSD for this case is 70% larger than for Case # 1, suggesting a weaker predictability. Case #3 (Fig. 4.17c)) is representative of a bifurcation situation where the spread is almost distributed uniformely in all directions. The RMSD for this case is the highest with a value of approximately 69 km (Table 4.5). Those results suggest that the ensemble generated using the ECMWF is not ideal for short-term prediction of balloon trajectories. It might become necessary to propagate the ECMWF perturbations for a longer time. This may remain problematic in terms of computational need for the operations. It is challenging in short-term applications to construct an initial set of perturbations that samples the PDF of the possible atmospheric states reasonably (*Snyder and Zhang*, 2003; *Zhang et al.*, 2004). Methods for quickly generating the perturbations used for short-term convective/mesoscale prediction such as additive noise (*Tong and Xue*, 2005; *Dowell and Wicker*, 2008) may be appropriate here. Improving the ensemble is a path for future investigation, but this remains beyond the scope of our study. The forecast trajectories are also sensitive to the tuning of the EnKF system such as the localization radius, and the inflation. For instance, we have chosen a radius of 300 km but this is not clear that the radiosounding data correlates for more than 100 km close to fronts. Also, we have used adaptative covariance inflation described by *Anderson* (2009) but inflation has given mixed results for convective studies (*Snyder and Zhang*, 2003; *Dowell et al.*, 2004; *Tong and Xue*, 2005). Since the largest portion of the OSBs' flights remain in the stratosphere, this is not clear how this would impact their trajectories. In future studies, sensitivity to those parameters could be examined.
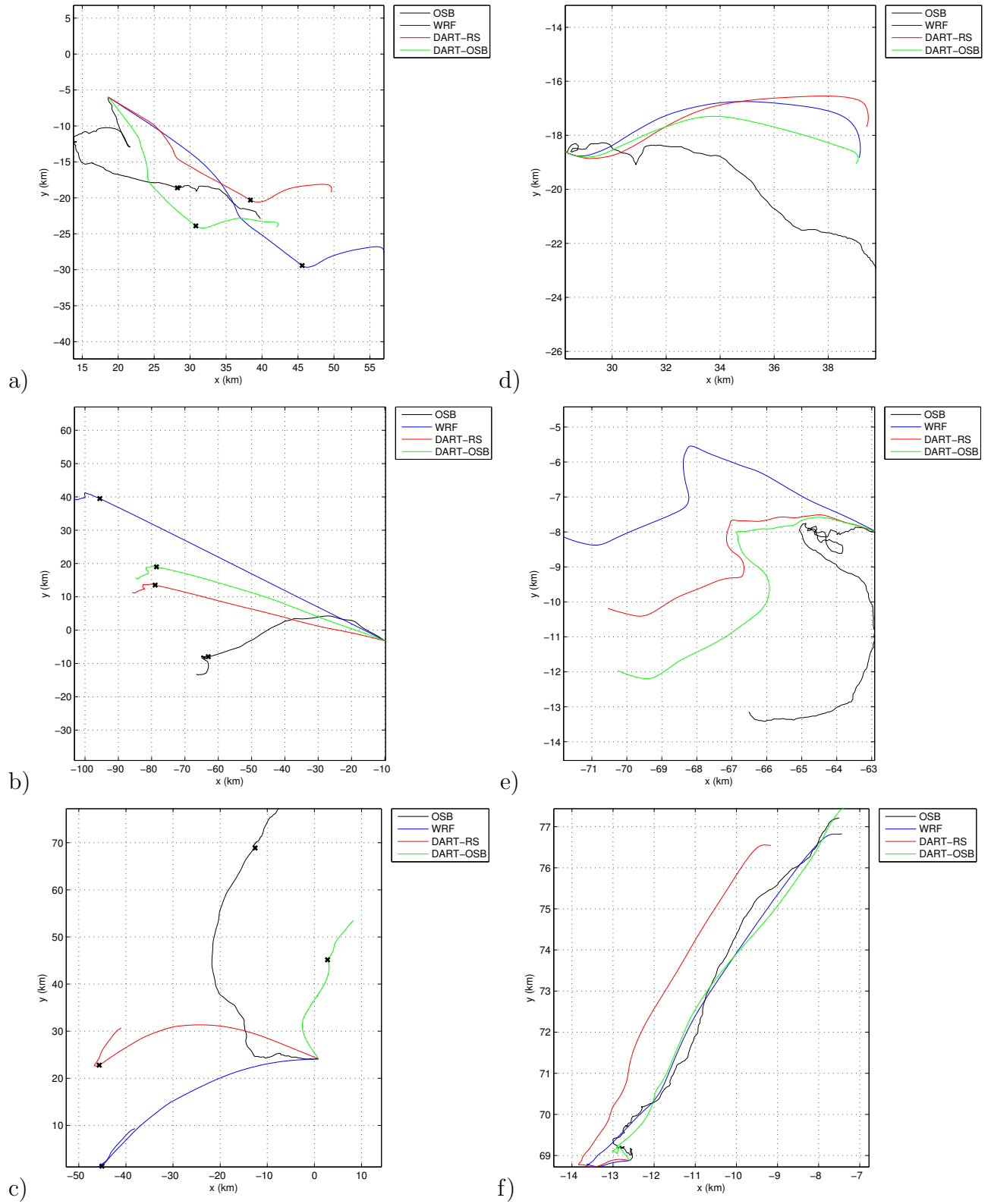
Figure 4.16: Trajectories integrated from the ceiling start (left panel) and end (right panel).

116
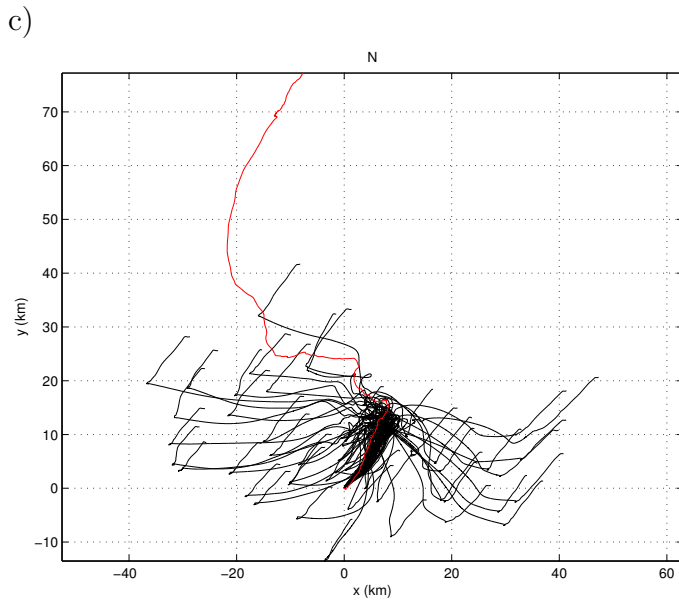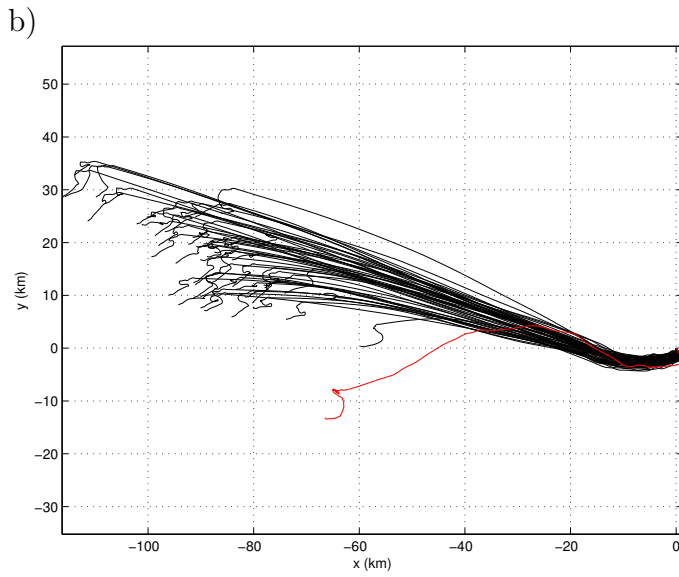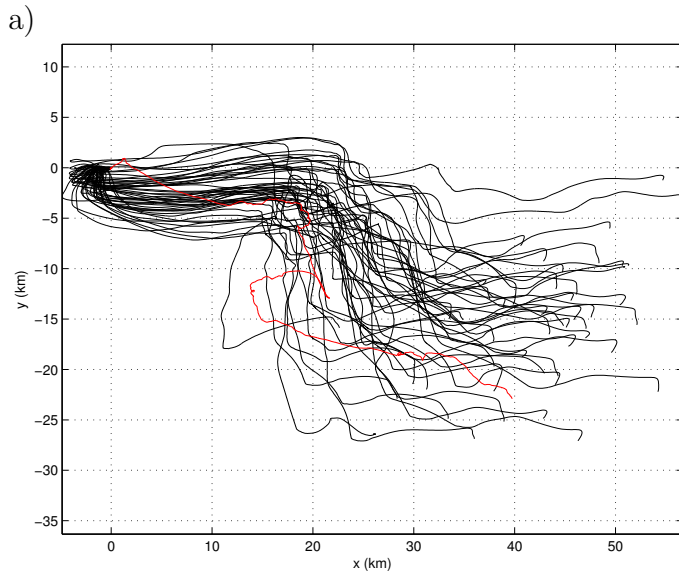
Figure 4.17: Numerically integrated trajectories in each DART-OSB member (black
lines) for Cases a) # 1, b) # 2, and c) # 3. The red lines depict the
OSBs' real trajectories.

4.10   Acknowledgements

4.11 Perspectives

Nos recherches s'appuient de manière essentielle sur les observations faites par ballon et nécessitent pour cela une étroite collaboration avec le CNES. En pratique, la mise en oeuvre de campagnes d'observation rencontre des exigences toujours plus contraignantes sur la sécurité. Le CNES a besoin de savoir estimer la probabilité d'un accident grave lors de l'atterrissage des ballons, notamment pour les OSBs dont les charges utiles peuvent peser une tonne. La prévision de la trajectoire des ballons est un élément crucial dans la démarche visant à maîtriser les risques lors des campagnes ballons. C'est par ailleurs une thématique qui a son intérêt scientifique (voir *Podglajen et al.* (2014)). Dans le présent chapitre, notre étude est porteuse d'un message positif pour améliorer les prévisions des trajectoires des OSBs au moyen de simulations à méso-échelle et en assimilant des données supplémentaires avec une méthode EnKF. Néanmoins, nous avons vu qu'il y a encore des incertitudes selon les scénarios qui proviennent des limitations décrites en conclusion dans notre analyse. Le travail supplémentaire pour améliorer encore davantage les prévisions passe par un travail sur les perturbations de l'ensemble. Dans un second temps, il peut être utile d'examiner la sensibilité des trajectoires simulées à la résolution horizontale et verticale, et au réglage des paramètres de DART. Afin de tirer des conclusions plus définitives sur l'impact des simulations à haute résolution et de l'assimilation de données, il est aussi nécessaire de faire des expériences sur un plus grand nombre de vols d'OSB. Comme les ballons volent relativement haut ($\sim$30 km), l'influence de la hauteur du toit a un fort impact sur les prévisions. Cependant, augmenter le sommet du modèle reste simple à faire. En revanche, une difficulté fondamentale subsiste pour décrire les oscillations comme celles observées entre 28 et 30 km dans les deux derniers cas, et qui influent beaucoup sur la trajectoire au plafond. L'assimilation d'observations supplémentaires (un profileur de vent est présent à Esrange notamment) permettrait

de réduire ce problème.

CHAPTER V

Conclusion

La motivation principale de ce travail de thèse est d'obtenir une meilleure connaissance des ondes de gravité dans l'atmosphère. Ceci est nécessaire afin d'améliorer la simulation de l'écoulement en stratosphère par les modèles (*Fritts and Alexander*, 2003; *Butchart et al.*, 2010). Notre approche, combinant des observations originales (balloons pressurisés; SPB) et sorties de modèles (simulations à méso-échelle avec WRF, analyses de l'ECMWF), s'inscrit dans les efforts récents pour quantifier les ondes de gravité atmosphériques, leurs flux moyens et leur variabilité (*Alexander et al.*, 2010). Nous disposons, grâce aux campagnes ballons auxquelles l'équipe a contribué ces dernières années, d'une base de donnée unique pour l'étude des ondes de gravité en basse stratosphère. En effet, un des moyens est par l'obtention de mesures in-situ faites par ballons pressurisés (SPB). En raison de leur caractéristiques (advection quasi-lagrangienne) qui permettent d'obtenir l'ensemble de caractéristiques des ondes, les SPB constituent l'une des meilleures plateformes pour l'étude des ondes de gravité, et les flux de quantité de mouvement calculés à partir de mesures SPB sont considérées à l'heure actuelle comme les estimations les plus fiables. En complément de ces observations, dont l'échantillonnage demeure inévitablement limité, les sorties de modèle permettent d'obtenir une description complète de l'écoulement avec une plus grande couverture spatiale et temporelle.

Nous avons exploité les observations des ballons lancés lors de PreConcordiasi (3 ballons, tropiques, février-mai 2010) et de Concordiasi (19 ballons, Antarctique, septembre 2010-janvier 2011). Une amélioration majeure par rapport aux campagnes précédentes (par exemple Vorcore, Antarctique, septembre 2005-février 2006) a été la résolution temporelle des mesures (toutes les 30 s au lieu de toutes les 15 min), ce qui a permis de résoudre pour la première fois la totalité du spectre des ondes de gravité. En nous appuyant sur ce jeu de données, nous avons analysé les ondes de gravité et le réalisme de sorties modèles aux basses et aux hautes latitudes.

Dans la première partie de l'étude, nous avons examiné les ondes émises par un cyclone tropical en développement. Nous avons observé un bon accord entre données ballons et simulations et montré l'importance des ondes avec des longueurs d'ondes courtes (<15 km) et avec des petites périodes (<20 min). Cependant, nous avons également trouvé des différences qu'on a pu attribuer à une mauvaise représentation de l'écoulement à grande échelle dans les simulations. Dans la seconde partie, nous avons analysé les flux de quantité de mouvement sur l'ensemble de la campagne PreConcordiasi et nous avons montré que les spectres de vitesses de phase avaient des distributions robustes avec les maximums de flux pour des vitesses de phases relatives quasi-nulles. Nous avons quantifié l'intermittence des flux de quantité de mouvement en utilisant des PDF et le coefficient de Gini (valeurs de 0.5-0.6). Nous avons attribué l'intermittence pour les valeurs les plus élevées du flux aux évènements convectifs. Nous avons étudié l'importance relative des effets orographiques et convectifs, et nous avons tirons les résultats suivants : d'une part on trouve une plus grande fréquence d'évènements convectifs aux tropiques (c'est ce à quoi on s'attend), d'autre part nous montrons que l'amplitude des flux associés aux effets orographiques et convectifs sont comparables. Enfin, nous avons calculé la contribution globale des cyclones tropicaux au forçage de la moyenne atmosphère. Bien qu'ils représentent des sources locales intenses d'ondes de gravité, la contribution reste relativement faible à l'échelle

globale.

Les perspectives en ce qui concerne l'étude des ondes convectives sont nombreuses. Pour explorer plus systématiquement le réalisme des simulations à méso-échelle, on peut envisager de faire plus de simulations WRF sur des cas de la campagne Pre-Concordiasi. Ceci permettrait d'analyser davantage la relation aux sources ainsi que les vitesses de phase des ondes. En effet, les modélisateurs qui écrivent les paramétrisations d'ondes de gravité souhaitent qu'on distingue davantage les spectres de vitesse de phase pour la convection profonde et de la convection superficielle, et ils aimeraient obtenir plus d'informations sur les directions de propagation des ondes (communication personnelle avec J. Alexander, J. Richter, et J. Bacmeister, 2013). Ces simulations nécessitent cependant une très haute résolution spatiale afin de représenter correctement les sources convectives, et sont par conséquent couteuses. Une voie possible consisterait en des collaborations avec des personnes qui font de telles simulations, pour analyser les caractéristiques des ondes (spectres) dans leurs simulations. Une collaboration avec Stuart Webster au MetOffice avait été évoquée au cours de la thèse notamment. Pour les observations, la prochaine étape naturelle est de faire une description plus complète que ce qu'a permis PreConcordiasi. C'est ce qui va se réaliser avec la campagne Stratéole 2, qui devrait avoir lieu en 2018-2019.

Une autre opportunité s'est offerte pour l'étude des ondes de gravité avec les observations de la campagne Concordiasi, cette fois aux hautes latitudes de l'hémisphère sud. L'analyse des observations SPB (le travail comparable à celui fait par *Hertzog et al.* (2008) pour Vorcore) est en cours par *Hertzog et al.*. Nous avons utilisé ces observations comme description de référence pour évaluer le réalisme des ondes de gravité résolues dans les analyses de l'ECMWF. Dans un premier temps, nous avons dérivé une climatologie moyenne des flux et montré qu'il y a un bon accord géographique entre ECMWF et Concordiasi à l'exception de la chaîne de montagnes transantarctiques. En revanche, les flux sont sous-estimées en moyenne d'un facteur 5 dans

l'ECMWF par rapport à Concordiasi. On note également un contraste plus marqué entre le plateau Antarctique et les autres régions dans l'ECMWF. Nous avons confirmé que l'intermittence est plus forte pour les OGW que les NGW. Dans la seconde partie de l'étude, nous avons observé que l'activité d'ondes de gravité est maximale au printemps et qu'elle diminue en novembre avec un minimum en décembre-janvier, avec la disparition du jet stratosphérique. En outre, les flux moyens pour les OGW et les NGW diminuent de 95% et 78% respectivement entre septembre et janvier. En d'autres termes, la diminution de la fréquence des évènements intenses diminue la valeur moyenne du flux, et son intermittence. Enfin, les champs d'ondes de gravité sont comparés dans l'ECMWF et Concordiasi sur 3 cas d'études d'OGW et NGW, et confirment encore une fois un bon accord géographique et le facteur 5 pour la magnitude.Enfin, nous avons déterminé que la traînée d'onde de gravité manquant dans les modèles qui produit un biais sur la destruction du vortex polaire au printemps dans l'hémisphère sud pourrait provenir d'effets non-orographiques mal représentés par les paramétrisations.

Cette étude ouvre la voie pour l'utilisation des analyses ECMWF afin d'étudier les ondes à échelle globale (hautes latitudes), les variations saisonnières et interannuelles. Il peut être intéressant d'étudier quelle part de la variabilité attribuer à la propagation, et aux sources. Par exemple, l'hypothèse décrite par *McLandress et al.* (2012) selon laquelle le déficit en drag à 60°S pourrait provenir d'ondes se propageant méridionallement (effet non représenté par les paramétrisations qui supposent toutes une propagation purement verticale) vers le cœur du jet stratosphérique mérite d'être examinée. Enfin, on peut envisager à l'avenir d'effectuer des comparaisons avec des paramétrisations hors-ligne, comme le font certains déjà au sein de l'équipe (Álvaro de la Cámara et François Lott).

La dernière partie constitue une contribution aux efforts pour faciliter la mise en oeuvre de campagnes d'observation par ballon. Nous avons mis notre expertise

en simulation à méso-échelle au service de la prévision de trajectoires de ballons. Ceci a été fait pour des ballons stratosphériques ouverts (OSBs), pour lesquels les contraintes de sécurité sont les plus fortes. Nous avons choisi 3 cas tests provenant de la campagne Strapolété qui a eu lieu à Kiruna, en Suède en 2009 pour examiner dans quelle mesure les prévisions peuvent être améliorées avec les simulations à méso-échelle et l'assimilation de données supplémentaires. Nous avons observé un impact généralement positif à l'utilisation de simulations à méso-échelle qui provient en partie d'une meilleure résolution spatiale et temporelle. D'autre part, nous avons remarqué que l'assimilation d'un unique radiosondage produisait des incréments horizontaux et verticaux significatifs (quelques m s^{-1}), mais que l'information était rapidement advectée par l'écoulement hors du domaine. L'assimilation d'observations peu de temps (1-2 h) avant que le ballon n'atteigne son plafond a un impact positif sur la prévision du point de chute du ballon. La distance à la position finale réelle observée est réduite de 50% ou plus par rapport aux prévisions utilisant les analyses ECMWF. Toutefois, nous observons des différences qui sont dues à la mauvaise représentation de gradients horizontaux ou verticaux par nos simulations d'ensemble, ce qui suggère que nos expériences peuvent encore être améliorées à l'avenir.

Les travaux futurs sur la prévisions des trajectoires de ballons, passent par une réflectioon sur la génération optimale des pertubations d'ensemble, et l'étude d'un grand nombre de cas. Dans le même temps, une réflexion sur les données supplémentaires locales à assimiler (données de profileurs de vent) semble une piste intéressante. Nous avons souligné dans notre étude l'impact de la hauteur du toit, ce qui nous montre l'importance de faire des tests de sensibilité pour ce paramètre. En revanche, la description des ondes d'inertie gravité dans la basse stratosphère reste une limitation difficile à franchir. Enfin pour les opérations, il est crucial d'améliorer et automatiser les procédures et d'optimiser le temps de calcul numérique et le transfert des données (communication personnelle avec P. Cocquerez, S. Louvel, et A. Doerenbecher, 2014).

BIBLIOGRAPHY

BIBLIOGRAPHY

Aksoy, A., D. C. Dowell, and C. Snyder (2009), A multicase comparative assessment of the ensemble Kalman filter for assimilation of radar observations. Part I: Storm-scale analyses, *Mon. Wea. Rev.*, *137*, 1805–1824.

Aksoy, A., D. C. Dowell, and C. Snyder (2010), A multicase comparative assessment of the ensemble Kalman filter for assimilation of radar observations. Part II: Short-range ensemble forecasts, *Mon. Wea. Rev.*, *138*, 1273–1292.

Alexander, M. J. (1998), Interpretations of observed climatological patterns in stratospheric gravity wave variance, *J. Geophys. Res.*, *103*, 8627–8640.

Alexander, M. J., and L. Pfister (1995), Gravity wave momentum flux in the lower stratosphere over convection, *Geophys. Res. Lett.*, *22*, 2029–2032.

Alexander, M. J., and H. Teitelbaum (2007), Observation and analysis of a large amplitude mountain wave event over the Antarctic peninsula, *J. Geophys. Res.*, *112*, D21,103,doi:10.1029/2006JD008,368.

Alexander, M. J., and R. A. Vincent (2000), Gravity waves in the tropical lower stratosphere: A model study of seasonal and interannual variability, *J. Geophys. Res.*, *105*, 22,299–22,310.

Alexander, M. J., J. R. Holton, and D. R. Durran (1995), The gravity wave response above deep convection in a squall line simulation, *J. Atmos. Sci.*, *52*, 2212–2226.

Alexander, M. J., J. H. Beres, and L. Pfister (2000), Tropical stratospheric gravity wave activity and relationship to clouds, *J. Geophys. Res.*, *105*, 22,299–22,309.

Alexander, M. J., J. H. Richter, and B. R. Sutherland (2006), Generation and trapping of gravity waves from convection with comparison to parameterization, *J. Atmos. Sci.*, *63*, 2963–22,310.

Alexander, M. J., S. D. Eckermann, D. Broutma, and J. Ma (2009), Momentum flux estimates for South Georgia Island mountain waves in the stratosphere observed via satellite, *Geophys. Res. Lett.*, *36*, L12,816,doi:10.1029/2009GL038,587.

Alexander, M. J., et al. (2010), Recent developments in gravity-wave effects in climate models and the global distribution of gravity-wave momentum flux from observations and models, *Q.J.R. Meteorol. Soc.*, *136*, 1103–1124.

Alexander, P., and A. de La Torre (2003), A program or the simulation and analysis of open atmospheric balloon soundings, *Comp. Phys.Com.*, *151*, 96–120.

Allen, S. J., and R. A. Vincent (1995), Gravity wave activity in the lower atmosphere: Seasonal and latitudinal variations, *J. Geophys. Res.*, *100*, DOI:10.1029/94JD02,688.

Anderson, B. D., and J. B. Moore (1979), *Optimal filtering*, Prentice-Hall, Englewood Cliffs, NJ.

Anderson, J. (2001), A ensemble adjustment Kalman filter for data assimilation, *Mon. Wea. Rev.*, *129*, 2884–2903.

Anderson, J. (2009), Spatially and temporally varying adpatative covariance inflation for ensemble filters, *Tellus*, *61*, 72–83.

Anderson, J., T. Hoar, K. Raeder, H. Liu, N. Collins, R. Torn, and A. Avellano (2009), The Data Assimilation Research Testbed: A community facility, *B. Amer. Meteor. Soc.*, *90*, 1283–1296.

Andrews, D. G., J. R. Holton, and C. B. Leovy (1987), *Middle atmosphere dynamics*, Academic Press.

Angot, G., G. P. Keckhut, A. Hauchecorne, and C. Claud (2012), Contribution of stratospheric warmings to temperature trends in the middle atmosphere from the lidar series obtained at Haute-Provence Observatory (44°N), *J. Geophys. Res.*, *117*, D21,102,DOI:10.1029/2012JD017,631.

Arakawa, A., and V. R. Lamb (1977), Computational design of the basic dynamical processes of the UCLA general circulation model, *Methods Comput. Phys.*, *17*, 173–265.

Aref, H. (1984), Stirring by chaotic advection, *J. Fluid Mech.*, *143*, 1–21.

Aref, H. (1990), Chaotic advection of fluid particles, *Philos. Trans. Roy. Soc. London A*, *333*, 273–288.

Austin, J., et al. (2003), Uncertainties and assessment of chemistry-climate models of the stratosphere, *Atm. Chem. Phys.*, *3*, 1–27.

Bacmeister, J. T., M. R. Schoebert, L. R. Lait, P. A. Newman, and B. L. Gary (1990a), Small-scale waves encountered during aase, *Geophys. Res. Lett.*, *17*, 349–352.

Bacmeister, J. T., M. R. Schoebert, L. R. Lait, P. A. Newman, and B. L. Gary (1990b), ER-2 mountain wave encounter over Antarctica: Evidence for blocking, *Geophys. Res. Lett.*, *17*, 81–84.

Bacmeister, J. T., S. D. Eckermann, P. A. Newman, L. Lait, K. R. Chan, M. Loewenstein, M. H. Proffitt, and B. L. Gary (1996), Stratospheric horizontal wavenumber spectra of winds, potential temperature and atmospheric tracers observed by high-altitude aircraft, *J. Geophys. Res.*, *101*, 9441–9470.

Baldwin, M. P., et al. (2001), The quasi-biennal oscillation, *Rev. Geophys.*, *39*(2), 179–229.

Boccara, G., A. Hertzog, R. A. Vincent, and F. Vial (2008), Estimation of gravity wave momentum flux and phase speeds from quasi-lagrangian stratospheric balloon flights. Part I: Theory and simulations, *J. Atmos. Sci.*, *65*, 3042–3055.

Butchart, N., et al. (2010), Chemistry-climate model simulations of twenty-first century stratospheric climate and circulation changes, *J. Climate*, *23*, 5349–5374.

Caya, A., J. Sun, and C. Snyder (2005), A comparison between the 4DVAR and the Ensemble Kalman Filter techniques for radar data assimilation, *Mon. Wea. Rev.*, *133*, 3081–3094.

Chagnon, J. M., and S. L. Gray (2008), Analysis of convectively-generated gravity waves in mesoscale model simulations and wind-profiler observations, *J. Geophys. Res.*, *134*, 663–676.

Chen, F., and J. Dudhia (2001), Coupling an advanced land surface hydrology model with the Penn State-NCAR MM5 modeling system. Part I: Model implementation and sensitivity, *Mon. Wea. Rev.*, *129*, 569–585.

Chin, M., and A. J. Mariani (2009), A Particle Filter for inverse Lagrangian prediction problems, *J. Atmos. Ocean. Tech.*, *27*, 371–384.

Chu, C.-M., and Y.-L. Lin (2000), Effects of orography on the generation and propagation of mesoscale convective systems in a two-dimensional conditionally unstable flow, *J. Atmos. Sci.*, *57*, 3817–3837.

Clark, T. L., T. Hauf, and J. P. Kuettner (1986), Convectively forced internal gravity waves: Results from two-dimensional numerical experiments, *Q.J.R. Meteorol. Soc.*, *112*, 899–925.

Coniglio, M. C., K. L. Elmore, J. S. Kain, S. J. Weiss, M. Xue, and M. L. Weisman (2010), Evaluation of WRF model output for severe weather forecasting from the 2008 NOAA Hazardous Weather Testbed Spring Experiment, *Wea. Forecasting*, *25*, 408–427.

Dewan, E., R. Picard, R. O'Neil, H. Gardiner, J. Gibson, J. Mill, E. Richards, M. Kendra, and W. Gallery (1998), MSX satellite observations of thunderstormgenerated gravity waves in midwave infrared images of the upper stratosphere, *Geophys. Res. Lett.*, *25*(7), doi:10.1029/98GL00,640.

Dhaka, S., M. Takahashi, Y. Shibagaki, M. Yamanaka, and S. Fukao (2003), Gravity wave generation in the lower stratosphere due to passage of the typhoon 9426 (Orchid) observed by the MU radar at Shigaraki (34.85N, 136.10E), *J. Geophys. Res.*, *108* (doi:10.1029/2003JD003489), 4595.

Douville, H. (2009), Stratospheric polar vortex influence on Northern Hemisphere winter climate variability, *Geophys. Res. Lett.*, *36*, L18,703.

Dowell, D. C., and L. J. Wicker (2008), Additive noise for storm-scale ensemble data assimilation, *J. Atmos. Ocean. Technol.*, *26*, 911–927.

Dowell, D. C., F. Zhang, L. J. Wicker, C. Snyder, and N. A. Crook (2004), Wind an temperature retrievals in the 17 May 1981 Arcadia, Oklahoma, supercell: Ensemble Kalman filter experiments, *Mon. Wea. Rev.*, *132*, 1982–2005.

Dunkerton, T. J. (1997), The role of gravity waves in the quasi-biennial oscillation, *J. Geophys. Res.*, *102*, 26,053–26,076.

Eckermann, S. D., A. Dörnbrack, S. B. Vosper, H. Flentje, M. J. Mahoney, T. P. Bui, and K. S. Carslaw (2006), Mountain wave-induced polar stratospheric cloud forecasts for aircraf science flights during SOLVE/THESEO 2000, *Wea. Forecasting*, *21*, 42–68.

Ern, M., P. Preusse, M. J. Alexander, and C. D. Warner (2004), Absolute values of gravity wave momentum flux derived from satellite data, *J. Geophys. Res.*, *109*, doi:10.1029/2004JD004,752.

Ern, M., P. Preusse, M. K. M. G. Mlynczak, and J. M. Russell, III (2008), Equatorial wave analysis fromSABER and ECMWF temperatures, *Atmos. Chem. Phys.*, *8*, 845–869.

Ern, M., P. Preusse, J. C. Gille, C. L. Hepplewhite, M. G. Mlynczak, J. M. Russell, III, and M. Riese (2011), Implications for atmospheric dynamics derived from global observations of gravity wave momentum flux in stratosphere and mesosphere, *J. Geophys. Res.*, *116* (D19107), doi:10.1029/2011JD015,821.

Evan, S., M. J. Alexander, and J. Dudhia (2012), WRF simulations of convectively generated gravity waves in opposite QBO phases, *J. Geophys. Res.*, *117* (D12117), doi:10.1029/2011JD017,302.

Evensen, G. (2003), The Ensemble Kalman Filter: theoretical formulation and practical implementation, *Ocean Dyn.*, *53*, 343–367.

Eyring, V., T. G. Shepherd, and D. W. Waugh (2010), SPARC CCMVal (2010), SPARC report on the evaluation of Chemistry-Climate Models, SPARC report n°5, WCRP-132, WMO/TD-No1526, *Tech. rep.*

Fovell, R., D. Durran, and J. R. Holton (1992), Numerical simulations of convectively generated stratospheric gravity waves, *J. Atmos. Sci.*, *49*, 1427–1442.

Fritts, D. C., and M. J. Alexander (2003), Gravity wave dynamics and effects in the middle atmosphere, *Reviews of Geophysics*, *41*(1), 1003.

Fritts, D. C., and G. D. Nastrom (1992), Sources of mesoscale variability of gravity waves, II, Frontal, convective, and jet stream excitation, *J. Atmos. Sci.*, *49*, 111–127.

Fritts, D. M., D. C. Fritts, C. D. Fawcett, E. Kudeki, and M. H. Hitchman (1997), Radar observations of gravity waves over Jicamarca, Peru during the CADRE campaign, *J. Atmos. Sci.*, *102*, 136–156.

Fueglistaler, S., A. E. Dessler, T. J. Dunkerton, I. Folkins, Q. Fu, and P. W. Mote (2009), Tropical tropopause layer, *Rev. Geophys.*, *47*, DOI:10.1029/2008RG000,267.

Gary, B. L. (1989), Observational results using the microwave temperature profiler during the airborne antarctic ozone experiment, *J. Geophys. Res.*, *94*, 11,223–11,231.

Gaspari, G., and S. E. Cohn (1999), Construction of correlation functions in two and three dimensions, *Q.J.R. Meteorol. Soc.*, *125*, 1897–1916.

Geller, M. A., et al. (2013), A comparison between gravity wave momentum fluxes in observations and climate models, *J. Climate*, *26*, 6383–6405.

Gerber, E. P., et al. (2012), Assessing and understanding the impact of stratospheric dynamics and variability on the Earth system, *B. Amer. Meteor. Soc.*, *93*, 845–859.

Gini, C. (1912), *Variabilità e mutabilità (Variability and Mutability)*, 156p pp., Libreria Eredi Virgilio Veschi (1955).

Gong, J., M. A. Geller, and L. Wang (2008), Source spectra information derived from US high-resolution radiosonde data, *J. Geophys. Res.*, *113*, D10,106.DOI:10.1029/2007/JD009,252.

Grell, G. A., and D. Devenyi (2002), Numerical simulation of a tornado vortex, *Geophys. Res. Lett.*, *29*, 1693.

Griffa, A., L. I. Piterbarg, and T. M. Özgökmen (2004), Predictability of Lagrangian particle trajectories: Effects of smoothing of the underlying Eulerian flow, *J. Marine Res.*, *62*, 1–35.

Hansen, F., K. Matthes, and L. J. Gray (2013), Sensitivity of stratospheric dynamics and chemistry to QBO nudging width in the chemistryclimate model WACCM, *J. Geophys. Res.*, *118*, 10,464–10,474.

Hertzog, A., and F. Vial (2001), A study of the dynamics of the equatorial lower stratosphere by use of ultra-long-duration balloons, 2. Gravity waves, *J. Geophys. Res.*, *106*, 22,745–22,761.

Hertzog, A., C. Basdevant, F. Vial, and C. Mechoso (2003), The accuracy of stratospheric analyses in the northern hemisphere inferred from long-duration balloon flights, *J. Geophys. Res.*, *130*, 607–626.

Hertzog, A., G. Boccara, R. Vincent, F. Vial, and P. Cocquerez (2008), Estimation of gravity-wave momentum fluxes and phase speeds from long-duration stratospheric balloon flights. Part II. Results from the Vorcore campaign in Antarctica, *J. Atmos. Sci.*, *65*, 3056–3070.

Hertzog, A., M. J. Alexander, and R. Plougonven (2012), On the intermittency of gravity-wave momentum flux in the stratosphere, *J. Atmos. Sci.*, *69*, 3433–3448.

Hertzog, A., et al. (2007), Stratéole/Vorcore - Long duration, superpressure balloons to study the antarctic stratosphere during the 2005 winter, *J. Ocean. Atmos. Tech.*, *24*, 2048–2061.

Holton, J. R. (2004), *An introduction to dynamic meteorology*, Elsevier Academic Press.

Holton, J. R., and R. S. Lindzen (1972), An updated theory for the quasi-biennal cycle in the tropical stratosphere, *J. Atmos. Sci.*, *29*, 1076–1080.

Holton, J. R., P. H. Haynes, M. E. McIntyre, A. R. Douglass, R. B. Rood, and L. Pfister (1995), Stratosphere-troposphere exchange, *Rev. Geophys.*, *33*, 405–439.

Hong, S.-Y., and H.-L. Pan (1996), Nonlocal boundary layer vertical diffusion in a medium-range forecast model, *Mon. Wea. Rev.*, *124*, 2322–2339.

Hong, S.-Y., J. Dudhia, and S.-H. Chen (2004), A revised approach to ice microphysical processes for the bulk parameterization of clouds and precipitation, *Mon. Wea. Rev.*, *132*, 103–120.

Huret, N., et al. (2010), STRAPOLÉTÉ: Studying the summer polar stratosphere, Europ. Geos. Union, EGU General Assembly, Vienna, Austria.

Iacono, M. J., J. S. Delamere, E. J. Mlawer, M. W. Shephard, S. A. Clough, and W. D. Collins (2008), Radiative forcing by long-lived greenhouse gases: Calculations with the AER radiative transfer models, *J. Geophys. Res.*, *113*, doi:10.1029/2008JD009,944.

Jewtoukoff, V., R. Plougonven, and A. Hertzog (2013), Gravity waves generated by deep tropical convection: Estimates from balloon observations and mesoscale simulations, *J. Geophys. Res.*, *118*, 9690–9707.

Kahl, J. D., and P. J. Samson (1986), Uncertainty in trajectory calculations due to low resolution meteorological data, *J. Clim. Appl. Meteo.*, *25*, 1816–1831.

Kawatani, Y., S. Watanabe, K. Sato, T. J. Dunkerton, S. Miyahara, and M. Takahashi (2010), The roles of equatorial trapped waves and internal inertia-gravity waves in driving the Quasi-Biennal Oscillation. Part I: Zonal mean wave forcing, *J. Atmos. Sci.*, *67*, 963–980.

Keil, M., M. Heun, J. Austin, W. Lahoz, G. P. Lou, and A. O'Neill (2001), The use of long-duration balloon data to determine the accuracy of stratospheric analyses and forecasts, *J. Geophys. Res.*, *106*, 10,299–10,312.

Kim, S.-Y., H.-Y. Chun, and J.-J. Baik (2005), A numerical study of gravity waves induced by convection associated with Typhoon Rusa, *Geophys. Res. Lett.*, *32*(L24816), doi:10.1029/2005GL024,662.

Kim, S.-Y., H.-Y. Chun, and J.-J. Baik (2007), Sensitivity of typhoon-induced gravity waves to cumulus parameterizations, *Geophys. Res. Lett.*, *34*(L15814), doi:10.1029/2007GL030,592.

Kim, Y.-J., and H.-Y. Chun (2010), Stratospheric gravity waves generated by Typhoon Saomai (2006): Numerical modeling in a moving frame following the Typhoon, *J. Atmos. Sci.*, *67*, 3617–3636.

Kim, Y.-J., S. D. Eckermann, and H.-Y. Chun (2003), An overview of the past, present and future of gravity-wave drag parametrization for numerical climate and weather prediction models, *J. Appl. Meteo.*, *41*, 65–98.

Klinker, E., F. Rabier, G. Kelly, and J.-F. Mahfouf (2000), The ECMWF operational implementation of four-dimensional variational assimilation. Part III: Experimental results and diagnostics with operational configuration, *Q.J.R. Meteorol. Soc.*, *126*, 1191–1215.

Knippertz, P., J. M. Chagnon, A. Foster, L. Lathouwers, J. H. Marsham, J. Methven, and D. J. Parker (2010), Research flight observations of a prefrontal gravity wave near the southwestern UK, *Weather*, *65*, 293–297.

Knudsen, B. M., and G. D. Carver (1994), Accuracy of the isentropic trajectories calculated for the EASOE campaign, *Geophys. Res. Lett.*, *21*, 1199–1202.

Knudsen, B. M., J. M. Rosen, N. T. Kjome, and A. T. Whitten (1996), Comparison of analyzed stratospheric temperatures and calculated trajectories with long-duration balloon data, *J. Geophys. Res.*, *101*, 19,137–19,145.

Knudsen, B. M., J.-P. Pommereau, A. Garnier, M. Nunez-Pinharanda, L. Denis, G. Letrenne, M. Durand, and J. M. Rosen (2001), Comparison of stratospheric air parcel trajectories based on different meteorological analyses, *J. Geophys. Res.*, *106*, 3415–3424.

Kuester, M. A., M. J. Alexander, and E. A. Ray (2008), A model study of gravity waves over Hurricane Humberto (2001), *J. Atmos. Sci.*, *65*, 3231–3246.

Kuo, Y.-H., M. Skumanich, and P. L. H. J. S. Chang (1985), The accuracy of trajectory models as revealed by the observing system simulation experiments, *Mon. Wea. Rev.*, *113*, 1852–1867.

Lane, T. P., and J. C. Knievel (2005), Some effects of model resolution on simulated gravity waves generated by deep, mesoscale convection, *J. Atmos. Sci.*, *62*, 3408–3419.

Lane, T. P., M. J. Reeder, and T. L. Clark (2001), Numerical modeling of gravity wave generation by deep tropical convevction, *J. Atmos. Sci.*, *58*, 1249–1274.

Lin, Y. I., and R. B. Smith (1986), Transient dynamics of airflow near a local heat source, *J. Atmos. Sci.*, *43*, 40–49.

Lindzen, R. S., and J. R. Holton (1968), A theory of quasi-biennal oscillation, *J. Atmos. Sci.*, *26*, 1095–1107.

Liu, Z., C. S. Schwartz, C. Snyder, and S.-Y. Ha (2012), Impact of assimilating AMSU-A radiances on forecasts of 2008 Atlantic Tropical Cyclones initialized with a limited-area Ensemble Kalman Filter, *Mon. Wea. Rev.*, *140*, 4017–4034.

Lott, F., R. Plougonven, and J. Vanneste (2010), Gravity waves generated by sheared potential vorticity anomalies, *J. Atmos. Sci.*, *67*, 157–170.

Lott, F., R. Plougonven, and J. Vanneste (2012), Gravity waves generated by sheared three-dimensional potential vorticity anomalies, *J. Atmos. Sci.*, *69*, 2134–2151.

Mahfouf, J.-F., and F. Rabier (2000), The ECMWF operational implementation of four-dimensional variational assimilation. II: Experimental results with improved physics, *Q.J.R. Meteorol. Soc.*, *126*, 1171–1190.

Marsh, A. K. P., N. J. Mitchell, and L. Thomas (1991), Lidar studies of stratospheric gravity-wave spectra, *Planet. Space Sci.*, *39*, 1541–1548.

McLandress, C., M. J. Alexander, and D. L. Wu (2000), Microwave Limb Sounder observations of gravity waves in the stratosphere: A climatology and interpretation, *J. Geophys. Res.*, *105*, 11,967–11,967.

McLandress, C., T. G. Shepherd, S. Polavarapu, and S. R. Beagley (2012), Is missing orographic gravity wave drag near 60°S the case of the stratospheric zonal winds biases in Chemistry-Climate Models?, *J. Atmos. Sci.*, *69*, 802–818.

McLandress, C., J. F. Scinocca, T. G. Shepherd, M. C. Reader, and G. L. Manney (2013), Dynamical control of the mesosphere by orographic and nonorographic gravity wave drag during the extended northern winters of 2006 and 2009, *J. Atmos. Sci.*, *70*, 2152–2169.

Mitchell, N. J., L. Thomas, and A. K. P. Marsh (1991), Lidar observations of long-period gravity waves in the stratosphere, *Ann. Geophys.*, *9*, 588–596.

Molteni, F., R. B. abd T. N. Palmer, and T. Petroliagis (1995), The ECMWF Ensemble Prediction System: Methodology and validation, *Q.J.R. Meteorol. Soc.*, *122*, 73–119.

Nastrom, G. D., D. C. Fritts, and K. S. Gage (1987), An investigation of terrain effects on the mesoscale spectrum of atmospheric motions, *J. Atmos. Sci.*, *44*, 3087–3096.

Nicholls, M. E., R. A. Pielke, and W. R. Cotton (1991), Thermally forced gravity waves in an atmosphere at rest, *J. Atmos. Sci.*, *48*, 1869–1884.

Orr, A., P. Bechtold, J. Scinocca, M. Ern, and M. Janiskova (2010), Middle atmosphere climate and forecasts in the ECMWF model through a nonorographic gravity wave drag parameterization, *J. Climate*, *23*, 5905–5926.

Özgökmen, T. M., A. Griffa, A. J. Mariano, and L. I. Piterbarg (1999), On the predictability of Lagrangian trajectories in the ocean, *J. Atmos. Ocean. Tech*, *17*, 366–383.

Özgökmen, T. M., L. I. Piterbarg, A. J. Mariano, and E. H. Ryan (2001), Predictability of drifter trajectories in the Tropical Pacific Ocean, *J. Phys. Ocean.*, *31*, 2691–2720.

Paldor, N., Y. Dvorkin, A. J. Mariano, T. M. Özgökmen, and E. H. Ryan (2004), A practical, hybrid model for predicting the trajectories of near-surface ocean drifters, *J. Atmos. Ocean. Tech.*, *21*, 1246–1258.

Pandya, R. E., and D. R. Durran (1996), The influence of convectively generated thermal forcing on the mesoscale circulation around squall lines, *J. Atmos. Sci.*, *20*, 2924–2951.

Pandya, R. E., D. Durran, and C. Bretherton (1993), Comments on "Thermally forced gravity waves in an atmosphere at rest", *J. Atmos. Sci.*, *50*, 4097–4101.

Pawson, S., et al. (2000), The GCM-Reality Intercomparison Project for SPARC (GRIPS): scientific issues and initial results, *B. Amer. Meteor. Soc.*, *81*, 781–796.

Pfister, L. W., K. R. Chan, T. P. Bui, S. Bowen, M. Legg, B. Gary, K. Kelly, M. Proffitt, and W. Starr (1993a), Gravity waves generated by a tropical cyclone during the STEP tropical field program: a case study, *J. Geophys. Res.*, *98*(D5), 8611–8638.

Pfister, L. W. P. L., S. Scott, M. Loewenstein, S. Bowen, and M. Legg (1993b), Mesoscale disturbances in the tropical stratosphere excited by convection: Observations and effects on the stratospheric momentum budget, *J. Atmos. Sci.*, *50*(D5), 1058–1075.

Piani, C., D. DUrran, M. J. Alexander, and J. R. Holton (2000), A numerical study of three-dimensional gravity waves triggered by deep tropical convection and their role in the dynamics of the QBO, *J. Atmos. Sci.*, *57*, 3689–3702.

Piterbarg, L. I. (2001), Short-term prediction of Lagrangian trajectories, *J. Atmos. Ocean. Tech.*, *18*, 1398–1410.

Plougonven, R., and C. Snyder (2006), Inertia-gravity waves spontaneously generated by jets and fronts. Part I: Different baroclinic life cycles, *J. Atmos. Sci.*, *64*, 2502–2520.

Plougonven, R., and H. Teitelbaum (2003), Comparison of a large-scale inertia-gravity wave as see in the ECMWF analyses and from radiosondes, *Geophys. Res. Lett.*, *30*, doi:10.1029/2003GL017,716.

Plougonven, R., and F. Zhang (2014), Internal gravity waves from atmospheric jets and fronts, *Rev. Geophys.*, *52*, 3376,doi:10.1002/2012RG000,419.

Plougonven, R., A. Hertzog, and H. Teitelbaum (2008), Observations and simulations of a large-amplitude mountain wave breaking above the Antarctic Peninsula, *J. Geophys. Res.*, *113*(D16113), doi:10.1029/2007JD009,739.

Plougonven, R., A. Hertzog, and L. Guez (2013), Gravity waves above antarctica and the southern ocean in mesoscale simulations and balloon observations, *Q.J.R. Meteorol. Soc.*, *139*(101), 118.

Podglajen, A., A. Hertzog, R. Plougonven, and N. Žagar (2014), Assessment of the accuracy of (re)analyses in the equatorial lower stratosphere, *Submitted to J. Geophys. Res.*

Powers, J. G., , K. W. Manning, D. H. Bromwich, J. J. Cassano, and A. M. Cayette (2012), A decade of Antarctica science through AMPS, *B. Amer. Meteor. Soc.*, *93*, 1699–1712.

Preusse, P., S. D. Eckermann, M. Ern, J. Oberheide, R. H. Picard, R. G. Roble, M. Riese, J. M. Russell, III, and M. G. Mlynczak (2009), Global ray tracing simulations of the SABER gravity wave climatology, *J. Geophys. Res.*, *114*, 10.1029/2008JD011,214.

Preusse, P., M. Ern, P. Bechtold, S. D. Eckermann, S. Kalisch, Q. T. Trinh, and M. Riese (2014), Characteristics of gravity waves resolved by ECMWF, *submitted to Atmos. Chem. Phys.*, *14*, 11,961–12,018.

Rabier, F., H. Järvinen, E. Klinker, J.-F. Mahfouf, and A. Simmons (2000), The ECMWF operational implementation of four-dimensional variational assimilation. Part I: Experimental results with simplified physics, *Q.J.R. Meteorol. Soc.*, *126*, 1143–1170.

Rabier, F., et al. (2010), The Concordiasi project in Antarctica, *B. Amer. Meteor. Soc.*, *91*(1), 69–86.

Salby, M. L., and R. R. Garcia (1987), Transient response to localized episodic heating in the tropics, Part I: Excitation and short-time near-field behaviour, *J. Atmos. Sci.*, *44*, 458–498.

Sato, K. (1993), Small-scale wind disturbances observed by the MU radar during the passage of Typhoon Kelly, *J. Atmos. Sci.*, *50*, 518–537.

Sato, K., S. Watanabe, Y. Kawatani, Y. Tomikawa, K. Miyazaki, and M. Takahashi (2009), On the origin of mesospheric gravity waves, *Geophys. Res. Lett.*, *36*, L19,801,doi:10.1029/2009GL039,908.

Schroeder, S., P. Preusse, M. Ern, and M. Riese (2009), Gravity waves resolved in ECMWF and measured by SABER, *Under review for Geophys. Res. Letter*, *36*, L10,805, doi:10.1029/2008GL037,054.

Shutts, G. J., and S. B. Vosper (2011), Stratospheric gravity waves revealed in NWP model forecasts, *Q.J.R. Meteorol. Soc.*, *137*, 303–317.

Skamarock, W. C., J. B. Klemp, J. Dudhia, D. O. Gill, D. M. Barker, W. Wang, and J. G. Powers (2005), A description of the Advanced Research WRF Version 2, *Tech. rep.*, note NCAR/TN-468+STR.

Skamarock, W. C., J. B. Klemp, J. Dudhia, D. O. Gill, D. M. Barker, M. G. Duda, X.-Y. Huang, W. Wang, and J. G. Powers (2008), A description of the Advanced Research WRF Version 3, *Tech. rep.*

Snyder, C., and F. Zhang (2003), Assimilation of simulated Doppler radar observations with an Ensemble Kalman Filter, *Mon. Wea. Rev.*, *131*, 1663–1677.

Snyder, C., D. J. Muraki, R. Plougonven, and F. Zhang (2007), Inertia-gravity waves generated within a dipole vortex, *J. Atmos. Sci.*, *64*, 4417–4431.

Snyder, C., R. Plougonven, and D. J. Muraki (2009), Mechanisms for spontaneous gravity wave generation within a dipole vortex, *J. Atmos. Sci.*, *66*, 3464–3478.

Song, I.-S., H.-Y. Chun, and T. P. Lane (2003), Generation mechanisms of convectively forced internal gravity waves and their propagation to the stratosphere, *J. Atmos. Sci.*, *60*, 1960–1980.

Thompson, W. J., and J. M. Wallace (1998), The Arctic Oscillation signature in the wintertime geopotential height and temperature fields, *Geophys. Res. Lett.*, *25*, 1297–1300.

Tong, M., and M. Xue (2005), Ensemble Kalmanfiter assimilation of Doppler radar data with a compressible nonhydrostatic model: OSS experiments, *Mon. Wea. Rev.*, *133*, 1789–1807.

Tsuda, T., T. Inoue, D. C. Fritts, T. D. VanZandt, S. Kato, T. Sato, and S. Fukao (1989), MST radar observations of a saturated gravity wave spectrum, *J. Atmos. Sci.*, *46*, 2440–2447.

Vallis, G. K. (2006), *Atmospheric and oceanic fluid dynamics: Fundamentals and large-scale circulation*, 407 pp., Cambridge University Press.

Vaughan, G., and R. M. Worthington (2007), Inertia-gravity waves observed by the UK MST radar, *Q.J.R. Meteorol. Soc.*, *133*, 179–188.

Vincent, R. A., and M. J. Alexander (2000), Gravity waves in the tropical lower stratosphere: An observational study of seasonal and interannual variability, *J. Geophys. Res.*, *105*, 971–982.

Vincent, R. A., and A. Hertzog (2014), The response of superpressure balloons to gravity wave motions, *Atms. Meas. Tech.*, *7*, 1043–1055.

Vincent, R. A., and I. M. Reid (1983), HF Doppler measurements of mesospheric gravity wave momentum fluxes, *J. Atmos. Sci.*, *40*, 1321–1333.

Vincent, R. A., S. J. Allen, and S. D. Eckermann (1997), *'Gravity-wave parameters in the lower atmosphere'. In Gravity Wave Processes: Their parameterizations in Global Climate Models*, 7-25 pp., Hamilton K.(ed). Springer-Verlag: Berlin.

Vincent, R. A., A. Hertzog, G. Boccara, and F. Vial (2007), Quasi-lagrangian superpressure balloon measurements of gravity-wave momentum fluxes in the polar stratosphere of both hemispheres, *Geophys. Res. Lett.*, *34*, L19804, doi: 10.1029/2007GL031072.

Walmsley, J. L., and J. Mailhot (1983), On the numerical accuracy of of trajectory models for long-range transport of atmospheric pollutants, *Atmos. Ocean*, *21*, 14–39.

Wang, L. M., M. J. Alexander, P. T. Bui, and M. J. Mahoney (2006), Small-scale gravity waves in ER-2 MMS/MTP wind and temperature measurements during CRYSTAL-FACE, *Atmos. Chem. Phys.*, *6*, 1091–1104.

Wang, S., F. Zhang, and C. Snyder (2008), Generation and propagation of inertia-gravity waves from vortex dipoles and jets, *J. Atmos. Sci.*, *66*, 1294–1314.

Wheatley, D., D. J. Stensrud, D. C. Dowell, and N. Yussouf (2012), Application of WRF mesoscale data assimilation system to springtime severe weather events 2007-09, *Mon. Wea. Rev.*, *140*, 1539–1557.

Whiteway, J. A., and A. I. Carswell (1995), Lidar observations of gravity wave activity in the upper stratosphere over Toronto, *J. Geophys. Res.*, *100*, 14,113–14,124.

Wicker, L. J., and W. C. Skamarock (2002), Time splitting methods for elastic models using forward time schemes, *Mon. Wea. Rev.*, *130*, 2088–2097.

Wilson, R., M. L. Chanin, and A. Hauchecorne (1991a), Gravity waves in the middle atmosphere observed by Rayleigh lidar: 1. Case studies, *J. Geophys. Res.*, *96*, 5153–5167.

Wilson, R., M. L. Chanin, and A. Hauchecorne (1991b), Gravity waves in the middle atmosphere observed by Rayleigh lidar: 1. Climatology, *J. Geophys. Res.*, *96*, 5169–5183.

Wu, D. L., and S. D. Eckermann (2008), Global gravity wave variances from Aura MLS: Characteristics and interpretation, *J. Atmos. Sci.*, *65*, 3695–3718.

Zhang, F., C. Snyder, and J. Sun (2004), Impacts of initial estimate and observation availability on convective-scale data assimilation with an Ensemble Kalman Filter, *Mon. Wea. Rev.*, *132*, 1238–1253.

ABSTRACT

Study of the gravity waves in the atmosphere with balloons and simulations

by

Valérian Jewtoukoff

The goal of this thesis is to obtain a better knowledge of the atmospheric gravity waves in the atmosphere, of their sources and characteristics, and their propagation using balloon observations and modeling. The superpressure balloons (SPBs) used in this thesis are one of the best platforms to observe gravity waves, and allow us to retrieve the ensemble of their characteristics. High-resolution models provide a complete description of the flow, not only of the waves, but also of their sources. We have combined SPB measurements and modeling in order to describe the gravity waves and evaluate the gravity wave field in model outputs. Using the observations from PreConcordiasi (2010), the convective gravity waves are described in the Tropics during the whole campaign, and also for a case of developing Tropical Cyclone. Second, observations from the Concordiasi campaign (2010) allow us to quantify the realism of the resolved gravity wave field in the ECMWF analyses at high latitudes (Southern Hemisphere). A good geographical and seasonal agreement is found for the momentum fluxes and the intermittency. However, it is shown that the magnitude is underestimated in the ECMWF. Finally, we bring a contribution to the operational balloon campaigns, with a focus on the open stratospheric balloons, which constitute the greatest challenge for the CNES. For cases during the Strapolété campaign, we show that the uncertainty on the final touchdown position of the balloons can be reduced using a simple setup that assimilates radiosoundings.